Detailed Understanding of Dark State Dynamics of Far-Red Fluorescent Proteins

by

Samantha L. Allen

B.S., Agnes Scott College, 2014

A thesis submitted to the

Faculty of the Graduate School of the

University of Colorado in partial fulfillment

of the requirements for the degree of

Doctor of Philosophy

Department of Chemistry

2020

This thesis entitled:
Detailed Understanding of Dark State Dynamics of Far-Red Fluorescent Proteins.
Written by Samantha L. Allen
has been approved for the College of Arts & Sciences Department of Chemistry

_____
Ralph Jimenez

_____
Amy E. Palmer

Date_____

The final copy of this thesis has been examined by the signatories, and we find that both the content and the form meet acceptable presentation standards of scholarly work in the above mentioned discipline.

Allen, Samantha L. (Ph.D., Chemistry)

Detailed Understanding of Dark State Dynamics of Far-Red Fluorescent Proteins

Thesis directed by Prof. Ralph Jimenez

The development of fluorescent proteins in the far-red and near-infrared has unlocked new potential for deep-tissue imaging, significantly reducing scatter, cellular autofluorescence, and absorption by cellular constituents compared to their blue-shifted counterparts. These proteins are characterized by low quantum yields, which must be improved to fully utilize these proteins for imaging. The dark state photophysics of near-infrared fluorescent proteins have yet to be characterized, which is necessary to render them useful for imaging and to inform generation of mutants with improved quantum yields. This work discusses my study of the dark state conversion of two far-red fluorescent proteins, smURFP and miRFP670, which both use biliverdin as a chromophore. I designed and optimized the fabrication of microwell devices for the isolation of single proteins. Use of these devices speeds data collection and decreases measurement variability compared to the preceding technique. The microwell devices were used to perform time-resolved fluorescence measurements of smURFP and miRFP670, the results of which indicate the proteins' effectiveness and guide future generations of far-red mutants.

Dedication

To Rob, thank you for always pushing me to succeed

Acknowledgments

There are many people who have helped me throughout my graduate studies, and without whom I would not have been able to complete this work. I would like to thank Dr. Leon Venable, my chemistry advisor at Agnes Scott College, who first encouraged me to pursue research opportunities and apply to graduate school. I would also like to thank Dr. Christopher Elles and Dr. Amanda Houk, who first mentored me in research and spectroscopy at the University of Kansas.

Special thanks to my advisor, Dr. Ralph Jimenez, for providing me with interesting research directions to pursue. His guidance has made me into a better scientist. I would also like to thank Pia Friis, who first taught me the basic biology skills that I needed. I would also like to thank Dr. Nancy Douglas, who continued this education. I would like to thank Dr. Brett Fiedler, who recruited me to the group and taught me how to make microfluidics, and to Premashis Manna, for introducing me to dark state conversion. I would like to think Dr. Sheng-Ting Hung and Srijit Mukherjee, for countless discussions on the dark states of fluorescent proteins. Thank you to Dr. Alex Mikhaylov, Kristen Parzuchowski, and Ryan Wilson, for always giving me the physics perspective. Thank you to Emma Simmerman, Dr. Richard Erickson, and Dr. Josh Slocum for your helpful feedback and scientific wisdom throughout this journey.

My friends and family have provided vital support throughout the way. Thank you to Alina Mateo, Zenyth Sheppard, Kathryn Randall, Vaidehi Mehta, Curtis Beimborn, and Randall Chiu for providing me with laughs and support along the way. Thank you to my family for supporting me. Thank you to Amelia Allen, my first friend and sister, who provided me with endless emotional support.

This thesis would not have been possible without the help from my husband, Rob Wells, without whom I could not have completed this degree. One PhD student in a household is bad enough. In addition to coding advice he has given me emotional support throughout thesis writing, providing encouragement along the way, all of this despite working on his own graduate studies at the same time.

Contents

Chapter

List of Tables

Table

List of Figures

Figure

Chapter 1: Introduction

1.1 Discovery and Initial Development of Fluorescent Proteins

The generation of fluorescent proteins with emission wavelengths spanning the visible spectrum enabled knowledge of the inner workings of cells to a degree not previously thought possible. Green fluorescent protein (GFP) was first isolated in 1962 by Osamu Shimomura. He was attempting to isolate the green fluorescence from the jellyfish *Aequorea victoria*, and instead extracted a blue emitting protein, named aequorin. GFP, the protein responsible for the green fluorescence of *Aequorea victoria,* was isolated as a byproduct of the aequorin purification.[1] Shimomura extracted and characterized the structure of the GFP chromophore in 1979,[2] and following this there were no major developments in GFP until the 1990‘s when the gene encoding GFP was cloned and sequenced, and the chromophore formation was characterized, leading to rapid progress in the field.[3-5] Martin Chalfie then used the isolated gene to express GFP in *E. coli* and *C. elegans*. Surprisingly, he found that the *E. coli* and *C. elegans* expressing GFP was fluorescent, indicating that GFP required no species-specific cofactors or enzymes for fluorescence.[6] Prior to this success, it was not believed that the protein alone would generate fluorescence in another organism.

The isolation of the GFP gene and expression in *E. coli* enabled Roger Y. Tsien and his lab to generate new fluorescent proteins (FPs) by making mutations to the amino acid sequence of existing FPs and observing the spectral properties of the resulting protein. Mutants were found with improved brightness, greater photostability, and were generated with a range of wavelengths including ones that were spectrally distinct for the purpose of multicolor imaging.[7-9] The crystal structure of GFP revealed the structure to be an 11-stranded β-barrel with a coaxial helix, with the chromophore forming from the central helix, enabling directed mutagenesis of GFP.[9] This structure is shown in Figure 1.1. Fluorescent proteins which share these structural features are referred to as GFP-like.

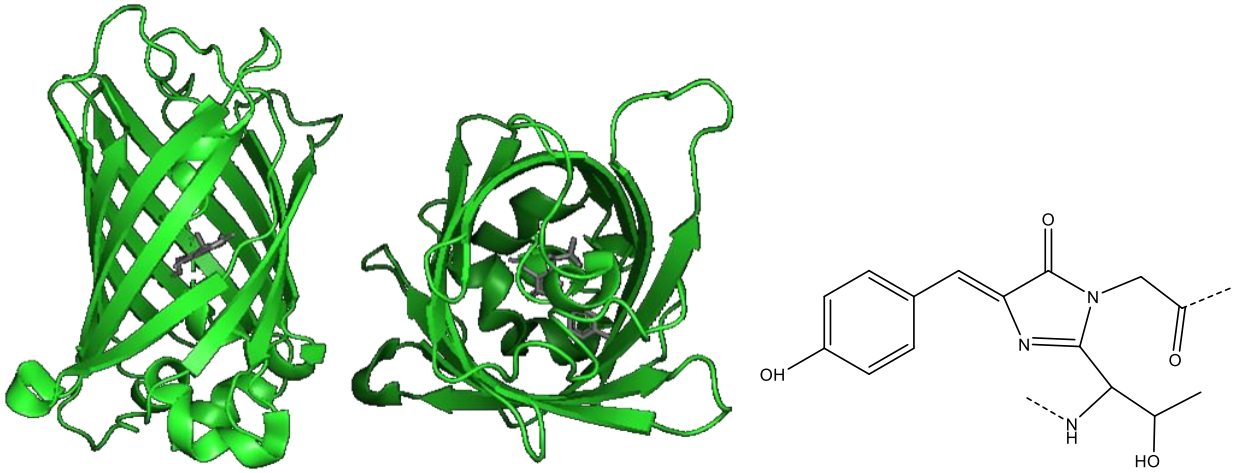

Figure 1.1 Structure of a GFP-like fluorescent protein. (a) Crystal Structure of EGFP (PDB # 2Y0G) (b) Top view of fluorescent protein with chromophore in gray.(c) GFP chromophore

Although mutagensis of GFP was able to generate GFP-like proteins with a range of wavelengths, it was unable to access red wavelengths. It was not until the isolation of the tetrameric fluorescent protein DsRed (558/583 nm ex/em) from coral that red fluorescence was achieved.[10,11] The spectral properties have been found to be caused

by the protein environment surrounding the chromophore in addition to the amino acid residues forming the chromophore. The cyan FP amFP486 has a chromophore formed from Lysine, Tyrosine, and Glycine residues, with Histidine and Alanine sidechains key to the blue shift in fluorescence.[12] Yellow fluorescent protein zFP538 also exhibited a Lysine-Tyrosine-Glycine chromophore, with a red shift caused by extended chromophore conjugation and π-stacking.[13] A structural study of the YFP chromophore found that its Serine-Tyrosine-Glycine chromophore, while identical to the GFP chromophore, is red-shifted by nearly coplanar π-stacking interactions.[14,15] Red-emitting FPs have been shown to undergo an additional multistep reaction for chromophore formation, resulting in delocalization of electron density over the polypeptide backbone and a red-shift in excitation and emission.[10,16] Multiple mutations of DsRed resulted in the generation of a monomeric red fluorescent protein, mRFP1 (584/607 nm ex/em), a protein more useful as a genetically encoded fusion tag compared to the tetrameric DsRed.[17] From this protein, the mFruit series of red fluorescent proteins (RFPs) was developed with improved brightness and photostability, including mCherry (587/610 nm ex/em).[18,19] Considerable work has been done to improve RFPs for spectroscopic study, but no single RFP fulfills all desired qualities (monomeric, bright, minimal blinking at a wide range of irradiances, pH stability, photostability) for optimal use across single molecule and other spectroscopic applications.[20]

In addition to achieving red fluorescence from proteins with the discovery of DsRed, mutagenesis of this protein and others from coral and other sea creatures have also led to the development of GFP-like proteins in the far-red portion of the spectrum. Proteins developed in this region of the spectrum include E2-Crimson (611/646 nm

ex/em),[21] mNeptune (600/650 nm ex/em)[22], TagRFP657 (611/657 nm ex/em),[23] and eFP670 (605/670 nm ex/em).[24] GFP-like far-red fluorescent proteins have been demonstrated to be useful in imaging *in vivo* and in mammalian cells.[21-24] Theoretical study of mPlum (590/649 ex/em) found that the large Stokes shift is increased by displacements of water H-bonds to the imidazolinone ring oxygen in addition to amino acid side chain rotation, with the largest red shift achieved with the highest negative charge accumulation on the acylmine.[25]

Fluorescent proteins possess several advantages compared to small molecule dyes. Fluorescent proteins are genetically econded, meaning they can be incorporated into cells by transforming those cells with DNA that encodes for the fluorescent protein of interest. Once incorporated into cells, they are reproduced by the cellular apparatus and can be used to target subcellular compartments and to interact with an analyte.[7,26,27] Fluorescent proteins exhibit lower brightness and lower photostability compared to small molecule dyes.

Dyes can leak out of cells and are difficult to load in thicker tissues, often requiring invasive techniques to import them into cells. While dyes alone cannot target subcellular compartments like fluorescent proteins, hybrid biosensors have been introduced to combine the benefits of synthetic dyes with the benefits of the genetic encodability of fluorescent proteins. Hybrid biosensors utilize bright, photostable synthetic dyes to improve upon the imaging capabilities, which can then be bound to a fluorescent protein tag to target specific cellular locations. These hybrid sensors are still in the early phases of development and suffer from the same cellular delivery issues dyes face with many of them demonstrated in cell culture only.[28]

Fluorescent proteins have been used as sensors for pH, temperature, and analyte concentration.[27,29,30] Using fluorescent proteins to monitor cellular activity is advantageous because the protein genetic fusions often preserve biochemical functions and cellular localization of the fused protein.[29]

The discovery of GFP and subsequent development into a range of wavelengths and into a variety of uses transformed the field of fluorescence microscopy. Recognizing the significance of this discovery and acknowledging the implications, the 2008 Nobel Prize in Chemistry was awarded to Osamu Shimomura, Martin Chalfie, and Roger Y. Tsien for their contributions to this field. These accomplishments made multicolor imaging possible and generated new insights into biological targets and pathways, but a different approach was needed to generate FPs with excitation and emission wavelengths in the far-red and near-infrared portion of the spectrum, a challenge for deep-tissue imaging.

1.2 Evolution of Far-Red and Near-infrared Fluorescent Proteins

As described in the previous section, fluorescent proteins revolutionized the field of cellular imaging and revealed the inner workings of cells to an extent not previously thought possible. Despite the broad availability of fluorescent proteins at a wide range of wavelengths, the generation of suitable fluorescent proteins in the far-red (FR) and near-infrared (NIR) region of the spectrum has been difficult to achieve. The longest wavelength excitation spectrum of a GFP-like fluorescent proteins is 611 nm.[21-24] This section will discuss the evolution of FR and NIR FPs from bacteriophytochromes and cyanobacterial proteins to generate a series of biliverdin-binding fluorescent proteins.

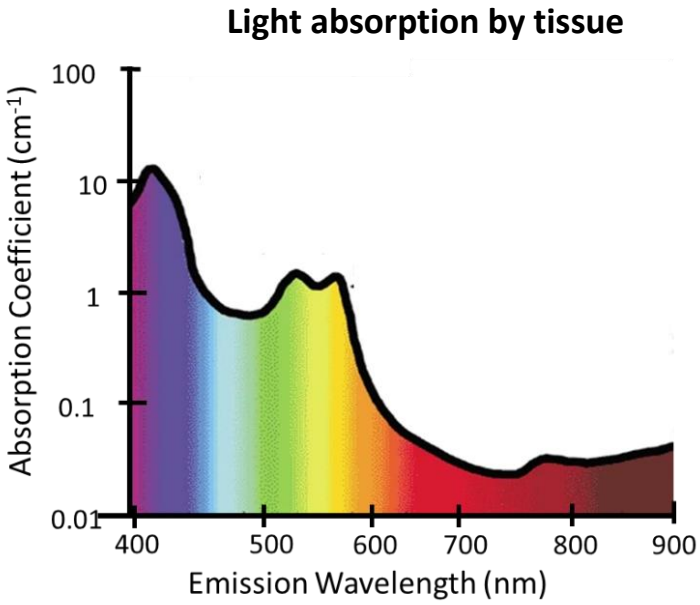

Figure 1.2 Comparison of light absorption by tissue. Figure adapted from Ref. 31. Light absorption was Calculated assuming normally oxygenated tissue, 50 mM hemoglobin, and a composition of 50% water and 15% lipids.

Deep-tissue imaging is limited by a deficiency of fluorescent proteins exhibiting excitation and emission in the far-red and near-infrared region of the spectrum. Lower absorption by hemoglobin, water, and lipids (Figure 1.2), lower tissue autofluorescence in the 650-900 nm region, and low scattering at longer wavelengths necessitates the use of far-red fluorescent proteins for imaging deeper than a few millimeters in a tissue sample.[31,32] For improved deep-tissue imaging, proteins with excitation above 600 nm and emission above 650 nm are needed.

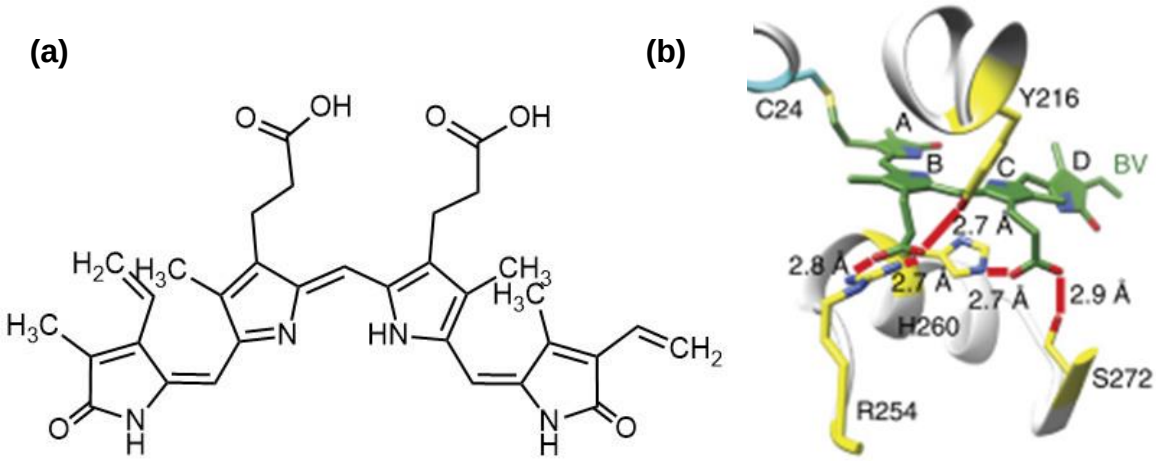

Figure 1.3 Biliverdin structure and binding (a) Biliverdin molecular structure. (b) Biliverdin within bacteriophytochrome binding pocket. Crystal structure showing BV within *Deinococcus radiodurans* (IFP1.4 parent bacteriophytochrome). Figure from Ref. 37.

Phytochromes are poorly fluorescent photoreceptors found in plants, fungi, bacteria and cyanobacteria that use tetrapyrroles as chromophores.[33] Of this group, bacteriophytochrome photoreceptors (BphPs) are the most promising precursor for far-red imaging because they have the most red-shifted absorption among the phytochomes.[34] Nearly all BphPs bind autocatalytically and covalently to biliverdin Ixα (BV, Figure 1.3 (a)) via a cysteine amino acid residue.[35,36] A crystal structure illustrating biliverdin binding within a bacteriophytochrome is shown in Figure 1.3 (b).[37] BphPs absorb light in the near-infrared, resulting in signal transductions, conformational changes, and protonation reactions of the chromophore.[33] Bacteriophytochromes are composed of the PAS, GAF and PHY domains. The absorption maximum of BphPs varies depending on the photochemical state of the molecule, exhibiting photoconversion between a red absorbing (~700 nm) and a far-red absorbing ground state (~750 nm).[33,35] This photoconversion occurs via isomerization around a C15=C16 double bond and a subsequent proton transfer process across several amino acid side chains. The

photoconversion from the red-absorbing from to the formation of an intermediate photoproduct is shown in Figure 1.4[38,39]

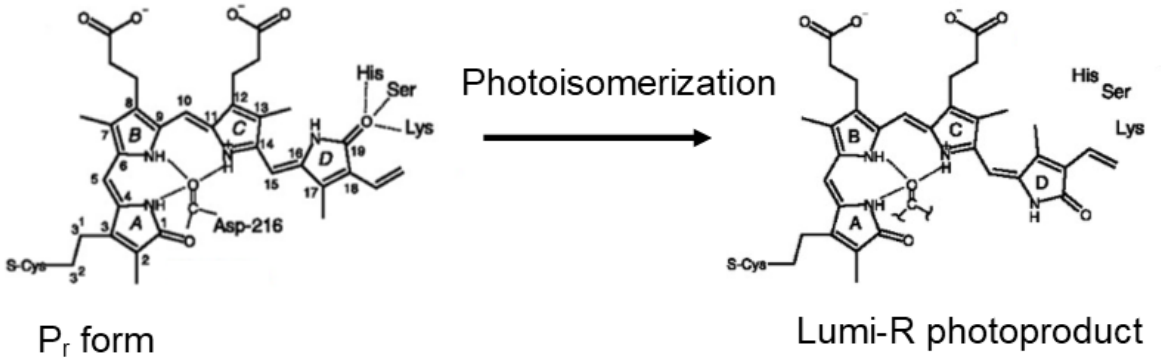

Figure 1.4. Biliverdin photoconversion reaction. The reaction results in formation of the Lumi-R photoproduct, which further reacts to form the far-red absorbing form (Pfr) in R. palustris P3 bacteriophytochrome. Adapted from Ref. 39.

Biliverdin is a flexible molecule and exhibits photoconversions in the excited state and intramolecular proton transfer in the ground or excited state. BV in solution adopts several different conformations and has a quantum yield of 10^{-4} in the far-red portion of the spectrum, and must be conformationally restricted via binding to a protein in order to induce fluorescence in this region.[40,41] Biliverdin is a byproduct of heme degradation and is abundant in eukaryotic cells, indicating BV-binding fluorescent proteins can ideally be used in mammalian cells without additional cofactors. In practice, many of these fluorescent proteins require the co-expression with heme oxygenase to produce a higher concentration of biliverdin or the addition of exogenous biliverdin to achieve bright fluorescence.[41-43]

Bright fluorescent proteins that bind biliverdin were generated by first truncating the wild-type protein to the PAS and GAF domains of a bacteriophytochrome and subsequently performing several rounds of mutagenesis. Truncation of the protein to the PAS,GAF domain in addition to mutations made around the chromophore was found to inhibit the photoconversion process and increase the quantum yield.[34,41,42] The PAS and GAF domains are necessary for effective BV incoroporation.[36,41] Initial iterations of BphP-based fluorescent proteins required exogenous BV to be added to achieve bright fluorescence,[41-43] but later versions efficiently incorporated cellular BV to produce bright fluorescence without added BV.[34,44,45] The first monomeric BphP-derived FP, IFP1.4 was dim without the addition of BV.[41] A series of dimeric fluorescent proteins were developed that demonstrated high brightness in mammalian cells without the requirement of additional BV that included iRFP670 (643/670 nm ex/em).[34] The properties of these proteins are summarized in Table 1.1.

Protein	Excitation (nm)	Emission (nm)	Quantum Yield	Extinction Coefficient (M^{-1} cm^{-1})
IFP1.4	684	708	0.07	92,000
IFP2.0	690	711	0.08	86,000
mIFP	683	704	0.08	82,000
iRFP670	643	670	0.11	114,000
miRFP670	642	670	0.14	87,400
smURFP	642	670	0.18	180,000

Table 1.1. Properties of BV-based fluorescent proteins.

Through additional mutations to a bacteriophytochrome, the monomeric protein miRFP670 is generated (Figure 1.5 a). miRFP670 was 5-times brighter than the

previously developed monomer mIFP in mammalian cells and has the highest molecular brightness of any BphP-derived fluorescent protein. It has a quantum yield of 0.14 and an extinction coefficient of 87,400 $M^{-1}cm^{-1}$, with an excitation maximum of 642 nm, and an emission maximum of 670 nm. miRFP670 is bright without additional biliverdin in mammalian cells but becomes 7-fold brighter when co-expressed with heme oxygenase.[46]

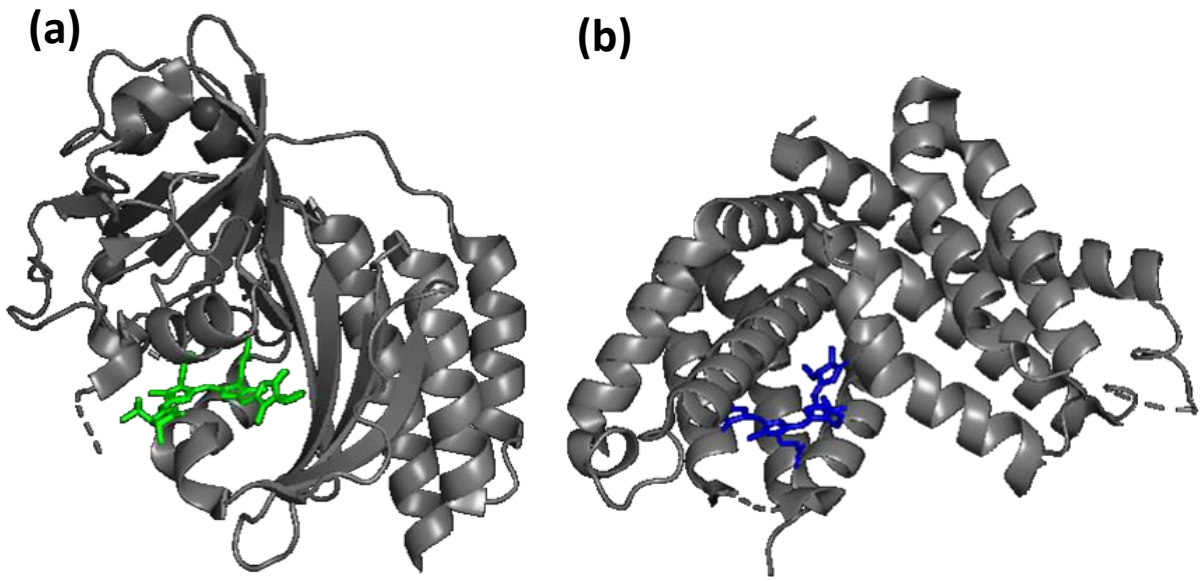

Figure 1.5. Crystal structures of miRFP670 and smURFP Y56R (a) Crystal Structure of miRFP670 with the biliverdin chromophore in green (PDB #5VIV) (b) smURFP Y56R crystal structure with the biliverdin chromophore in blue (PDB #6FZN)

smURFP (Figure 1.5 b) was evolved from an allophycocyanin (APCα) subunit from cyanobacteria.[47] APC is a light-harvesting biliprotein optimized for highly efficient energy transfer via natural evolution, resulting in a higher natural fluorescence quantum yield.[48,49] The wild-type protein covalently binds phycocyanobilin (PCB) via a cysteine residue with the help of a lyase to incorporate the chromophore.[49] The protein was evolved to attach PCB without the help of a lyase and was further evolved to bind biliverdin. Biliverdin is

preferable to PCB as a chromophore due to its abundance in mammalian cells. The resulting protein, smURFP, has the highest molecular brightness of any biliverdin-binding far-red fluorescent protein. It has a quantum yield of 0.18 and an extinction coefficient of 180,000 $M^{-1}cm^{-1}$. The excitation maximum is 642 nm, and the emission maximum is 670 nm.[47] APC-based NIR FPs show low affinity for binding BV, leading to lower effective brightness in cells. Enhancing the binding efficiency increases the fluorescence of these proteins.[50] Excitation and emission spectra for miRFP670 and smURFP (Figure 1.6) illustrate the similarities in excitation and emission for these two proteins.

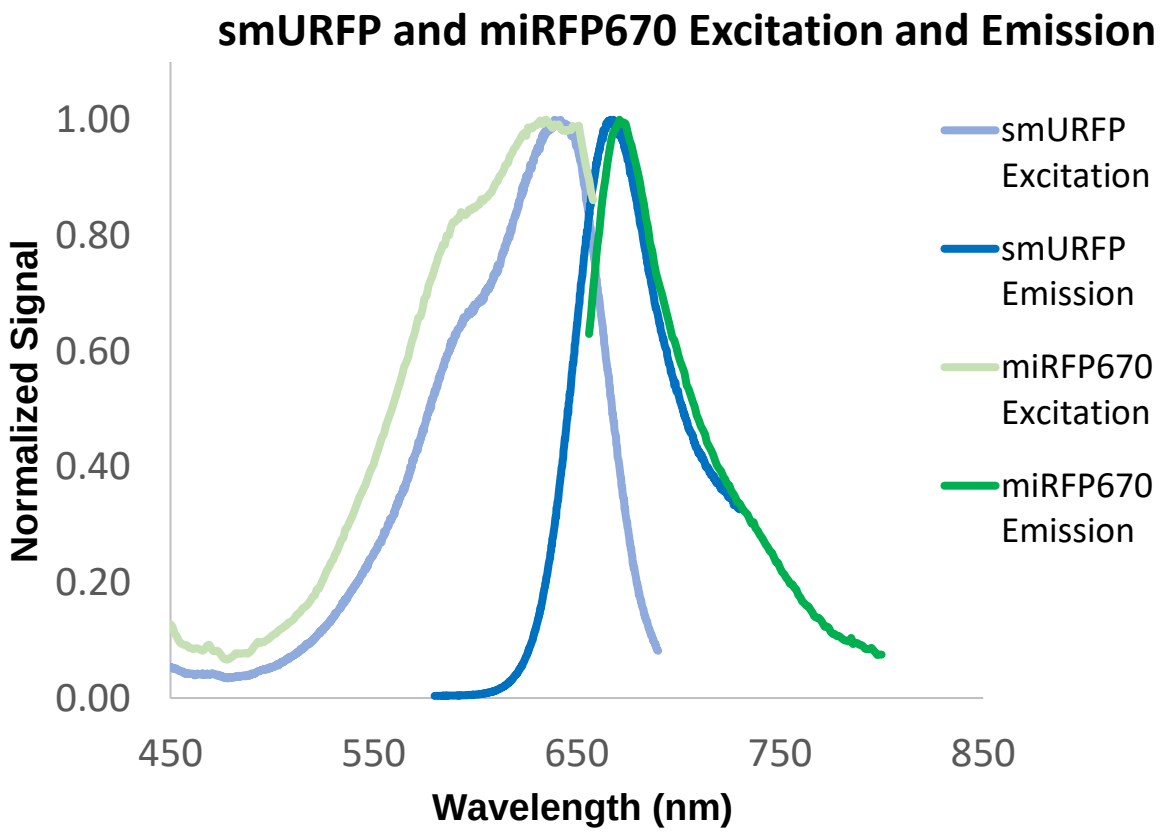

Figure 1.6. smURFP and miRFP670 excitation and emission. Normalized spectra for excitation and emission.

The crystal structure of IFP1.4 showed that a dense, hydrophobic binding pocket restricts movement of the BV D-ring and prevents C15=C16 isomerization as a relaxation pathway.[38] NIR FPs with even higher effective brightness were obtained via mutations that enhance fluorescence that may be caused by a reduction in motion of the BV A ring via van der Waals interactions and introducing a Hydrogen bond between the chromophore and protein.[50]

The utility of FR and NIR BV-based FPs has been demonstrated *in vivo* and in cells.[36,39,40] BphP-based FPs are often genetically encoded alongside a heme oxygenase gene to convert heme into biliverdin in order to increase the amount of biliverdin in cells, allowing use in cells such as *E. coli*, which possess heme but not BV.[30,32]

1.3 Fluorescent Protein Photophysics

Fluorescence occurs following excitation, when a fraction of molecules in the excited electronic state returns to the ground electronic state. Additionally, some molecules will become trapped in a long-lived dark state, and some will be permanently photobleached. The emission lifetime is the average time between excitation and return to the ground state, and is typically on the order of 10^{-9} s for fluorescent proteins, much faster than light absorption, which is on the order of 10^{-15} s.[51] This section will discuss the photobleaching and dark state conversion processes observed in fluorescent proteins, and potential mechanisms.

Fluorescence emission occurs at longer wavelengths compared to excitation in a phenomenon known as the Stokes shift. At each electronic energy level, there are several

vibrational energy levels. Molecules are typically excited from the ground electronic state from the lowest vibrational state to a higher vibrational state of S_1, since at room temperature the excited vibrational energy are not thermally populated to a significant extent. Excited molecules in condensed phase, such as proteins in solution, rapidly relax to the lowest vibrational state in ~10^{-12} s resulting in emission from a lower vibrational state of the excited electronic state to a higher vibrational level of the ground state. Other factors that further decrease emission energy relative to excitation include solvent relaxation effects, conformational changes, and excited state proton transfer. [51]

Brightness is a key factor determining the utility of fluorescent proteins, influencing the lowest concentration that can be used in experiments as well as the sensitivity and contrast from background fluorescence in live cells.[52,53] Brightness can be expressed as either molecular brightness or cellular brightness. Molecular brightness determines the fluorescent protein performance in solution and is defined as the product of extinction coefficient and fluorescence quantum yield ($M_b = \varepsilon \cdot \phi$). Equation 1.1 describes how fluorescence quantum yield is calculated. Cellular brightness refers to the brightness of fluorescent proteins within cells and is dependent on the molecular brightness in addition to protein expression level, protein folding, and intracellular folding and stability of the protein (sensitivity to pH, ionic strength, etc.). For the NIR FPs, chromophore affinity and specificity is an additional concern for cellular brightness, with some NIR FPs exhibiting higher molecular brightness, but lower cellular brightness.[46,47,50,54,55] This effect occurs due to competition between biliverdin and related molecules for the binding site for the FP apoprotein.[56,57]

$$\phi = \frac{k_r}{k_r + k_{nr}}$$

Equation 1.1. Quantum yield. Ratio of emitted photons to total number absorbed. k_r is the radiative rate constant and k_{nr} is the rate constant for non-radiative decay.

Another key factor determining fluorescent protein utility is photostability, the ability of fluorescent proteins to absorb and emit photons while resisting photoreactions that lead to degradation. A photobleached molecule no longer produces fluorescence. Mechanisms for photobleaching have been characterized in various fluorescent dyes and in select fluorescent proteins but have yet to be characterized in NIR FPs.

One mechanism that has been proposed for photobleaching in certain dyes and fluorescent proteins is photoreaction via a dark triplet state. Both small molecule dye Rhodamine 6G and fluorescent proteins EGFP, EYFP, DsRed, and mCherry have shown evidence of photobleaching occurring via a triplet state and leading to photoproduct formation.[58-62] Rhodamine 6G photobleaching involves a multistep photoreaction from the triplet state that results in radical anion.[59-61] Single-molecule spectroscopy on EYFP, EGFP, and DsRed similarly supported a mechanism of multistep reaction from the triplet state and leading to photoproduct formation.[62] These measurements on EGFP, EYFP, and DsRed reported photobleaching time constants of 2.8 ± 0.2 ms, 3.5 ± 0.5 ms, and 0.4 ± 0.1 ms at saturating irradiances of 13 ± 3 kW/cm^2, 6 ± 1 kW/cm^2, and 50 ± 10 kW/cm^2, respectively.[62] The single-molecule results were reinforced by a fluorescence correlation study that also found EYFP to be more photostable than EGFP.[63] Fluorescence measurements on mCherry reported photobleaching time constants of 3.5 ± 0.7 s and 57.0 ± 4.6 ms at 2.5 and 25 kW/cm^2 respectively.[58]

Photobleaching via a singlet state has also been proposed as a mechanism in some fluorescent dyes. A fluorescence correlation spectroscopy study of photobleaching of fluorescein and borondipyrromethene (BODIPY) dyes determined that bleaching for these dyes occurred primarily via an excited singlet state, by comparing rates of photobleaching and rates of intersystem crossing in multiple of these dyes.[64]

In addition to irreversible photobleaching, fluorescent proteins also exhibit reversible loss of fluorescence, known as dark state conversion (DSC). Dark state conversion is a light-driven, reversible process. A fluorescent protein in the initially excited electronic state enters a dark (nonfluorescent) state. The process by which the excited state of a fluorescent protein returns to the ground state is called Ground State Recovery (GSR). Once a fluorescent protein has returned to the ground state, it can resume fluorescing. The steady-state population of molecules in the dark state is determined by the rate at which the molecule enters and exits the dark state.

A three-level system diagram depicts the cyclic process of excitation, emission, with the possibility of entering and exiting the dark state as well as photobleaching (Figure 1.7). Previous studies of fluorescent proteins photophysics have employed three-level,[65,66] four-level,[58,67,68] and more complex models[69] to describe the photophysics of various fluorescent proteins. The four-state model includes two anionic and two neutral states of the chromophore, with the neutral forms designated nonfluorescent. and was initially proposed by Dickson et al to describe single-molecule observations of a GFP variant.[68] An analogous model was used to interpret fluorescent measurements on RFPs, with two bright and two non-fluorescent states, with the dark states interpreted as a combination of neutral and isomeric states of the chromophore. This model agreed with

experimental findings of a linear relationship between dark state fraction and DSC time constant for the RFPs studied.[58] A similar four-state model was used to describe TagRFP-T fluorescence results with two fluorescent and two dark states.[67] Another study found a three-state model with a bright ground and excited state and a dark state was sufficient to describe fluorescent measurements on several RFPs.[65] A similar three-level model with 2 bright and one dark state was used to describe the flickering dynamics observed from FCS experiments on red fluorescent protein eqFP611.[66] Sinnecker et al proposed a mechanism with a protonated form, deprotonated form, and a dark form to describe the kinetics observed in fluorescence correlation spectroscopy (FCS) measurements of ECFP and EYFP.[69] A model with fewer states such as the three-level model may be more practical to use, it also risks simplifying the complex photophysics in the dark state. On the other hand, a more complicated model with several levels may have so many parameters as to risk overinterpreting the data. In practice, we will use the three-level model as a starting point to interpret our data since it can combine multiple dark state processes into one state. This is done in an effort to use the simplest model that can describe experimental observations.

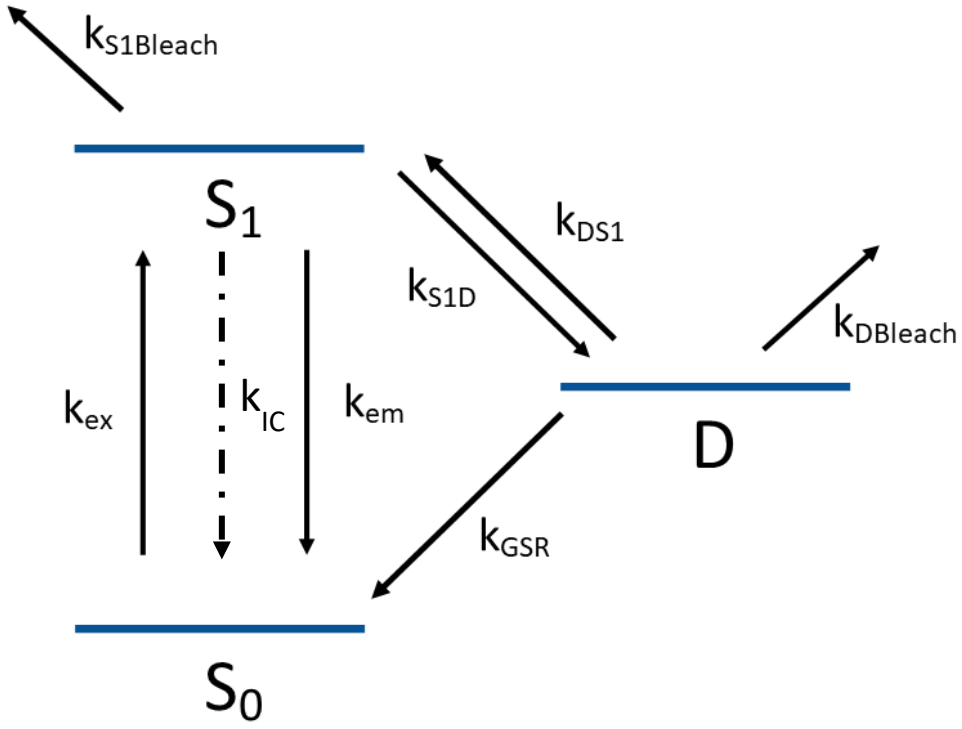

Figure 1.7 Three-level system diagram. The ground state (S_0), the first excited state (S_1), and D indicating a dark state. k_{ex} is the excitation rate constant, k_{em} is the emission rate constant, $k_{S1Bleach}$ and $k_{DBleach}$ are the bleaching rate constants, and k_{DS1}, k_{S1D}, and k_{GSR} are the rate constants for entering and exiting the dark state.

Many of the photophysical parameters used to describe fluorescent proteins are interrelated. A higher dwell time in the dark state conversion results in lower fluorescence brightness and lower quantum yields, since a greater fraction of the molecules is nonfluorescent at any given observation time. The relatively low quantum yields of RFPs mCherry, mRuby2, and mKate has been linked to the relatively large fraction of molecules in the dark state compared to mScarlet, an RFP with a much higher quantum yield.[70] A correlation between excitation rate and sensitivity to irradiance of reversible and irreversible photobleaching rate constants has been demonstrated in RFPs.[58] As a result, when comparing photophysical properties of different fluorescent proteins, it is necessary to do measurements at the same excitation rate to accurately compare relevant

parameters. Excitation rate (Equation 1.2) is dependent on extinction coefficient and irradiance. Irradiance is reported as power divided by area (e.g. kW/cm^2) and is a measure of excitation intensity.

$$k_{ex} = \frac{\ln(10) \cdot 1000 \cdot \varepsilon \cdot \lambda \cdot I}{h \cdot c \cdot N_A}$$

Equation 1.2. Excitation rate, k_{ex}. ε is the extinction coefficient. λ is the wavelength. I is the irradiance, h is Planck's constant, c is the speed of light, and N_A is Avogadro's number. This calculation is an average for k_{ex} over the volume illuminated based on the irradiance calculation

Among fluorescent proteins that exhibit conversion to the dark state, fluorescent proteins exhibit a variety of mechanisms for entry into the dark state, including electron-transfer reactions[71,72], chromophore conformational changes,[71-73] reactions via a triplet state,[71,72] and excited-state proton transfer.[69,74-76] Dark state conversion and ground state recovery processes have been reported on timescales ranging from hundreds of microseconds to seconds.[76-79]

Several fluorescent proteins were found to exhibit dark state conversion that could be attributed to proton transfer reactions. Proteins undergoing these reactions include both variants of GFP and a protein derived from a sea anemone. Fluorescence studies of several GFP variants found that ECFP, EGFP, EYFP, and Citrine exhibited light-driven dark state conversion that increased at lower pH values in both cells and solution.[69,76] For these proteins, return from the ground state is spontaneous, but it can be accelerated by light. This pH dependent effect was attributed to proton transfer between amino acid residues exposed to the surrounding solution and the chromophore, whereas at high pH internal proton transfer is thought to be predominant.[69,76] Timescales for dark state

conversion range from 2.4 s for ECFP, 130 s for EYFP, and 28 s for Citrine at irradiances of 2.5 W/cm^2 for ECFP and 2.35 W/cm^2 for EYFP and Citrine.[69] In contrast with these variants derived from GFP, DsRed exhibited pH-independent (4.4-9.0 range) light-driven dark state conversion.[74] Excitation-dependent, pH-independent flickering observed in both DsRed and Citrine indicated the presence of an additional dark state, distinct from the protonated dark state observed in many GFP variants.[74] Blinking of dsRed and Citrine was reported on the timescale of hundreds of μs for the irradiance range 0.4-7.3 kW/cm^2.[74,80] The T203Y and T203F mutants of GFP exhibited both the pH-dependent and light-dependent dark state conversion effects discussed above. Flickering from these proteins was observed over a μs-ms time scale for irradiances from 0.6-5000 kW/cm^2.[75]

Dark state conversion occurring via conformational changes in the chromophore has been observed in IrisFP, a protein derived from a coral protein. X-ray radiolysis was used to generate a radical dark state. This indicates that intermolecular electron transfer affects the blinking of IrisFP.[71] Quantum Mechanics/Molecular mechanical calculations on IrisFP indicated two mechanisms from which the distorted chromophore dark state can arise. The two mechanisms involve a proton transfer reaction that can occur via a triplet state or a radical ground state and results in a distorted chromophore with disrupted π-conjugation, resulting in loss of fluorescence.[72] Both mEos2 and Dendra2 also show evidence of dark state conversion via chromophore distortion and twisting motions.[73]

Blinking timescales also give indications of the mechanism behind dark state conversion.[81] Fast blinking behavior (tens of microseconds to ms) has been attributed to conversion to a triplet state, while slower blinking (0.1-10s range) is associated with excited-state conformational dynamics.[73] mCherry and TagFPP-T have blinking reported

on the sub-ms to ms timescale.[65] eqFP611 was found to have blinking on two timescales, a fast 300 μs timescale and a slower blinking on a 10 ms timescale.[66]

Blinking refers to the phenomenon of individual fluorescent protein molecules entering the dark state and then returning to an emissive state. Blinking of fluorescent proteins was first observed in a study of single molecules green fluorescent protein.[68] Single molecule measurements enabled visualization of this phenomenon that is obscured in ensemble experiments. Single molecules of GFP were discovered to turn on and off several times over a timescale of seconds, eventually entering a long-lived dark state in which no emission is observed.[68] A blinking trajectory for a single fluorescent molecule shows it alternating between on and off states with lifetimes τ_{ON} and τ_{OFF}, respectively (Figure 1.8). Equations 1.3 and 1.4 show how the on- and off-times can be calculated based off the rate constants for dark state conversion (DSC) and ground state recovery (GSR), respectively. Histograms of single molecule trajectories with on and off times can be constructed to determine average behavior. Fluorescent proteins with short dark state lifetimes will blink on and off several times within an observation period. The average number of blinks that can be observed is the ratio of the rate constant for conversion to the dark state compared to the rate constant for irreversible photobleaching. (k_{DSC}/k_{Bleach}).[73]

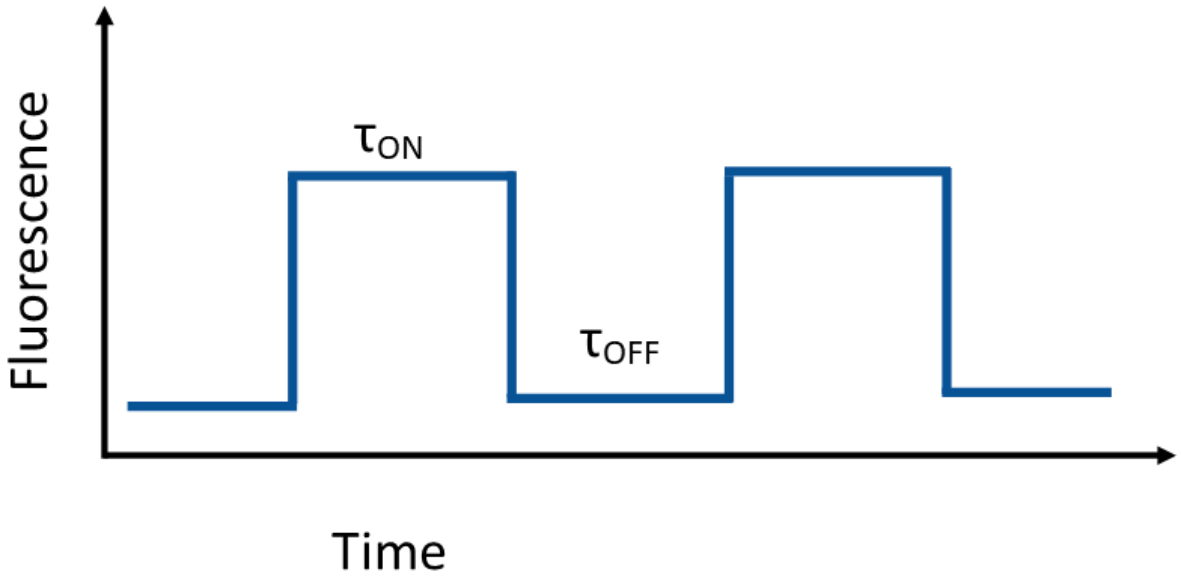

Figure 1.8 Fluorescence trajectory for a single fluorescent molecule. τ_{ON} is the time the molecule spends fluorescing, and τ_{OFF} is the time the molecule spends in the dark state.

$$\tau_{on} = \frac{1}{k_{ex} * k_{DSC} * \tau_{em}}$$

Equation 1.3. Equation to calculate the on time (τ_{on}) for a fluorescence trajectory. k_{ex} is the excitation rate constant, k_{DSC} is the dark sate conversion rate constant, and τ_{em} is the fluorescence lifetime.

$$\tau_{off} = \frac{1}{k_{GSR}}$$

Equation 1.4. Equation to calculate the off time (τ_{off}) for a fluorescence trajectory. k_{GSR} is the ground state recovery rate constant.

Photoswitchable fluorescent proteins exhibit highly efficient transfer to the dark state, allowing the molecules to be switched on and off between nonfluorescent and fluorescent states. A fluorescent molecule in the “on” state can be switched off through light-driven conversion into a nonfluorescent or “off” state. Photoswitching is caused by reversible conversion between these on and off states.[82] Studies have demonstrated that pulsed excitation with a carefully selected frequency can be used to depopulate the dark

state or ensure relaxation to the ground state between pulses and thus increase fluorescence.[83-85] Optical depopulation of dark state population has been utilized to increase the measured fluorescence signal of FPs, resulting in improved sensitivity and selectivity for imaging, as demonstrated with AcGFP[86] and protein rsFastLime.[85]

Depending on the application, the dark state can be a hindrance or a benefit. When high brightness over long, uninterrupted time intervals is needed such as cellular tracking experiments, a fluorescent protein with little to no dark state conversion would be preferable. The super-resolution techniques discussed in the next section utilize the dark state to generate imaging resolution above the diffraction limit. Understanding dark state photophysics can help guided evolution of fluorescent proteins by informing which mutations can be linked to dark state conversion. Improved knowledge of dark state behavior for a range of FPs allows evaluation of the utility of those FPs for imaging techniques to determine whether the FP is better suited for cellular tracking experiments or for super-resolution imaging techniques. The next section discusses super-resolution imaging techniques and how they take advantage of dark state conversion.

1.4 Advances in Super-Resolution Imaging

While microscopy using fluorescent proteins is a powerful technique for imaging living systems, standard light microscopy techniques could not distinguish emitters below 200 nm until the 1990s when techniques were introduced that used the dark state to overcome this limit. This diffraction limit was first described by Ernst Abbe in 1873 as the closest distance that two objects can be and still be distinguishable (Equation 1.5).[87] As

a result of this limit, objects smaller than approximately half a wavelength of light cannot be resolved with traditional fluorescence microscopy techniques, preventing detailed observation of subcellular objects below this size. This section discusses several of these techniques, referred to as super-resolution imaging, and how they utilize the dark state to overcome the diffraction limit.

$$\Delta x \geq \frac{\lambda}{2nsin\alpha}$$

Equation 1.5. Diffraction limit. Δx is the distance between two objects that can be distinguished. n is the refractive index. α is the aperture angle under which the point source is observed. nsinα is also known as the numerical aperture of the lens.

A key achievement in the development of super-resolution capabilities was the successful detection of single molecules. This work was pioneered by W.E. Moerner in 1989 when he successfully detected absorption of single molecules of pentacene in a *p*-terphenyl crystal.[88] Single-molecule fluorescence is observed when only one molecule is present within the irradiating volume, and when the signal from that molecule is larger than the background signal.[89] Single-molecule methods were used to reveal photoswitchable behavior of GFP in 1997, which demonstrated the first use of a room temperature photoswitchable molecule.[68] Ensemble measurements observe behavior of a large number of molecules and report the average value of parameters across the whole group, whereas single-molecule studies report on parameters of individual emitters. Effective use of single-molecule fluorescence requires knowledge of total number of photons a fluorescent molecule can emit on average and rate of fluorescence, which is affected by trapping in dark states. Additionally, single molecule signal is weak and easily

lost in the background.[89] Utilization of single molecule techniques and photoswitchable molecules is essential for the localization-based super-resolution techniques.

Stefan W. Hell and Jan Wichmann introduced a method in 1994 to overcome the diffraction limit using pointillistic scanning technique with shaped beams and Hell implemented the technique in 2000.[90,91] This technique, Stimulated Emission Depletion (STED) fluorescence microscopy, requires the use of a saturable molecular transition to inhibit fluorescence in a limited area, resulting in higher resolution. This is achieved by using light of one wavelength to excite the sample, and a second beam to saturate the transition, reducing the number of excited molecules. The second beam of light inhibits fluorescence everywhere except the innermost region of the sample, so only this innermost region can contribute to the fluorescence signal.[90] The initial application of this technique required irradiances in GW/cm^2 to suppress fluorescence sufficiently to reach sub-diffraction limit resolution.[91] Ground-State Depletion (GSD) fluorescence microscopy is a related technique that overcomes the diffraction limit by depleting the ground state of molecule in the outer region of the focus by using high intensity irradiation (MW/cm^2) to quickly cycle molecules between excitation and emission, with a fraction caught in the dark state each time. The reduced number of excitable molecules leads to a decrease in full-width half maximum (FWHM) and an increase in resolution.[92] Reversible Saturable Optical Fluorescence Transitions (RESOLFT) is an iteration of this technique which has achieved resolution as low as 30-40 nm with irradiances on the scale of W/cm^2 by selecting saturable processes and fluorophores that require lower intensities, using reversible photoswitches in this case.[93]

In 2006, two similar super-resolution fluorescence microscopy localization techniques were developed independently of one another, Photoactivated Localization Microscopy (PALM) proposed by Eric Betzig and Stochastic Optical Reconstruction Microscopy (STORM) proposed by Xiaowei Zhuang. Both methods were demonstrated to achieve ~20 nm resolution.[94,95] Both techniques use the selective localization of sparse subsets of fluorophores in which only one molecule in a diffraction limited volume is localized at a time. This is done through switching fluorophores on for localization with one wavelength of light, and then switching them off with another wavelength of light. Through repetitive cycles of imaging, a total image with nanometer resolution can be reconstructed. The set of fluorophores that are turned on at any time is controlled so that there is no overlap, and no two within a diffraction-limited volume are on at the same time[94,95] This can theoretically be done with any fluorophore that exhibits blinking, but photo-switchable ones are the most straightforward to use for this application.

Super-resolution Optical Fluctuation Imaging (SOFI) was first published in 2009 and obtained resolution beyond the diffraction limit in all three dimensions.[96] SOFI requires less sophisticated equipment compared to STED, PALM, and STORM, using only a widefield microscope and CCD camera, compared to the requirement of total internal reflection fluorescence (TIRF) microscopy and an EMCCD camera for single molecule for PALM and STORM.[94-96] SOFI uses statistical analysis of temporal fluctuations caused by fluorophore blinking to enhance contrast over a series of images. This process is illustrated in Figure 1.9. The resulting super-resolution image is virtually background-free and is collected from seconds of acquisition time, improving upon temporal resolution compared to PALM and STORM.[96] Successful application of SOFI

requires a label with two spectrally distinct emission states, the label must switch between these two states independently and stochastically, and the pixels used should be smaller than the diffraction limit.[96]

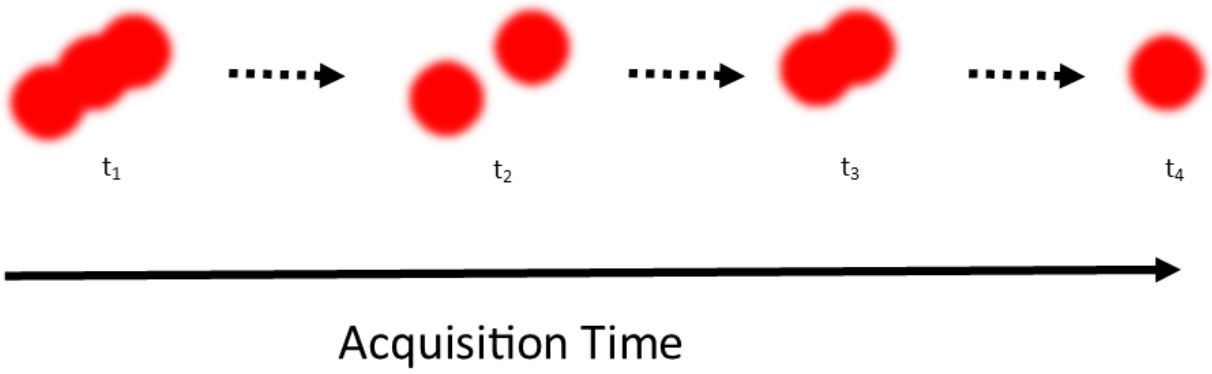

Figure 1.9 Illustration of image collection through SOFI. At time t_1, three fluorophores are shown in the ON state, too close to exactly localize all three of them. At time t_2, the middle fluorophore is in the OFF state, and the other two fluorophores are in the ON state and separated enough so that they can be localized. At t_3, the fluorophores in the ON state are too close for localization. And finally, at t_4, only the middle fluorophore is in the ON state, so it can be localized.

Super-resolution microscopy techniques have fundamentally changed the limits of fluorescence microscopy. In recognition of this influence, the 2014 Nobel Prize in Chemistry was awarded to Eric Betzig, Stefan W. Hell, and William E. Moerner for their role in developing the super-resolution microscopy techniques mentioned above. Since its development, super-resolution has enabled the imaging of sub-cellular structures at resolution above the diffraction limit.[71,72,75] SOFI is an especially promising technique, given its lower requirements and simple collection protocol. Utilizing fluorescent proteins as the probes in this technique further enhances its capabilities, minimizing perturbations to the biological substrates being imaged. While the biliverdin based fluorescent proteins

have not been used in super-resolution imaging, better understanding of their dark state photophysics can be used to extend the wavelength range available for these techniques.

1.5 Thesis Objectives

As outlined in the above sections, the discovery of fluorescent proteins and the development of super-resolution microscopy have greatly advanced knowledge of subcellular biological processes. Despite these advances, deep-tissue imaging is limited by the low quantum yields and low brightness of near-infrared fluorescent proteins. Improved understanding of these fluorescent proteins and their dark state photophysics is necessary to improve their utility. Knowledge of the dark state photophysics of these proteins would enable application to super-resolution spectroscopy techniques such as PALM and SOFI and would also allow illumination settings to be controlled to minimize dark state populations. While near-infrared fluorescent proteins are not currently used for super-resolution spectroscopy, a better understanding of the mechanisms controlling blinking in these FPs can allow them to be further developed for this purpose.

This work seeks to characterize the dark state photophysics of two far-red fluorescent proteins, smURFP and miRFP670. smURFP has the highest molecular brightness of any far-red fluorescent protein, and miRFP670 has the highest molecular brightness of any bacteriophytochrome-based far-red fluorescent protein. To perform these time-resolved fluorescence measurements reproducibly and efficiently, a microwell device protocol was developed and characterized.

Chapter 2: Design and Fabrication of Microwell Devices

2.1 Introduction

During a time-resolved fluorescence experiment, fluorescent proteins may diffuse throughout the sample. Diffusion can introduce adverse effects into measurements of dark-state and photobleaching time constants, since a bleached protein or a protein in the dark state may diffuse out of the irradiated area, or an unbleached protein may diffuse in, artificially inflating the measured fluorescence signal. For experiments over a long time period, it is essential to confine the fluorescent proteins within the irradiated area to collect accurate measurements. This chapter discusses the methods developed to confine proteins within a measurement area.

Whether or not a fluorescent protein remains in the irradiated area over the course of measurements can be evaluated using the Stokes-Einstein equation for diffusion. The Stokes-Einstein equation (Equation 2.1) describes diffusion for a spherical particle in solution. This equation can be used to obtain approximate values for the diffusion coefficients of fluorescent proteins in solution, using the hydrodynamic radius calculated from the molecular weight of each protein.

$$D = \frac{RT}{N_A 6\pi n a}$$

Equation 2.1 Stokes-Einstein equation to calculate diffusion coefficient. This equation assumes that particles are spherical. R is the gas constant, T is temperature in Kelvin, N_A is Avogadro's number, n is the viscosity of the solution, and a is the hydrodynamic radius of the spherical particle.

Using this equation, the far-red fluorescent proteins smURFP and miRFP670 studied have diffusion coefficients of approximately 107 $\mu m^2/s$ and 102 $\mu m^2/s$ respectively. To assess this approximation, the diffusion coefficient was calculated for GFP using the same method, and found a diffusion coefficient of 117 $\mu m^2/s$. This value was compared to the experimentally determined diffusion coefficient for GFP in solution, 87 ± 2 $\mu m^2/s$, indicating the calculation is off by 30%.[97]

The displacement of the proteins during the timescale of a measurement can be calculated using Brownian dynamics (Equation 2.2). Over the course of a ten second measurement, smURFP and mCherry will on average travel 65 µm and in the same measurement time, miRFP670 will on average diffuse 64 µm. The calculated displacements were then compared to the full width at half maximum (FWHM) for the laser beam to determine the extent to which diffusion will affect measurements. For the beam used for my fluorescence measurements, the FWHM ~30 µm, half the distance that a protein will diffuse within a short measurement. Even assuming the diffusion coefficients are ~30% lower than calculated, miRFP670 would be expected to diffuse 53 µm within a ten second measurement, greater than the 30 µm beam diameter. This indicates that unless samples are confined, protein diffusion into and out of the irradiated area will occur during these measurements, affecting the calculated time constants. To prevent such artifacts from affecting the data, several methods of protein confinement were considered.

$$< x >= \sqrt{4Dt}$$

Equation 2.2 Equation for root mean squared displacement in 2-dimensional space. Describes a molecule diffusing in 2-dimensional space according to Brownian motion. 2-dimensional motion is a good approximation for proteins in solution between coverslips.

Initially I utilized octanol microdroplets as a method of protein confinement, a technique that was first introduced by Patterson and coworkers in 1997 for characterization of fluorescent proteins.[98] Microdroplets have been used to measure photoconversion and photobleaching of fluorescent proteins.[99-102] The weaknesses of this technique include the random distribution of droplets on a coverslip and the wide range of droplet sizes produced, making it ineffective for characterizing the photophysics of the far-red fluorescent proteins within our experimental setup. Due to these concerns microwell arrays were investigated as an alternative method for protein confinement. This chapter discusses the drawbacks of using droplets, the challenges related to the optimization of the design, fabrication, and use of microwell devices, and a discussion of the evaluation of microwell devices.

2.2 Droplets for Protein Confinement

Droplets are generated using dye or protein in solution and 1-octanol as a means of confining fluorescent molecules through phase separation between water and 1-octanol. To prepare a droplet sample of fluorescent protein a 1:9 ratio of protein in buffer solution is mixed with 1-octanol and is then deposited on a corner of a coverslip.[77] Once prepared, these samples will have many droplets filled with purified protein solution inside the imaging area with diameters ranging from 5-200 μm (Figure 2.1A). By adding the

solution to one corner of the coverslip, the droplets within the imaging area are spaced as far apart as possible. This minimizes the likelihood that fluorescence from nearby droplets contributes to fluorescence signal.

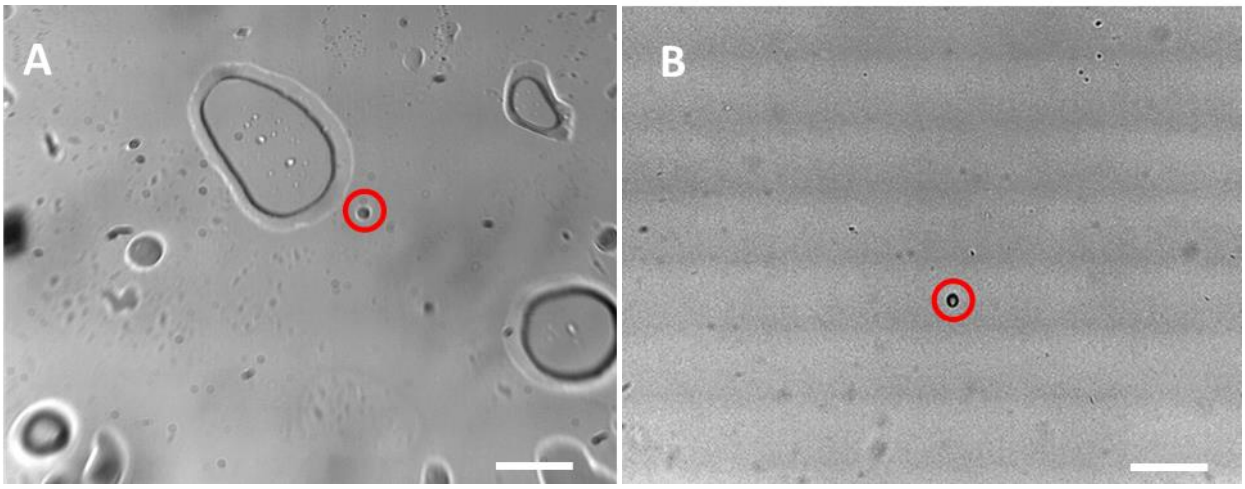

Figure 2.1 Droplet and Microwell Images (A) Droplet and (B) Microwell samples as viewed under brightfield illumination and collected by a cMOS camera under 20x magnification. The droplet picture is contrast-enhanced for clarity. Circled in red is the portion of the image that will be centered in the laser beam for measurement. Scale bar is 100 µm.

Within the sample on the coverslip, selected droplets must have the right size and must not appear to be near any other droplets to be used in a measurement. Distance to the nearest neighboring droplet is an important consideration when selecting a spot for fluorescence measurement because proteins in nearby droplets illuminated by scattered laser light will contribute to the background fluorescence signal. A portion of the proteins within that neighboring droplet will be bleached or converted to the dark state, distorting results if the adjacent droplet is used for a later measurement. To have the right size for a measurement the droplet must be small enough fit within the beam so that diffusion into and out of the irradiated area does not affect fluorescence signal. Droplets must also be

large enough that fluorescence signal is high at the selected protein concentration. Once a droplet is selected it is centered within the beam and measured.

While droplets have been useful to confine proteins in many studies,[98-102] they were found to be ineffective for fluorescence measurements of far-red fluorescent proteins. Once a droplet sample is prepared, there is no guarantee how many droplets within the sample will meet the size and spacing specifications discussed above. The droplets produced have a range of sizes, with a low percentage of droplets below 30 μm in diameter. Since the FWHM of the beam at the sample is ~ 30 μm in our setup, this means very few droplets will fit within the beam. An additional concern is the random distribution of droplets within a measurement area. Generating enough data to compare across multiple types of fluorescent proteins and irradiances requires multiple droplet samples to be prepared over the course of an experiment. In addition, the process of scanning the sample for droplets of appropriate size and spacing is very time-consuming. Since smURFP has been reported to dimerize and bind 1-2 biliverdin chromophores and miRFP670 possesses two binding sites, it was necessary to devise a more rigorous technique to control for artifacts and ensure variability in signal is linked to the fluorescent proteins themselves.[37,46] This new technique should also have samples arranged efficiently to minimize the amount of time lost searching the sample for good measurement spots.

After considering alternative options for sample preparation such as functionalizing the surface of the coverslip or containing samples within liposomes, microwells were determined as the best means of addressing the challenges encountered with droplets while not altering protein behavior. Microwells are an array of cylindrical cavities with

diameters on the order of microns molded out of polydimethylsiloxane (PDMS). A microwell device is depicted in Figure 2.2 below. Utilizing microwells instead of droplets would ideally reduce uncertainty associated with measurements by increasing control over several variables including measurement volume and spacing between measurements.

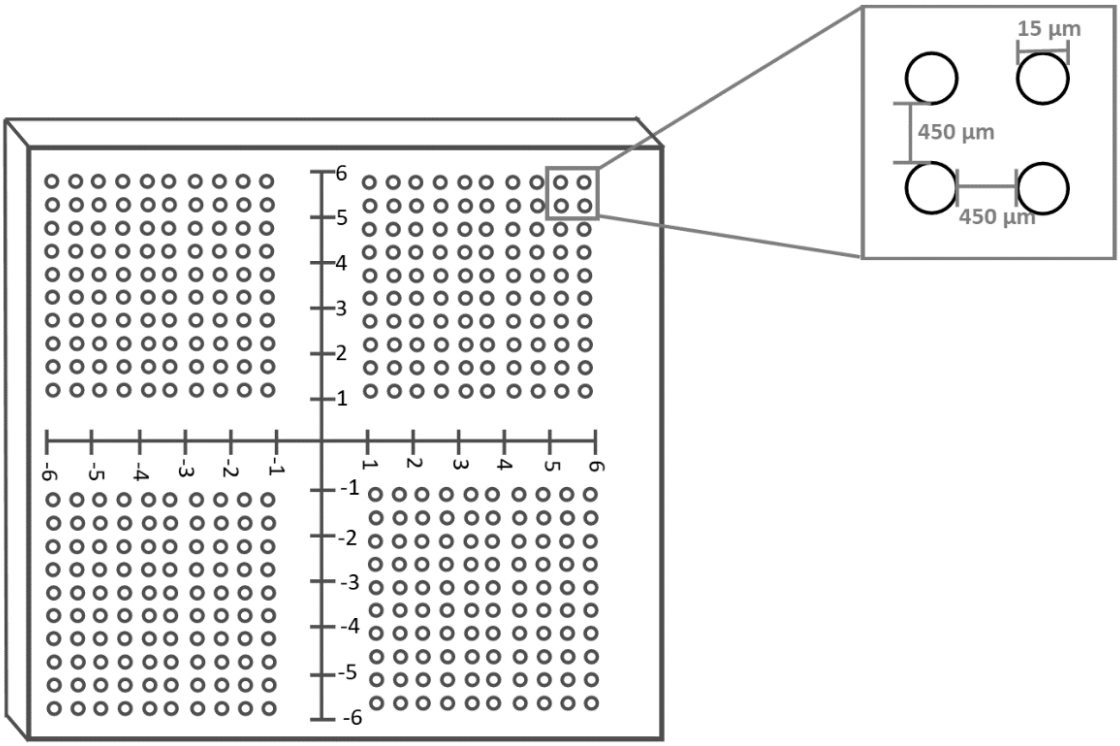

Figure 2.2 Depiction of a single microwell device. Scale bar and outer box makes it easier to locate microwells under 20x magnification. Each quadrant contains 100 microwells. The tick marks are spaced at 1 mm intervals and the entire box is 13 mm x 13 mm.

2.3 Optimization of Microwell Device Design

The utility of microwell devices has been demonstrated for quantitative study of reaction products of a single enzyme, single cell analysis, and use in sandwich

immunoassays.[103-105] The wells on these devices each has identical dimensions on the micrometer scale and has a volume on picoliter scale. Fabrication of these devices allows precisely controlled measurement volumes and spacing.

Our research group possessed a microwell master mold that was used by past lab members and could be used as a starting point for microwell tests. This original design was an array of 1000 wells, each 8 μm in diameter and spaced 10 μm apart with ~10 μm well depth. The close spacing of wells on this design permitted multiple microwells to appear in one field of view on our microscope, unlike the single microwell visible in Figure 2.1 (b). Each device was filled with 2 μL of protein by gently pressing PDMS onto a coverslip with protein on it.[106] These microwell master molds were used to generate PDMS microwell devices for testing. Initial fluorescence measurements determined these microwells were too close together for my measurements, and fluorescence from nearby microwells would significantly contribute to signal. I addressed this problem by designing microwell templates with wider spacing and with wells in a variety of diameters to use for the next phase of testing.

In the first stage of the microwell redesign I placed the wells 50 μm apart. Microwell devices with diameters of 10, 15, 20, 25, and 30 μm were prepared to ascertain the best diameter to use for fluorescence measurements. Each master had a 100 x 100 array of microwells, ensuring each device would contain enough wells for repetitive measurement. After several test measurements using fluorescent proteins to fill the wells, it was determined the wells should be spaced even further apart to minimize the irradiance exposed to nearby wells. A calculation of beam irradiance 50 μm from the center of the beam determined that nearby wells would be irradiated with 20 W/cm^2 when the irradiance

at the center of the beam is 814 W/cm^2, the lowest power setting used. For the highest power setting used, the irradiance measured 50 µm away is 540 W/cm^2. To minimize this irradiance, spacing was increased to 450 µm since this distance is greater than 10-fold higher than the beam diameter, reducing the irradiance felt by nearby wells by 54% compared to the previous design. The sparsely arranged wells were generated in a 22 x 22 grid since there was no longer enough space on the template for 1000 wells per device.

Testing of microwells ranging from 10-35 µm in diameter with 450 µm spacing between them revealed that a diameter of 15 µm was the minimum needed to generate a fluorescence signal 10-fold above the blank with 30 µM smURFP solution. For the 30 µm beam used for these experiments, the maximum microwell size that should be used is 15 µm. This ensures that the well fits within the full width at half maximum (FWHM) of the laser profile. The technique for centering the microwell within the beam is shown in Figure 2.3. Molecules within the FWHM of the beam are irradiated at nearly identical laser intensity, and for the purposes of these experiments the irradiance within this area can be treated as constant. By using the largest well diameter that receives a uniform irradiance, the signal to background ratio is maximized. Based on this analysis, all future microwell designs were only made for 15 µm. For test measurements, irradiances of 1.4 kW/cm^2 were used. Later modification to the setup by replacing the PMT with one with higher sensitivity in the far-red fluorescent protein emission range enabled the same procedure to be done with lower fluorescent protein concentrations (~10 µM protein concentrations).

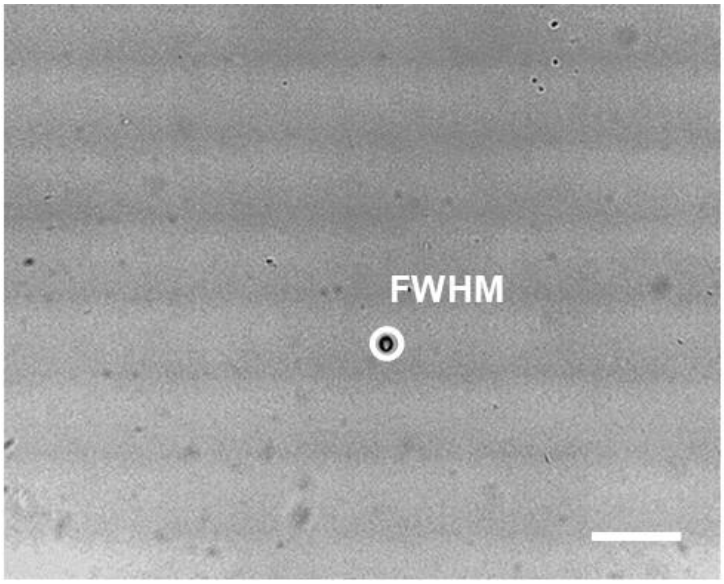

Figure 2.3 Picture of a single microwell within a laser beam. The full width at half maximum (FWHM) of the beam is depicted as a white circle with a 30 µm diameter, corresponding to the experimental settings. The microwell is 15 µm in diameter. Scale bar is 100 µm.

After these microwell masters were used for experiments and evaluated repeatedly over the course of a year, it was found many of the microwell masters were worn down and were no longer usable. While this was a setback for the project, it was taken as an opportunity to redesign the microwells for further improvement of the design. This was the final iteration of the microwell device design, and a depiction of the ultimate device template is shown in Figure 2.4.

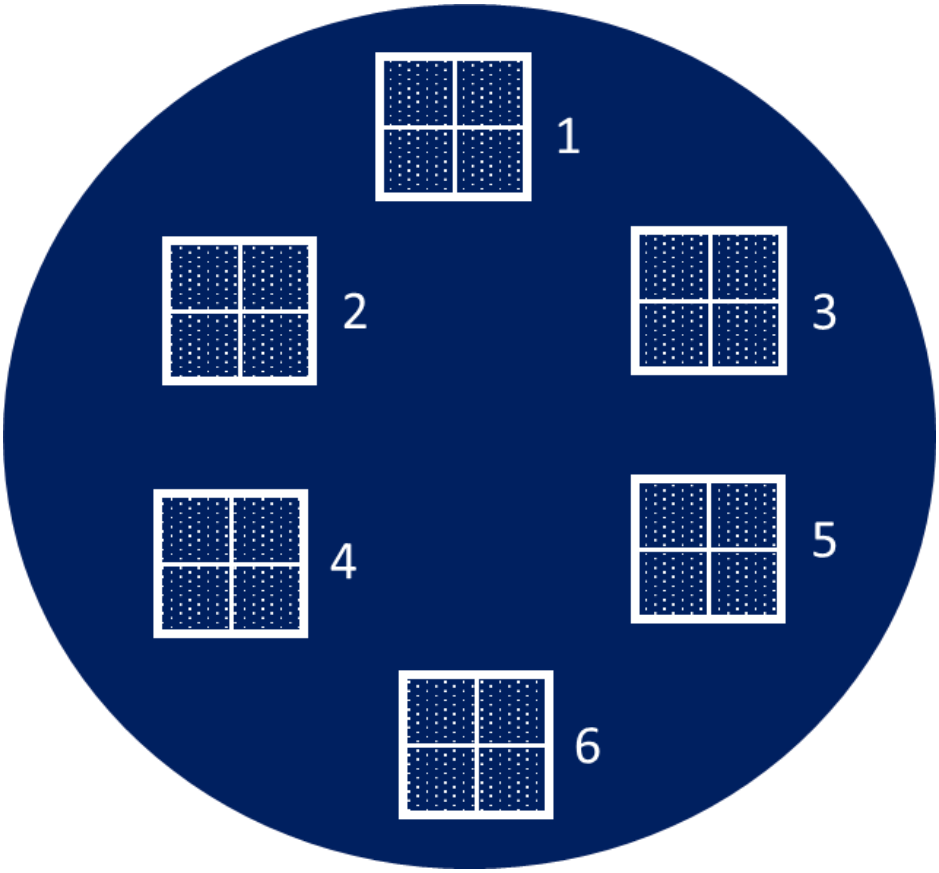

Figure 2.4 Microwell master diagram. The blue represents the silicon wafer, and the white represents the cross-linked photoresist deposited on the wafer. Each wafer has a diameter of 76.2 mm.

This final microwell device design featured PDMS wells with a 15 μm diameter and 24 μm depth, each spaced 450 μm apart and arranged in a 400-well array. The array was surrounded by a box and divided into four quadrants, with each quadrant containing 100 wells. The addition of the box makes it possible to see the edges of each device with the naked eye, improving the process of cutting microwells out of PDMS. The center of the array has a set of scale bars marking each millimeter, making microwells easier to locate under a microscope, accelerating data collection. Each device on the master was labeled with a number 1-6 to keep track of which devices were fabricated successfully and have not yet been worn down. The addition of the numbers assists in preparing all microwells

in the same orientation since the orientation of the numbers is visible with the naked eye, unlike other features on the microwell master. This final design is depicted in Figure 2.2.

2.4 Troubleshooting Microwell Device Fabrication

Microfluidic device protocols produced by our lab were the starting point for fabrication of microwell devices. A schematic depicting this process is given in Figure 2.5. The general process begins with production of a microwell master from a template with the desired design, PDMS is then poured over the design to generate devices based on the master mold, and finally the devices can be cut out of the PDMS and used for measurements. This section discusses necessary modifications to the fabrication protocol, and a detailed protocol for the entire process is included in Appendix B.

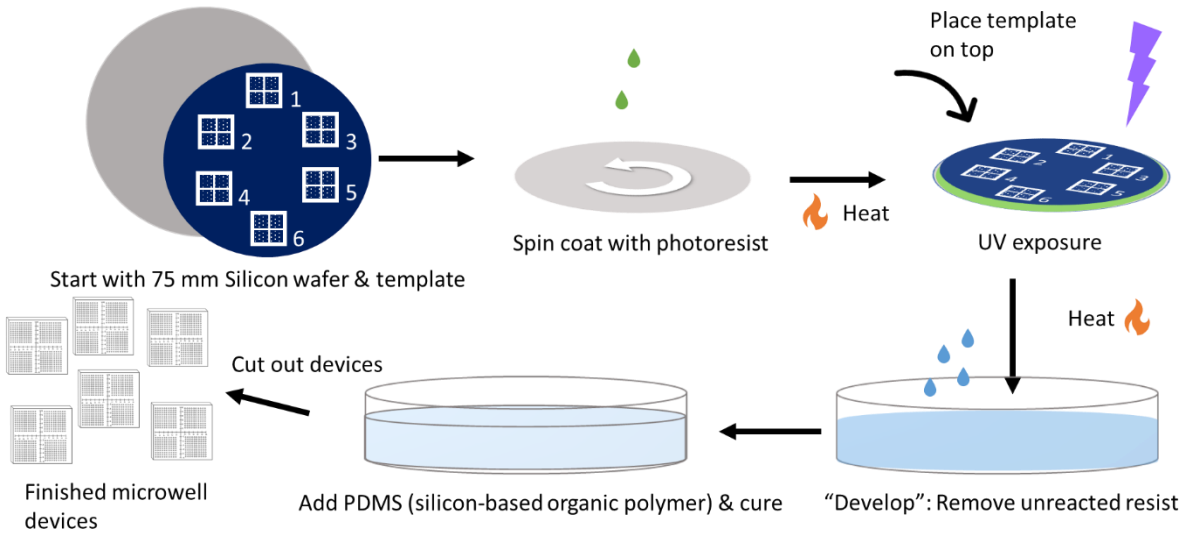

Figure 2.5. Fabrication process schematic. Process starts with 75mm silicon wafer and photolithography mask designed in AutoCAD. Output of this process is a microwell master that is used as mold to make microfluidic devices, with 6 PDMS microwell devices produced from the master each time.

Although a protocol for this process was successfully used for fabrication of other designs, the same protocol had to be extensively modified for fabrication of microwell devices. Fabrication of the master for the final design of 15 μm diameter wells with wide spacing between wells required adjustment of UV exposure doses, thoughtful modification of heating steps, and careful application of development steps to successfully produce microwell masters. While in theory the production of masters only takes a few days, to successfully test a range of settings and modify the procedure for different rounds of design took several months. The result of this process is an updated protocol that can be applied for improved adhesion for rapid fabrication of new designs with minimal adjustment. The entire fabrication process is summarized in a flow chart in Figure 2.6.

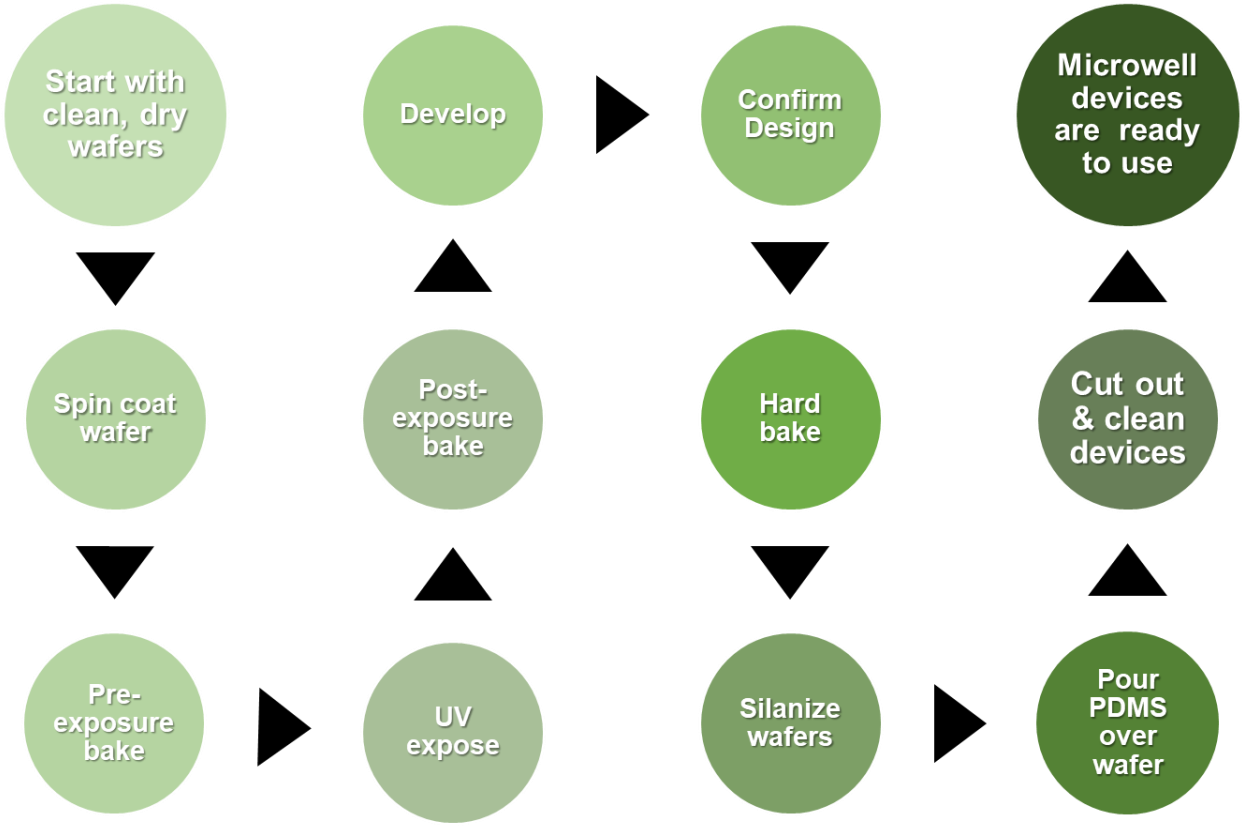

Figure 2.6. Flow diagram of microwell device fabrication process. Process starts with clean, dry silicon wafers and produces a microwell master mold that can be reused, ending with the production of six PDMS microwell devices.

The first step in the process to make the microwell master is to design a template in computer-aided design (CAD) software such as AutoCAD. This template was made according to the specifications in the section 2.3 for each round of microwell template redesign. The AutoCAD design is then printed on a photolithography mask for later use in the UV exposure steps.

Silicon wafers with 76.2 mm diameter are used as a substrate for the microwell masters. The wafers are thoroughly cleaned by rinsing for 5 minutes in acetone, 2 minutes in methanol, and are then rinsed with isopropanol (>90%), dried with N_2 gas, and solvents are evaporated away by placing the wafer on a hot plate at 70 °C for 10 minutes. Starting

with clean wafers is essential for proper adhesion between the photoresist and the wafer in later steps. The wafers are spin-coated with SU-8, a negative photoresist and then soft baked on a hot plate to evaporate excess solvent. The photolithography mask is used to expose UV light only to the area designated by the template, producing the acid catalyst. The acid catalyst promotes the polymerization reaction when the mask is removed and the wafer is heated during the post-exposure bake, with the design appearing on the wafer after a few minutes of heating. Uncrosslinked photoresist is then washed away with SU-8 developer, Propylene glycol methyl ether acetate (PGMEA) and the wafer is hard baked overnight at 150 °C to smooth out any cracks in the photoresist. The wafers are then silanized with (tridecafluoro-1,1,2,2-tetrahydrooctyl)-1-trichlorosilane to passivate the surface so that PDMS can be peeled off the master easily.

This wafer with the design is then referred to as the microwell master and is the mold from which PDMS devices can be made. PDMS is prepared by mixing the pre-polymer and curing agent in a 10:1 ratio. PDMS is poured over the microwell master and is cured overnight in an oven at 70 °C. The microfluidic devices are cut from the PDMS and the master can be used many times to produce more devices.

While the microwell masters containing closely packed microwells were straightforward to fabricate, the new microwell masters were considerably more difficult due to their small size, shallow depth, and sparse arrangement. Several rounds of fabrication were needed to optimize each step of the fabrication procedure. For the first several rounds of fabrication SU-8 2025 was used as the photoresist. Of the photoresists our group possessed, this one was desirable because it could be used to spin coat photoresist in thicknesses between 20-80 μm. This coating thickness corresponds to the

depth of the microwells once the photoresist is crosslinked and developed. The spin speed was set to 4000 rpm to produce well depths of approximately 20 μm. Once the initial supply of SU-8 2025 ran out I replaced it with SU-8 3025 for improved photoresist adhesion. The same spin speed settings were used for the new reagent to produce similar microwell depths based on the product datasheets. [107,108]

For the device design with 450 μm microwell spacing (prior to the introduction of boxes and scale bars), the amount of energy needed for UV exposure was considerably lower than the guidelines on the SU-8 datasheet. To achieve the recommended 150-160 mJ/cm^2 recommended for photoresist with 25-40 micron thickness, 15-17 s of UV light exposure would be needed based on the 9.5 mW/cm^2 measured power of the UV contact aligner.[107] After trying a range of settings, starting with 17 seconds of exposure and gradually lowering UV exposure settings it was determined that 8-9 s of UV exposure produced 15 μm diameter microwells that successfully formed and remained on the substrate following development. Due to the small area of the features, other diameters of microwells required adjustment of the exposure settings for successful fabrication. The introduction of the boxes and scale bars around the design greatly increased the area of exposed photoresist and required adjustment of the exposure settings. For the final microwell device design, UV exposure was increased to 20-22 seconds for each master.

These exposure doses were determined by evaluating microwell formation at several stages of master fabrication. Following the post-exposure bake, microwell masters were removed from the hot plate and viewed under a microscope. If the photoresist shows cracks on the outside of the design area, that indicates that the cross-linking reactions have spread beyond the area of the design. When this happens, the

wafer has been overexposed and the exposure time should be reduced in future trials. Similarly, if the photoresist shows cracks on the inside of the design template, that indicates the plate has been underexposed and the exposure time should be increased.[109] If there is poor contact between the photolithography mask and the photoresist during UV exposure, a similar effect to overexposure will be observed as there is less control over the exposed area. Contact between the mask and the photoresist is improved by adding a few drops of glycerol between them. The glycerol will be rinsed off later during the development step.

Another issue with master fabrication that made production difficult was poor adhesion between the photoresist and the wafer. Poor adhesion results in microwells that wash away during the development step. The most important parameters in the fabrication process that affect adhesion are exposure time, followed by post-exposure bake settings, and finally with development technique playing the third most important role.[110] A UV exposure time that is too short results in weak adhesion between cross-linked photoresist and the wafer substrate, increasing the likelihood that wells will wash away. Exposure doses were evaluated based on the above discussion. If the microwells appear overexposed following the post-exposure bake but still wash away, the other key fabrication steps in the process must be evaluated and optimized to improve adhesion.

Since the post-exposure bake is the second most important step for strong adhesion, it was improved next by starting all heating steps at room temperature and heating at a rate of 6 °C/min. Once the hot plate is warmed to within 10 °C of the desired temperature, the timer for the heating step is started, and the plate is cooled at the same rate. Once the hot plate is 20 °C below the temperature setting the wafer is removed from

the heat. This modification results in a gentler heating process. By modifying all heating steps and not just the post-exposure bake, crosslinking will begin at lower temperatures and each step will be less abrasive.[111]

The final fabrication parameter to be optimized was the development technique. Submerging the wafer in developer induces stress to the photoresist, so care must be taken to reduce stress during this step.[111] To achieve gentler development, the wafer is completely cooled prior to submerging in developer, and for the first half of the development time the solution is left unperturbed. For the second half of the development time, the solution is gently agitated around the wafer. This produced better results compared with the more vigorous rinse that was used before, resulting in a greater percentage of microwells stuck to the wafer. Whereas before instituting these modifications all the microwells washed away in the development step, greater than 90% of microwells remained adhered to the substrate following development once these changes were made.

The lab protocol for silanization with (tridecafluoro-1,1,2,2,-tetrahydrooctyl)-1-trichlorosilane called for a few drops of the solution to be placed in a vacuum chamber with the microwell master for 3 hours. This method resulted in PDMS adhered to the microwell master that could not be removed without also destroying the photoresist on the master surface. The protocol was adjusted for the silanization to occur overnight, guaranteeing that the wafer surface has been sufficiently passivated before removing it from the chamber. This alteration yields microwell masters from which PDMS can easily be peeled off.

Protocols for PDMS device cleaning and storage also needed to be adjusted. Once fabricated, the microwell devices must be kept free of dust so they are ready to be filled with solution. After cutting out devices in a cleanroom for low dust levels, each side of the PDMS device would be covered in tape. The tape was left over the wells to prevent dust from entering them prior to use. After a few trials it was found that the tape residue blocked the wells. To prevent this issue, tape is removed immediately after cutting out microwells and is only used to remove PDMS debris immediately after cutting out the devices. N_2 gas is used to blow away dust particles, and the cut devices are rinsed with isopropanol for 10 s. The devices are dried with N_2, and any remaining solvents are evaporated away by placing the device on a hot plate set to 70°C for 10 minutes.

For device storage, one technique initially used was plasma cleaning the devices and storing them pressed against a clean coverslip to keep dust out. This technique was discontinued after a few batches of microwell devices became stuck to the glass and were unusable. Instead, the clean devices are stored in a clean petri dish that is taped closed and wrapped in aluminum foil. The container is stored in a dust free hood and is only opened in a clean environment. Microwell devices are only removed immediate before use to be filled

These adjustments made to the entire fabrication process from microwell master fabrication through storage of the PDMS devices were necessary to generate a detailed microwell device generation protocol described in Appendix B. The result was applied for rapid and successful re-fabrication of the microwell master when it became worn out after repetitive use. PDMS microwell devices fabricated according to this procedure can be stored for several weeks and filled with solution without issue.

2.5 Microwell Filling Investigation

After optimizing the microwells design and fabrication, the next step is to evaluate their use in fluorescence experiments using the proteins of interest. After several rounds of measurement of smURFP, I noticed considerable variation in maximum fluorescence signal. Further examination revealed 5-fold variation between the lowest and highest signal collected from an individual microwell. Evaluation of the height of individual microwells, the filling procedure, and whether microwells remain filled over time was needed to determine the source of this variation. For accurate data interpretation it is essential that variations in signal are due to smURFP fluorescence and not artifacts introduced by the data collection method.

The first concern after observing variation in signal levels was whether each microwell contained the same volume of solution. To address this, the microwell depth distribution for each microwell device on the master was determined using an optical profilometer. The optical profilometer measures the height difference between the photoresist and the wafer in several locations to confirm the photoresist thickness. The instrument used for these measurements is a white light vertical scanning interferometer. Using this instrument to evaluate the microwell devices is ideal because it is a non-contact method so repeated measurement will not damage the microwell masters. The instrument works by exploiting the low coherence of white light, vertically scanning to vary the optical path difference, generating an interference function that is used to determine the height difference between two locations. The height difference was measured in 30 places for each device to produce a histogram displaying the variation in well depth for each device. This histogram can then be compared to another histogram that reports initial

fluorescence signal for fluorescence measurements made using the same device (Figure 2.7). The histogram of initial fluorescence signal showed considerably more variation compared to the microwell depth distribution, indicating that the initial signal variation could not be caused by variation in well depth, and must have another cause.

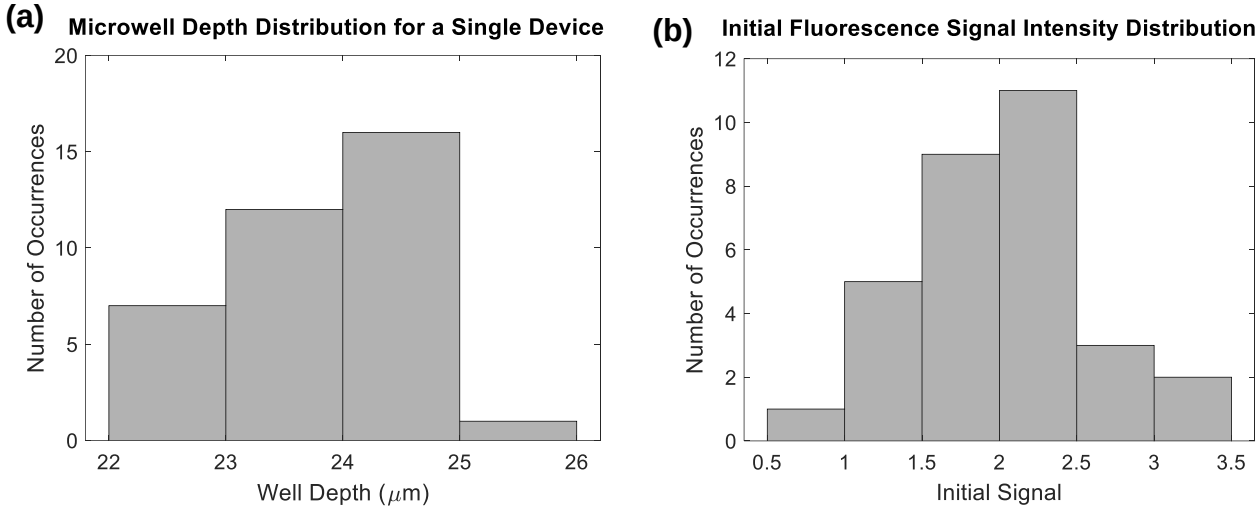

Figure 2.7 Comparison of microwell depth distribution to fluorescence signal. (a) Distribution of microwell depth for a single device measured with an optical profilometer. 50x magnification was used for optical profilometer measurements. Microwells with depths above 25 µm were excluded from measurements. (b) Distribution of smURFP fluorescence initial signal from microwells filled with 30 µM smURFP. Unfilled microwells were excluded (signal with less than a 2-fold increase compared to the blank).

Once well depth variation was ruled out as a cause for variation in initial fluorescence signal, the next parameter to be evaluated was microwell filling levels across the device. This assessment was needed to confirm that microwells contain the same volume of solution across the device. A series of experiments were performed to determine the maximum volume of purified protein that could be used and to determine the proper technique for filling them. Ideally the microwells would be filled with enough solution for a 10-fold signal above the blank and no signal between wells. This ensures that all the solution has been pressed into the microwells and expelled from the space between wells.

Pressing the device on top of the coverslip with solution was not sufficient to force solution into microwells and out of the space between wells, since this technique resulted in high signal between wells. The procedure was adjusted by placing a magnet on top of the device after pressing it on top of a coverslip with a drop of fluorescent protein solution, wicking away any solution that leaks out of the edges of the device with a piece of filter paper. This technique resulted in signal between microwells comparable to the signal produced from blank media between two coverslips. The filling volume was optimized using this procedure. To determine the optimal volume of fluorescent protein solution to add to the coverslip, a range of volumes from 1 µL to 20 µL were used for testing. 15 µL was selected as the optimal volume since it is the highest volume that can be used without increasing signal between microwells, and so maximizes microwell filling and therefore fluorescence signal that can be produced from a given protein concentration. Higher volumes of fluorescent protein solution will result in higher signal between wells, indicating not all solution is removed from between the microwells. Fluorescence signal 10-fold higher than the blank was successfully produced with 15 µL of 10 µM smURFP solution.

After the microwell filling procedure was optimized, the next step to consider is how long the microwells can be used for experiments after they are initially filled. An overnight time lapse experiment was performed to determine how long and to what extent microwells stay filled once protein is added. In this experiment, a microwell device was filled and imaged under brightfield illumination at 40x magnification in three locations every 10 minutes to determine microwell filling levels for over 8 hours after being filled with fluorescent protein. The absorbance was averaged across these three microwells and the results were normalized to yield a plot of absorbance over time (Figure 2.8). One

hour after the initial measurement the absorbance was 89 % of the initial value. After two hours, the absorbance was 77 % of the initial value. After 8 hours, the absorbance was 66 % of the initial value. From this result it was determined that microwell devices should be used as soon as possible after filling and microwell experiments should be concluded within 1-2 hours of filling. For longer experiments, the microwell devices could be sealed to the coverslip by applying a layer of clear nail polish between the PDMS and the coverslip.

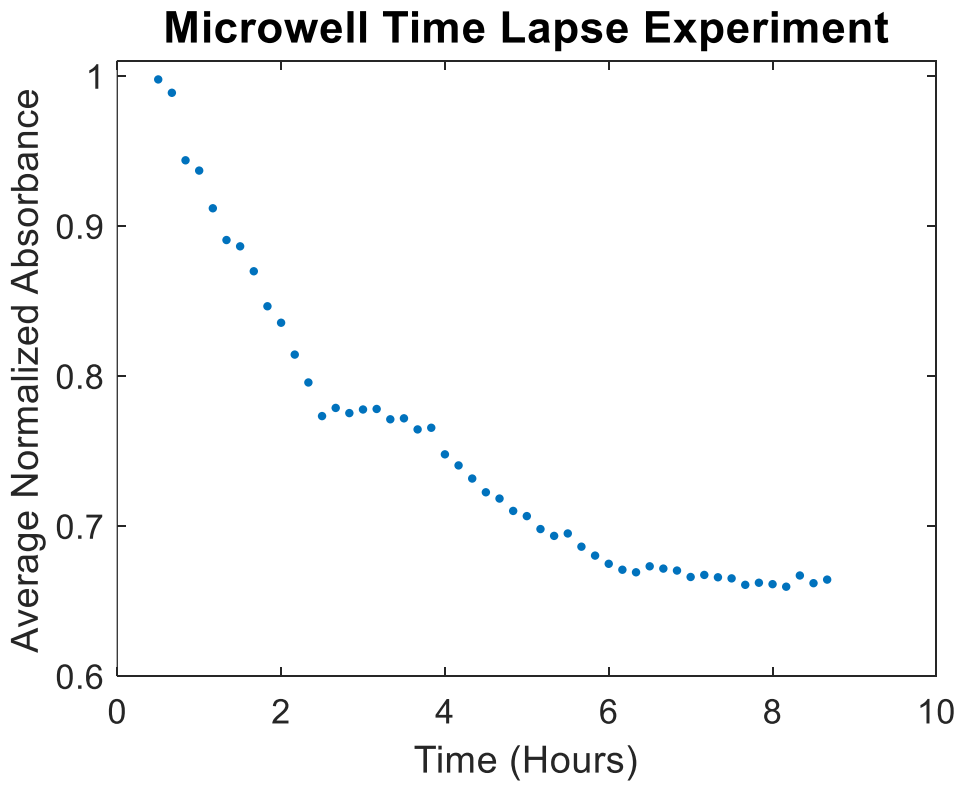

Figure 2.8 Results of microwell time lapse experiment. This data is the result of imaging three smURFP-filled microwells filled under brightfield illumination. The wells were imaged every 10 minutes over 8 hours and the results were averaged. Results show a 66% reduction in signal intensity at the end of the measurement.

2.6 Pre-illumination Study

After assessing microwell device well-depth variation, filling procedure, and filling levels over time, there was still considerable variation in initial fluorescence signal. Pre-illumination of microwells prior to imaging was the final source of variation investigated. Light scattered through the PDMS reaching the nearest neighboring microwell would cause a portion of molecules within samples to be bleached or converted to the dark state. The extent of the pre-illumination phenomenon was evaluated by preparing samples of bulk protein solution and imaging repetitively. Bulk solution was used rather than microwells for these measurements to quickly assess this occurrence without requiring additional microwell device fabrication. 10 measurements were made on each sample, moving the microscope stage in the x-direction 500 μm after each measurement to mimic microwell spacing. Three samples were prepared at each irradiance and the fluorescence decay profile for the three measurements were averaged to produce plots of average signal reduction following subsequent measurement. These measurements were compiled to show how initial fluorescence decreases as number of measurements increases. (Figure 2.9)

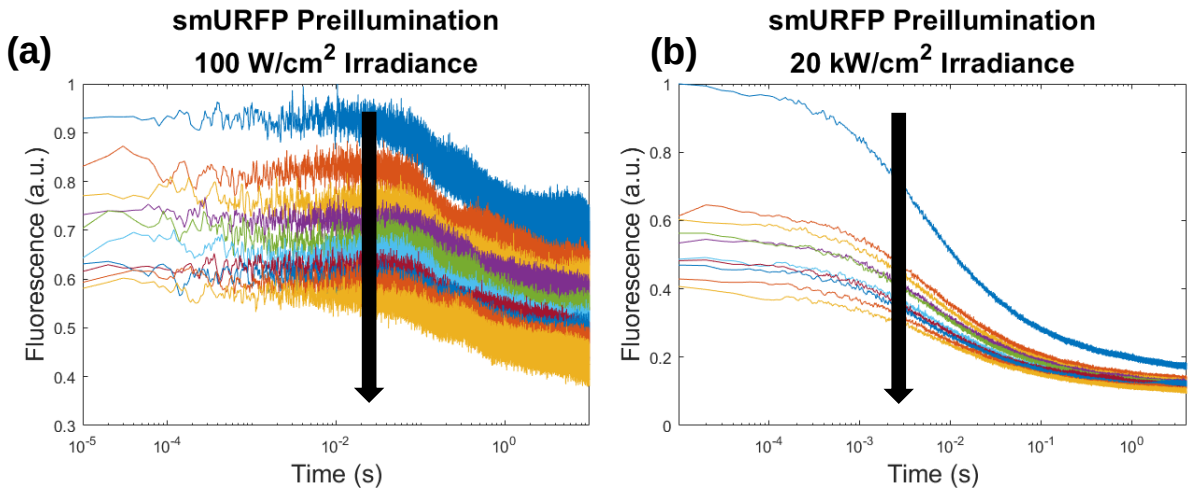

Figure 2.9 Results of pre-illumination study (a) 100 W/cm^2 irradiance. (b) 20 kW/cm^2 irradiance. Arrows show the direction of increasing number of measurements within one sample. The arrows show that for both irradiances, fluorescence signal decreases with increasing number of measurements.

The compiled fluorescence plots measured at irradiances of 100 W/cm^2 and 20 kW/cm^2 show a reduction in signal over the 10 measurements. At lower irradiances, the reduction in signal was less pronounced. To quantify the pre-illumination effects, I calculated the irradiance 450 µm away from the center of the beam, revealing that at an irradiance of 20 kW/cm^2 within the FWHM, the nearest neighboring well experiences an irradiance of 200 W/cm^2. This irradiance experienced by the nearest neighboring microwell is nonnegligible and must be taken into consideration when analyzing results. The pre-illumination effect may have been artificially enhanced in these measurements compared to in actual microwells by using bulk solution to study this effect instead of microwells. Some of the observed pre-illumination can be attributed to diffusion of bleached molecules into the measurement area. The large drop off in signal between the first and second measurement at high irradiances suggests that future designs should

space microwells even further apart to minimize pre-illumination and low irradiances should be used to minimize the effect.

2.7 Conclusion and Future Outlook

The creation of microwells posed several challenges, both in design and fabrication. Several iterations of design were needed to generate microwells that were appropriate for the collection settings. Initial rounds of master fabrication resulted in microwell devices where all or most of the wells washed away or the wells were severely warped from overexposure of the photoresist. Fabrication of microwell masters was improved by using a slow ramp up of temperature for all heating steps, using gentle agitation during the development step, and by adjusting the UV exposure time based on the photoresist thickness and design template. After several rounds of modification to the fabrication procedure, microwells were successfully fabricated with most wells remaining adhered to the wafer.

Once the microwell devices were successfully fabricated, they had to be evaluated for use in fluorescence experiments. Assessing the microwell depth with an optical profilometer showed minimal variation across devices. Microwell filling was optimized for filled microwells with signal between wells comparable to the blank and high signal within wells. It was determined that microwells can reasonably be imaged for up to 2 hours after initial filling and could be imaged even longer by sealing the PDMS device to the coverslip. The pre-illumination study determined the source of variation in initial fluorescence signal intensity, and yielded recommendations for future improvement to the microwell device

design by increasing spacing between adjacent wells. The results of the pre-illumination study also suggest that use of lower irradiances in future studies would minimize artifacts due to pre-illumination.

Overall, microwells are a considerable improvement compared to droplets. Repetitive measurements are faster since the box and scale bar on each device makes it easier to locate microwells. The arrangement in a 400-well array provided a huge increase in number of measurements that could be made in one sample compared to droplets. Every microwell is the same size, eliminating the need to evaluate the size of a droplet before each measurement. Microwells are evenly spaced and far apart, reducing fluorescence contribution from nearby wells and keeping the minimal fluorescence contribution from nearby microwells constant throughout the experiments. The spread out spacing of microwells on the device also reduces pre-illumination effects compared to droplets. For these reasons, fluorescence measurements in later chapters use microwells alone for fluorescence measurements.

Chapter 3: Data Collection and Analysis Methods

3.1 Introduction

This section details the experimental methods used to measure the fluorescence decay profiles of fluorescent proteins as well as the analysis methods used to extract the rate constants for dark state conversion, ground state recovery, and photobleaching from the data. The first three sections discuss the experimental methods, with how samples were prepared for optical measurements described in Section 3.2, followed by the experimental setup in Section 3.3, and lastly a description of the procedure for collecting measurements in Section 3.4. The final three sections describe the processes used for data analysis, with Section 3.5 describing in detail the calculation of irradiance, followed by a thorough discussion of data analysis of continuous illumination data in Section 3.6.

3.2 Sample Preparation

This section describes how protein samples are prepared for fluorescence measurements. Samples for measurements done in microwells or droplets are prepared using purified fluorescent protein in Tris buffer (150 mM NaCl, 50mM Tris-HCl, pH 7.4) to fill them with protein concentrations in the range of 5-10 μM. Protein is thawed immediately before use and samples are stored at 4 °C for no more than one week. Small

aliquots are used so that samples are used within 24 hours after thawing. Protein concentration is determined by measuring the absorbance of the protein solution using a cuvette with a UV-Vis spectrometer or using a NanoDrop to measure the absorbance of small volumes of solution (1-2 µL). The stability of smURFP and miRFP670 was assessed by comparing the UV-Vis absorption spectrum of a sample that was frozen and later thawed to that of a sample of freshly purified sample. The spectra of both proteins was identical.

Microwells were filled by adding 15 µL of purified protein to a 22 x 22 mm coverslip and pressing a clean microwell device on top. A magnet is then placed on the device to press the solution into the microwells and press the solution out of the space between microwells. Filter paper is used to wick solution away from the edges of the device. The device with the coverslip is flipped over to ensure all excess solution is removed. Prior to use, dust is removed from the coverslips and PDMS devices with an air gun.

For test measurements, droplets are prepared by mixing a 1:9 ratio of protein solution with 1-octanol. The solution is vortexed for 30 s and is pipetted 5 times to mix immediately before use. Mixing immediately before use increases the likelihood of producing a good number of smaller droplets (~15 µm) that are ideal for measurements with the beam size in the setup. 5 µL of droplet solution is added to a corner of a clean 22 x 22 mm coverslip before placing another coverslip on top. Uniformity of droplets can be improved by sonicating the droplet solution or by applying a hydrophobic coating to the glass slides.[112]

For experiments done in live cells, the sample was prepared by expressing the fluorescent protein in *E.* coli cell on an agar plate (See protocols in Appendix B). Since *E.*

coli cells produce heme but do not produce biliverdin, the proteins were co-expressed with heme oxygenase (HO-1) to generate biliverdin, as is necessary to produce fluorescence. After at least 24 hours of growth at 37 °C, the plate was stored at 16 °C for at least 24 hours prior to measurement. Immediately prior to measurement, a single colony is selected and removed from the agar plate using an inoculum loop. The colony is dissolved in 250 µL of blank media. The colony is vortexed for 30 s and pipetted 10 times to mix. 20 µL of solution is placed on a clean 22 x 22 coverslip and a second coverslip is placed on top. This technique resulted in bright fluorescence for *E coli* measurements with cells suitable to easily be selected with a 40x objective (Olympus). An agar plate was used to prepare *E. coli* cells instead of liquid culture because liquid culture resulted in much smaller *E. coli* cells that did not produce fluorescence signal at least 5-times signal produced from the blank, the standard used to select measurements.

3.3 Experimental Setup

This section describes the features of the optical setup and why the selected optics and settings were chosen. For fluorescence measurements of near-infrared fluorescent proteins, a 637 nm diode laser (Coherent, OBIS 637LX) is used as the excitation source. A 650 nm dichroic mirror (Brightline, FF650-Di01) is used to reflect the excitation light into a custom-built inverted microscope. Laser light is focused onto the sample by a 20x 0.75 NA air-immersion objective (Olympus). A 50:50 beam splitter is used to direct 50% of the scattered light from the sample to be focused onto a CMOS camera (ThorLabs, DCC1545M) for sample visualization, with the other 50% of the scattered light focused

onto the Photo-Multiplier Tube (PMT, Hammamatsu Photonics, R9880U-20). The combination of the dichroic mirror mentioned above and a pair of identical 731 nm emission filters (Brightline, FF01-731/137) prevent stray excitation light from passing to the PMT. Photocurrent from the PMT was converted to voltage using a custom-built AC-coupled linear transimpedance operational amplifier to improve the signal-to-noise ratio by removing high and low frequency noise components. Noise components outside the bandpass of 160 mHz to 106 kHz bandpass were removed. The resulting voltage levels were digitized at a sampling frequency of 100 kHz with a PC-based data acquisition board (DAQ, National Instruments) and LabVIEW software (http://ni.com/labview, National Instruments, 2012 version).

Data collection was operated with custom-built LabVIEW software which controlled power setting, sampling frequency, and modulation of the 637 nm laser. The laser is operated in digital modulation mode and interfaces with the computer using the DAQ board. The irradiance of the laser is tuned by changing the laser power setting of the 637 nm laser and by attenuating the beam using the half-waveplate and polarizer in the setup. Figure 3.1 shows the diagram of the experimental setup as well as labeled photos of the experimental setup.

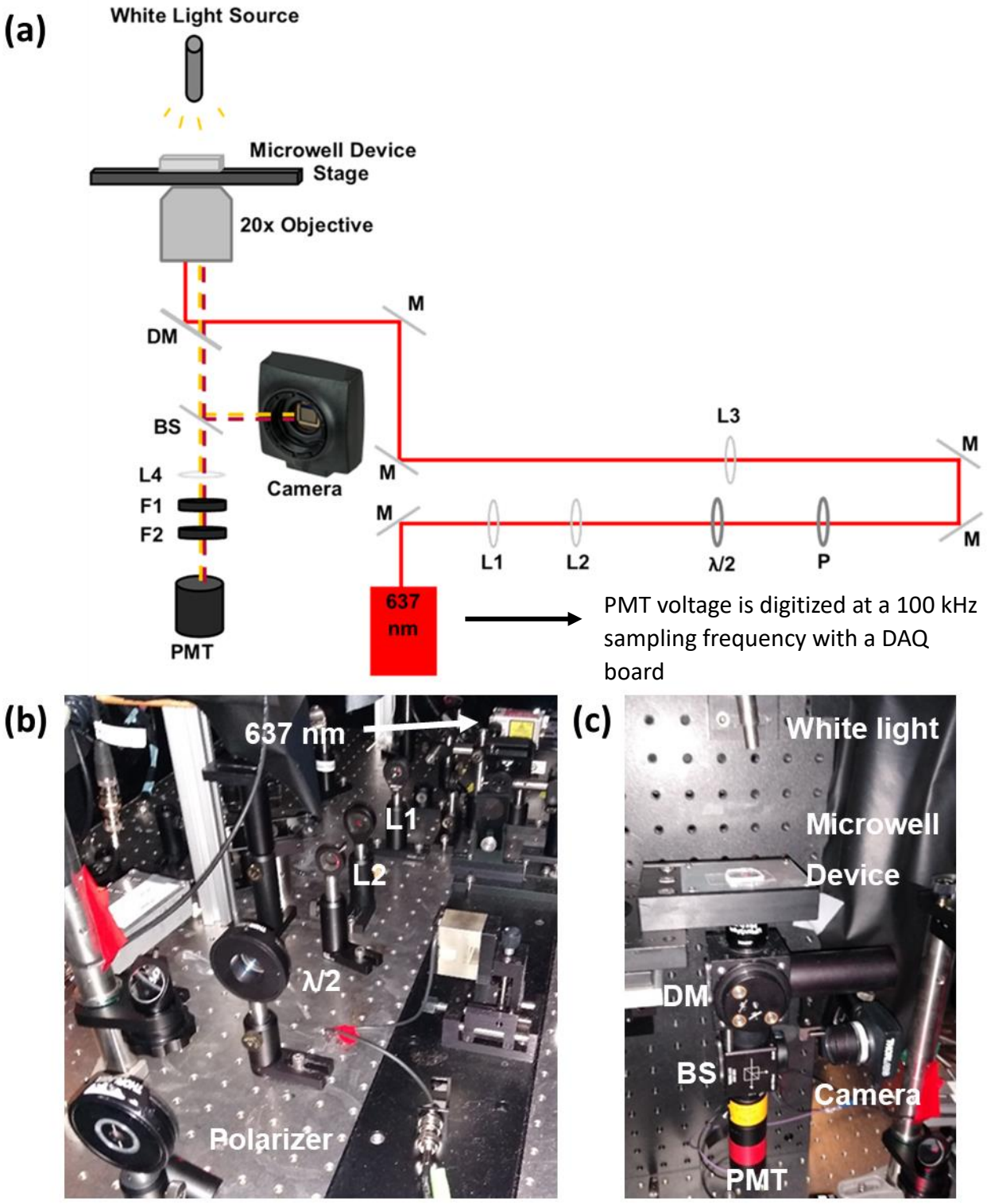

Figure 3.1 Optical setup. (a) Optical diagram of fluorescence microscope. Each M is a silver coated mirror. L1 and L2 are lenses λ/2 is a half-waveplate. P is a calcite polarizer. L3 is a lens focusing light into the microscope. DM is the 650 nm dichroic mirror and BS is a 50:50 beamsplitter. L4 is a lens focusing scattered light onto the PMT. F1 and F2 are the emission filters. (b) Image of beam path. (c) Image of microscope stage

Due to the smaller size of *E. coli* cells (~2 µm long) compared to droplets and microwells, the setup was modified for measurements with *E. coli* cells by replacing the 20x objective with a 40x 0.60 NA air-immersion objective (Olympus). For experiments done with red fluorescent proteins, the experiment was modified due to the different excitation and emission properties of these fluorescent proteins compared to near-infrared fluorescent proteins. The excitation source is replaced with a 561 nm diode laser (Coherent Genesis MX), The filters (F1 and F2) are replaced with a set of red emission nm filters and the 650 nm dichroic mirror is replaced with a 573 nm dichroic mirror (Brightline, FF573-Di01). The 561 nm laser pulse profile was obtained with an acousto-optic modulator (AOM, Gooch & Housego, 35210-BR). The RF input to the AOM driver was delivered by a function generator (Agilent 332050A) controlled by custom MATLAB (http://www.mathworks.com, The Mathworks, Inc., version 2019a) software. For mCherry, an acquisition rate of 1 MHz is used. All other aspects of the experimental setup remained the same when switching between fluorescent protein type.

3.4 Optical Measurements of Dark State Photophysics

The same procedure for setting up and running fluorescence measurements was followed to ensure measurement reproducibility, as described in this section. The first step of performing these measurements is checking the alignment with the laser power set to 1 mW. The microwells are co-focused with the beam to ensure that the best microwell focus is also the best focus of the beam. A clean coverslip is placed on the

sample stage to aid in the alignment check. Mirrors are adjusted so that the reflections from both sides of the coverslip are directly overlapped.

Once the alignment check is complete, the sample is prepared as described in Section 3.2 and is placed on the sample stage as shown in Figure 3.1c. In the case of the microwells, the sample is oriented with the coverslip facing down and toward the objective. The cell, droplet, or microwell to be measured is centered within the beam area drawn on the computer screen using the CMOS camera and white light illumination. Samples are centered within the FWHM to ensure uniform irradiance across the measurement since the irradiance within this area can be assumed constant. Each measurement location is selected within a sample by moving the microscope stage in the x- and y-direction until the cell, droplet, or microwell is centered within the FWHM as labeled on the computer screen. For the near-infrared fluorescent protein measurements, data is acquired using LabVIEW program smURFP_v06.vi to control data collection settings. The sample collection rate is set to 100 kHz. The PMT voltage is set to 500V, within the linear range of the PMT. Fluorescent protein sample concentrations were selected to avoid saturation of the PMT. When necessary for high irradiance measurements, a neutral density filter was added immediately before the PMT to prevent saturation.

To gain insight into the light-dependence of the dark state conversion and ground state recovery processes, experiments were performed under both continuous and pulsed illumination conditions. For the continuous illumination measurements, the laser is set to turn on for 90 s and turn off for 5 s. These settings were selected to ensure that the fluorescence for each trial was collected over one pulse. The 90 seconds setting was

the longest possible for the 100 kHz frequency and the LabVIEW memory settings, any longer and the memory is overloaded. Collecting measurements at longer times would require a reduction in sampling frequency.

3.5 Calculation of Irradiance

At the beginning of each set of fluorescence measurements, the irradiance must be characterized to accurately determine how much light is illuminating the sample. This section will discuss the steps taken to carefully measure and calculate the irradiances for each measurement. The beam spot size is measured at the focus by setting the power to 100 mW. The image of the beam is collected on the camera with the exposure set to the lowest setting. Previous characterization of the laser beam determined that the beam area is constant above a power setting of 20 mW and the beam area decreases by 22% below that power. If the camera is saturated at 100 mW, a power of 50 mW is used for that waveplate and polarizer setting. This produces a beam size for the laser at the focus which fluorescence is generated, since for each sample type (cells, droplets, microwells), the sample is imaged through a coverslip. Within the camera program a circle is placed around the center of the beam. Samples are then centered within this area to ensure uniform irradiance across the measurement.

To calculate the laser spot size, ImageJ (http://imagej.net/, ImageJ, version 1.52p) is used to extract the beam line profile in the horizontal and vertical directions. The extracted line profiles are then loaded into OriginPro (https://origin.com, OriginLab, version 2019b) and fitted to a Gaussian to calculate the FWHM of the beam. This FWHM

is measured in pixels and is converted to centimeters by using a unit conversion determined from measuring a calibration standard within the setup. The calibration standard is a set of 5 µm squares with a 5 µm pitch and is used to calculate the number of µm per pixel. The process of measuring the profile and fitting the line profile was repeated three times to determine error associated with the process. The variability of the FWHM using this technique was determined to be less than 0.01%.

Using the FWHM from both the vertical and horizontal line profiles, the area of the spot size is calculated by using the equation for the area of an ellipse (Equation 3.1).

$$Area = \pi \cdot \frac{H}{2} \cdot \frac{V}{2}$$

Equation 3.1 Area of an ellipse. H is the horizontal FWHM (cm) and V is the vertical FWHM (cm).

The error on the calculation for area is given in Equation 3.2.

$$Error = \sqrt{\left(\frac{\partial(Area)}{\partial H}\right)^2 \cdot {s_H}^2 + \left(\frac{\partial(Area)}{\partial V}\right)^2 \cdot {s_V}^2}$$

Equation 3.2 Equation for error on the spot size calculation. s_H is the standard deviation of H and s_V is the standard deviation of V. All variables have units of centimeters.

Another aspect that must be considered to find the beam irradiance is the laser power at the sample. The fraction of laser power that reaches the sample is measured with a power meter immediately above the objective. For powers below 30 mW at the sample, a silicon sensor (Coherent, OP-2 VIS) is used to measure the power. For powers above 30 mW, a position-sensing air-cooled thermopile sensor is used (Coherent, LM10).

It was concluded from measurements on the 637 nm laser at a range of power settings that the fraction of light that reaches the sample is constant at multiple laser powers, so this measurement can be used for all power settings. The power is carefully measured to ensure the detector is accurately placed and the maximum power reading is recorded. The measurement is repeated three times and the average value is used to calculate the irradiance. Power measurements were made at the beginning and end of experiments and reported a 0.1% change in power from the beginning of measurements to the end.

Using the information on spot size and fraction of power that reaches the sample, the irradiance can be calculated using Equation 3.3 for each power used for experiments.

$$I = \frac{(Power\ ) \cdot (F)}{Area}$$

Equation 3.3. Equation for Irradiance, I. Power is the laser power setting in Watts. F is the fraction of the laser power that reaches the sample.

The error of the irradiance calculated is found using Equation 3.4.

$$Error = \sqrt{\left(\frac{\partial I}{\partial F}\right)^2 \cdot {s_F}^2 + \left(\frac{\partial I}{\partial Area}\right)^2 \cdot {s_{Area}}^2}$$

Equation 3.4. Error calculations for Irradiance. s_F is the standard deviation of F and s_{Area} is the standard deviation of the spot size.

An example of a typical irradiance calculation from measurements made on 12/04/2018 found the fraction of laser light that reached the sample was 0.806 ± 0.002, with a horizontal beam diameter of 21.217 ± 0.002 μm and a vertical beam diameter of

23.750 ± 0.002 μm. This resulted in an area of (3.96 ± 0.01) x 10^{-6} cm^2 and an irradiance of 2.037 ± 0.009 kW/cm^2 when the power was set to 10 mW and 14.26 ± 0.06 kW/cm^2 when the power was set to 70 mW.

Section 3.6 Analysis of Continuous Illumination Data

Analysis of continuous illumination fluorescence data for fluorescent proteins to find the rate constants for photophysical properties required careful development of a data analysis scheme. The data for near-infrared fluorescent proteins had more variability compared to similar measurements of red fluorescent proteins so a rigorous procedure was developed to ensure that no biases were introduced in steps taken to remove outliers. All data received the same treatments in the processing steps. This section discusses the procedure used for data processing, fitting, and reduction. An overview of the data analysis scheme is depicted in Figure 3.2.

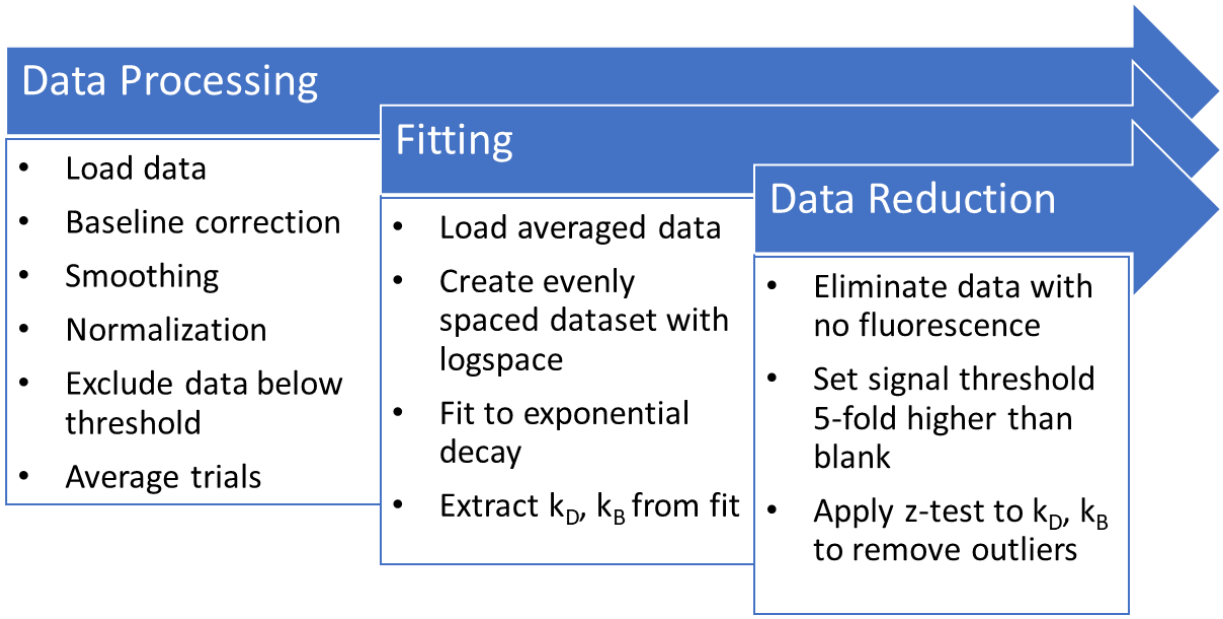

Figure 3.2 Flow chart summary of data analysis scheme. Scheme starts with data processing in MATLAB, followed by fitting using a sum of exponentials, and reduction through outlier analysis.

Fluorescence data is analyzed in MATLAB using a series of scripts developed for this purpose. The first phase of this analysis is data processing, which consists of loading the data, smoothing, baseline correction, and normalization. After loading data into MATLAB, the data for each trial is trimmed to cut off the portion of the data collected before the laser is turned on and after the laser is turned off, leaving the laser rise to ensure none of the fluorescence decay is erroneously cut while still isolating the fluorescence decay for fitting.

Once the fluorescence decay is isolated for fitting, the baseline is adjusted to zero by subtracting the minimum value of the decay. The data is then smoothed using a moving average filter and normalized before averaging across all the trials with the same experimental settings (protein concentration, irradiance setting, and preparation method). Data is carefully examined after each step of data processing to ensure no artifacts are

introduced by the processing. Preparation of average decays concludes the data processing phase. Data analysis proceeds to the fitting phase.

Fitting begins by decreasing the total number of datapoints for faster fitting speeds using MATLAB and to weight the fits towards the fastest part of the decay. The first 15 points of the fluorescence decays are retained, and the rest of the points are culled using a logspace function to select logarithmically spaced points. This process weights the fits toward the beginning of the measurements, where dark state conversion occurs. Additional weighting is done by applying a weight to the first 10 data points and the last 5 points to ensure the fit function decays to the baseline. The average fluorescence decays are initially fit with a two-exponential function. If this results in a poor fit, then a three-exponential fit is tried. This approach leads to the minimal model that fits the data being selected, since an overly complex model with too many parameters will overfit the data and an oversimplified model will exclude normal patterns within the data are outliers. The fits are evaluated using the R^2 coefficients and the residuals. Fit parameter quality is evaluated using confidence intervals. A three-exponential fit based on the 3-level model including dark state conversion discussed in Chapter 1 is given in Equation 3.5.

$$F = a \cdot e^{-k_D \cdot t} + b \cdot e^{-k_{B1} \cdot t} + c \cdot e^{-k_{B2} \cdot t} + d$$

Equation 3.5 Three-exponential fit equation for fluorescence. k_D is the rate constant associated with the dark state. k_{B1} and k_{B2} are the first and second photobleaching rate constants, respectively. a, b, and c are the fractions of each exponential decay component.

The rate constants for the dark state and for photobleaching are extracted by first fitting to Equation 3.5, or a two-exponential version based on the best fit. The fastest component of the three-exponential fit is considered to be the dark state rate constant,

and the slower two components are photobleaching rate constants. This assignment is made because dark state conversion occurs on a much faster timescale compared to photobleaching. Blinking timescales have been measured for a variety of fluorescent proteins, and have been observed on timescales of hundreds of microseconds to millesconds,[58,65,74,75] while photobleaching has been measured on timescales from tens of milliseconds to seconds for several fluorescent proteins.[58,65]

In cases where none of the decay components are on the timescale of dark state conversion and ground state recovery and the fastest decay is on photobleaching timescales, the fastest decay would be designated k_{B1} instead of k_D. Otherwise for a two-exponential fit the two rate constants would be designated k_D and k_B. Figure 3.3 shows a sample two-exponential fit for miRFP670 fluorescence data.

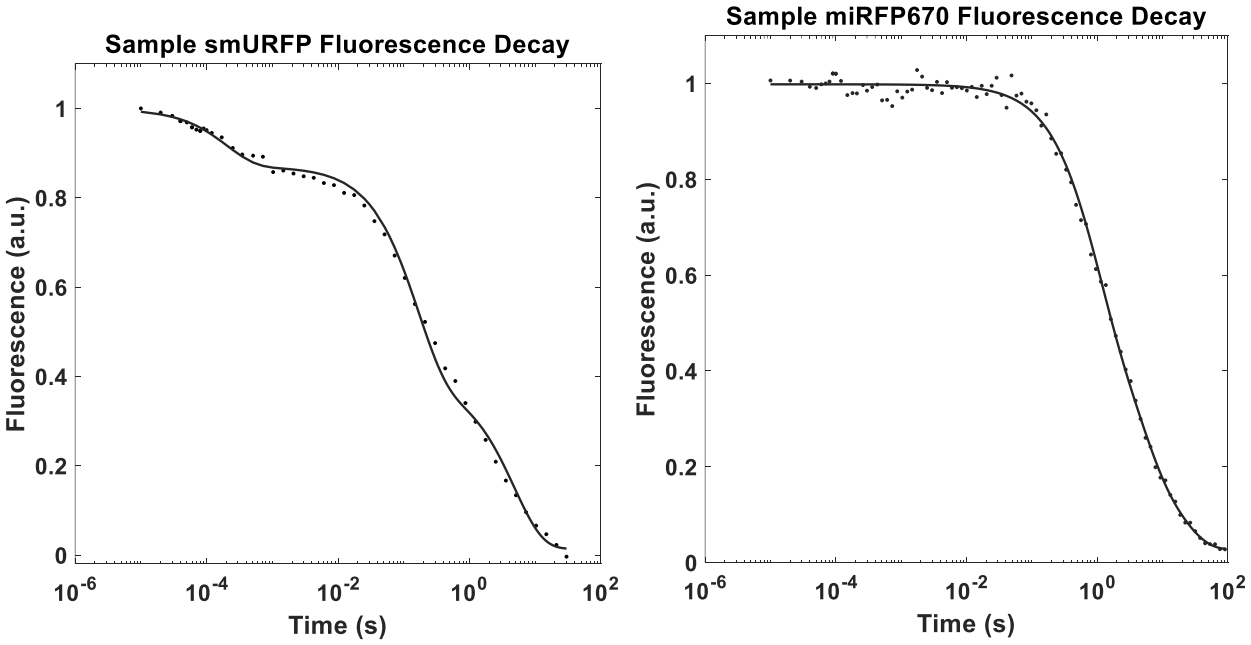

Figure 3.3 Sample miRFP670 and smURFP fluorescence decays. (a) Sample 3-exponential fit for continuous illumination fluorescence data of smURFP in microwells collected with an irradiance of 870 W/cm^2 (b) Sample 2-exponential fit for continuous illumination fluorescence data of miRFP670 in microwells collected with an irradiance of 2 kW/cm^2

In addition to this initial exponential fit to determine a rate constant associated with the dark state, the data is further analyzed by simulating data using a numerical to the system of kinetic equations describing the populations of these states (Equations 3.6).

$$\frac{d[S_0]}{dt} = -k_{ex}[S_0] + (k_{em} + k_{IC})[S_1] + k_{GSR}[D]$$

$$\frac{d[S_1]}{dt} = k_{ex}[S_0] - (k_{em} + k_{IC} + k_{DSC})[S_1] + k_{DS1}[D]$$

$$\frac{d[D]}{dt} = k_{DSC}[S_1] - (k_{S1D} + k_{GSR})[D]$$

Equations 3.6. Kinetic equations for 3-level system. S_0, S_1, and D are the ground electronic state, first excited state, and the dark state, respectively. k_{em}, k_{IC}, and k_{ex} represent rate constant for emission, internal conversion, and the excitation rate, respectively.

When modeling the results, several simplifications are made to find the simplest possible model that fits the data. The simplest model starts with just the two-level model where the dark state and rate constant leading to the dark state are omitted. If that model does not describe the data, the three-level model described by Equations 3.6 is used. A simplified version of this model starts by treating the rate of conversion from the dark state to the excited state as negligible. This simplification can be made because the dark state is lower energy compared to the excited state, so this rate constant will be small compared to other processes. The numerical solution was obtained in Python (http://www.python.org, Python Software Foundation, version 3.0) and plotted to compare the results to the experimental data. The k_{DSC} rate constant is estimated based on experimental results for other fluorescent proteins, and the value of k_D from the exponential fit is used for k_{GSR}, since ground state recovery is the rate limiting step of the

dark state processes. The values for k_{em}, k_{ex}, and k_{IC} are fixed within the fit equation are calculated based on the lifetime, fluorescence quantum yield, and extinction coefficient for the fluorescent protein. The equation used to calculate excitation rate is described in Equation 3.7.

$$k_{ex} = \frac{\ln(10) \cdot 1000 \cdot \varepsilon \cdot \lambda \cdot I}{h \cdot c \cdot N_A}$$

Equation 3.7. Equation to calculate excitation rate, k_{ex}. k_{ex} depends on extinction coefficient (ε), excitation wavelength (λ), and irradiance (I). h is Planck's constant, c is the speed of light, and N_A is Avogadro's number.

Data reduction is the final phase of data analysis. Initial data reduction occurs during data collection. Trials which showed fluorescence signal no higher than the blank were eliminated since they can be assumed to contain no fluorescent protein. Microwells or droplets which are non-fluorescent are assumed to be empty, and non-fluorescent *E. coli* cells are assumed to have low protein expression levels. After the data has been processed and fit, a careful evaluation of the fits is done to reduce the data set by eliminating outliers. An outlier is a measurement that substantially diverges from the other measurements made with the same collection settings (irradiance, fluorescent protein identity and concentration). An outlier could indicate one of two possibilities: the outlier could be an extreme example of the random variability intrinsic in the data or it could result from some deviation from the experimental procedure or an error in calculations. In the first instance the outlying data is an interesting facet of the fluorescent protein behavior and could indicate a separate mechanism, and in the second instance it is a data point that will skew results and should be excluded from analysis. Outlier analysis

involves balancing the need to keep valid observations while discarding flawed ones. If the source of the deviation is not readily apparent, careful statistical analysis is needed to determine whether the outlying data occurs from a deviation in the experimental procedure or an error in calculation. The key to this analysis is minimizing the risk of incorrectly rejecting a good observation during the data reduction process.[113,114]

The first step of data set reduction was to select only fluorescent traces with fluorescence signal at least 5-fold higher than the blank. This process will remove samples that have been excessively pre-illuminated from the analysis flow. Once this set is narrowed, the fluorescence decay of each trial is fit in addition to previously fitting the average decays and extracting the rate constants. The dark state and photobleaching rate constants from this set of measurements are used to calculate the average rate constant and standard deviation for the distribution of fits. These rate constants are used in statistical analysis for further data reduction. The z-value is calculated for each rate constant to give it a score based on how much it deviates (Equation 3.8).[115]

$$z = \frac{x_i - \bar{x}}{\sigma}$$

Equation 3.8. Equation for z-value test. x_i is the rate constant for the ith trial and $\bar{x}$ is the average rate constant for all trials at the same collection settings. σ is the standard deviation for rate constant for the set of collection settings.

A higher z-value indicates a higher likelihood that a data point should be rejected. This method assumes the data follows a normal distribution. When there are higher numbers of outliers within a data set, there will be a masking effect and the ability to use the rejection test to identify outliers is reduced.[114] Additional testing is used to evaluate whether more than one outlier should be removed. Each data set is evaluated based on

its kurtosis, a measure of the widths of tails of a probability distribution and skewness, a measure of the asymmetry of the probability distribution of the variable about the mean. The rate constants extracted from the exponential fits are used in the tests for kurtosis (Equation 3.9) and skewness (Equation 3.10).

$$k = n\sum_{i=1}^{n}\frac{(x_i - \bar{x})}{(n-1)^2\sigma^4}$$

Equation 3.9 Equation for test of kurtosis. x_i is the rate constant for the ith trial and $\bar{x}$ is the average rate constant for all trials at the same collection settings. n is the total number of samples. σ is the standard deviation.

$$s = \sum_{i=1}^{n}\frac{(x_i - \bar{x})^3}{(n-1)\sigma^3}$$

Equation 3.10 Equation for test of skewness. x_i is the rate constant for the ith trial and $\bar{x}$ is the average rate constant for all trials at the same collection settings. n is the total number of samples. σ is the standard deviation.

The kurtosis test is less sensitive to masking when there are multiple outliers and measures the thickness of tails for the distribution, and skewness measures the asymmetry of the distribution about the mean.[116,117] If excess kurtosis is over 2 or if skewness is greater than 1.5, then the trial with the highest z-value is removed from the dataset.

By removing outliers using these tests, outliers are removed from the dataset to avoid obscuring the analysis. While there was no trend in dark state rate constants for pre-illuminated samples, photobleaching rate constants would be affected by this phenomenon since the sample has been partially bleached. Following data reduction, the data is returned to the data processing phase following the arrow shown in the Figure 3.4

flow chart. Outliers are removed and the narrowed data set is used to construct a new average fluorescence decay. This average fluorescence decay is then fit and moved forward to the data analysis stages. The results from these measurements and the conclusions drawn for them are discussed in Chapter 4.

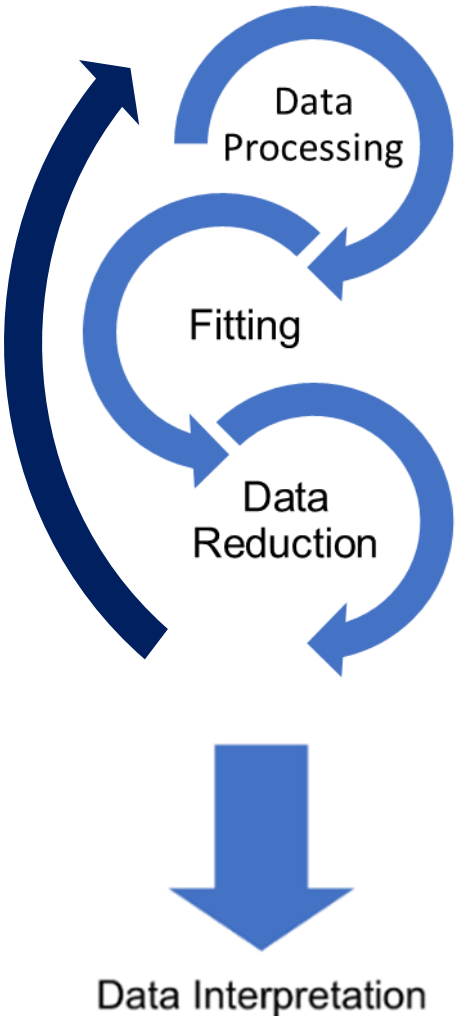

Figure 3.4 Overview of data analysis scheme. This scheme was used to analyze continuous illumination fluorescence data. This cycle was carried out until no further data reduction was performed, as determined by the kurtosis and skewness tests.

Chapter 4: Results of Dark State Analysis

4.1 Introduction

This section discusses the results of the study of dark state photophysics of near infrared fluorescent proteins. These measurements have important implications for using these proteins for deep tissue imaging and potentially super-resolution microscopy experiments by predicting blinking and photobleaching rates. In addition to comparing the dark state conversion behavior of these two proteins, measurements were also done at multiple irradiances to compare the dark state dynamics at excitation rates ranging from 2.5×10^5 to 4×10^7 s^{-1}.

Laser intensity used in these experiments is reported as an excitation rate rather than irradiance, because the excitation rate is a more accurate way to compare behaviors between fluorescent proteins with different extinction coefficients. At the same irradiance and excitation wavelength, a protein with a higher extinction coefficient will have a larger population of molecules in the excited state, resulting in higher rates of reactions that occur from the excited state, including dark state conversion and photobleaching. By using the excitation rate to compare the rates of dark state conversion and photobleaching, a more concrete comparison of the dark state behavior of different fluorescent proteins can be made.

Sections 4.2-4.4 present the results of continuous illumination experiments of fluorescent proteins smURFP, miRFP670, and mCherry. Sections 4.5 and 4.6 introduce the results of mathematical simulations and compare them to experimental results. Finally, sections 4.7-4.9 discuss the implications of this work and plans for further study.

4.2 smURFP Continuous Illumination Study

smURFP is a far-red fluorescent protein derived from allophycocyanin. It was selected for study because it has the highest molecular brightness of any biliverdin-based fluorescent protein. Continuous illumination measurements of smURFP followed the procedure described in detail in Chapter 3. Samples were loaded into microwells and examined at a range of irradiances (350 W/cm^2-20 kW/cm^2), obtained by attenuating the laser beam with a half waveplate and polarizer. Data was collected at a sampling rate of 100 kHz for 70 seconds with the 637 nm laser set to maximum power (140 mW). The processed data is shown in Figure 4.1. The data shows a trend of faster fluorescence decay rates as excitation rate increases. Looking more closely at the data, there are decays on multiple timescales, with a fast, microsecond timescale decay in addition to slow, millisecond timescale decays. The time axis is displayed on a log-scale to display and fit the data on both the fast and slow timescales.

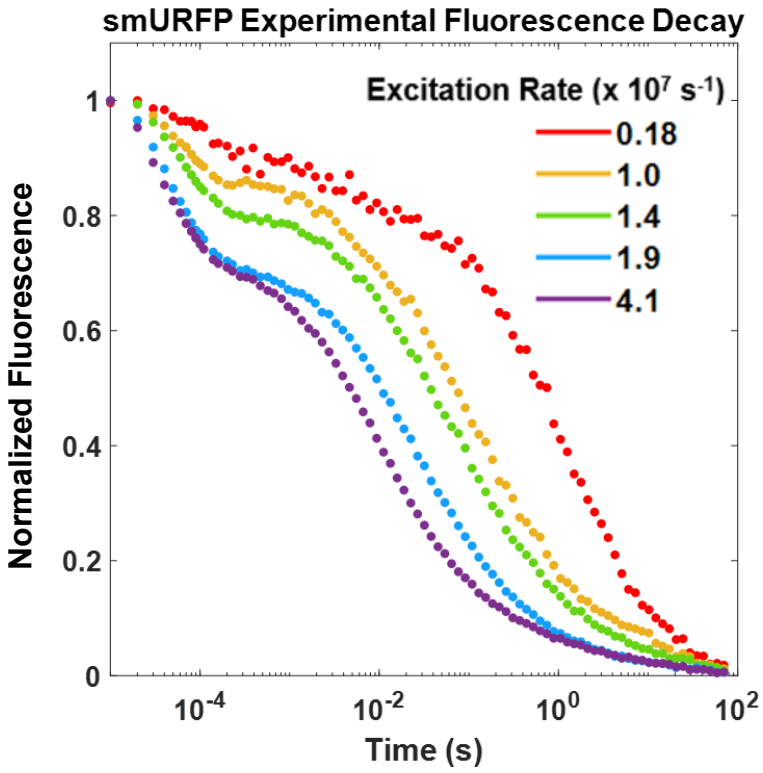

Figure 4.1. smURFP experimental data. Experiments are at excitation rates ranging from 1.8 x 10^6 s^{-1} to 4.1 x 10^7 s^{-1}. The data shown here is a normalized, baseline-corrected average at each set of experimental conditions, with the data set selected with the procedure described in Chapter 3. These experiments were performed for multiple purifications of smURFP

The data was fit using two-exponential, three-exponential, four-exponential, and five-exponential decays, as shown in Figure 4.2. Assessing the fits in Figure 4.2, clearly adding exponential terms to the fits improves the quality of the fit. Comparison of the residuals and confidence intervals for the fits support this claim. To avoid overfitting the data, the exponential terms from each fit were extracted and evaluated to determine whether the additional complexity was necessary to fully describe the data.

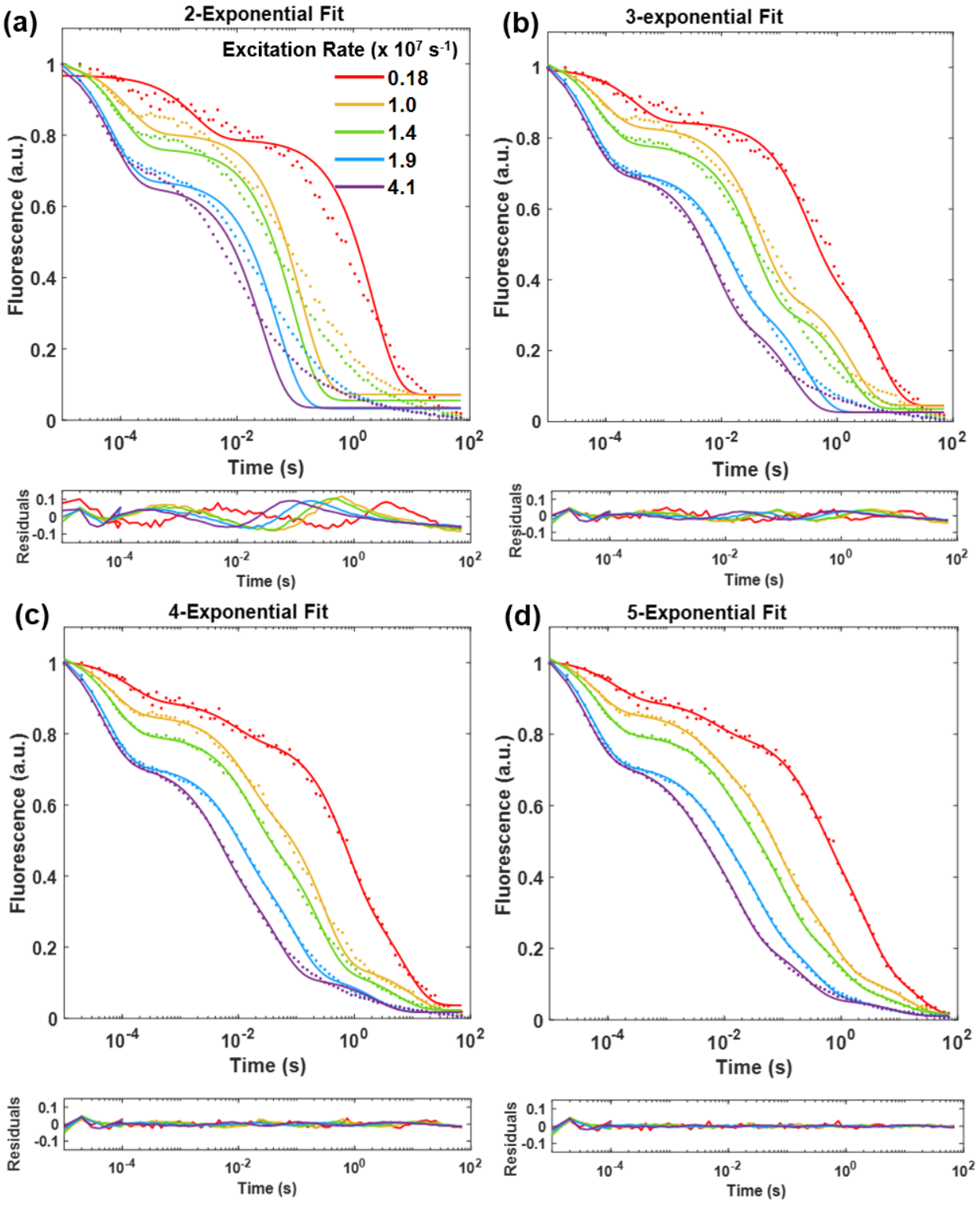

Figure 4.2 smURFP fits. (a-d) Two-, three-, four-, and five-exponential fits of smURFP data with residuals. Experiments are at excitation rates ranging from 1.8 x 10^6 s^{-1} to 4.1 x 10^7 s^{-1}. The data are fit with a sum of exponentials in accordance with the labels on each plot.

Comparison of the four and five-exponential fits for smURFP showed average variation in fit parameters of 5% across the five irradiances between the two fits. Comparing the three and four-exponential fit showed variation in fit parameters of 20% between the two fits. Closer inspection of the three-exponential fit in Figure 4.1 reveals that the region of the decay around 10^{-3} s is not fit very well, and so the four-exponential fit should be used to determine the most accurate determination of the fastest rate constant.

While the fastest rate constant can be accurately determined with the four-exponential fit, the remaining three rate constants extracted from the decay may be associated with irreversible photobleaching, and as such should reflect the appropriate trend with irradiance. This portion of the decay is overfit since the photobleaching is expected to increase with excitation rate, while none of the extracted rate constants for photobleaching show a clear trend for the four-exponential fit.

These fits could be improved by extending the time frame for each measurement. Although the higher irradiance measurements decayed to a stable baseline, collecting more points along this baseline would improve the quality of the fit. Many trials were performed to collect average decay behavior so collecting longer decays would limit the number that could be collected before the sample dried out. The other consideration with taking longer measurements is the limitation of the LabVIEW software memory capabilities. Collecting longer decays would require lowering the sample frequency from the 100 kHz used for the measurements and would reduce the quality of the fit for the fastest phase of the decay because the signal in this regime would be under sampled.

To ensure a more accurate fit of the fastest decay component given these constraints, the data was fit with a two-exponential fit up to the steady-state plateau. This period was chosen to include the fastest decay component, while exluding the decays at longer times. This corresponds to fitting up to 10 ms for the 1.8 x 10^6 s^{-1} excitation rate, 0.7 ms for the 1.0 x 10^7 s^{-1} excitation rate, and 0.3 ms for excitation rates from 1.4 to 4.1 x 10^7 s^{-1}. A fit from 10 µs up to 10 ms is shown at all excitation rates is shown in Figure 4.3 to illustrate this technique.

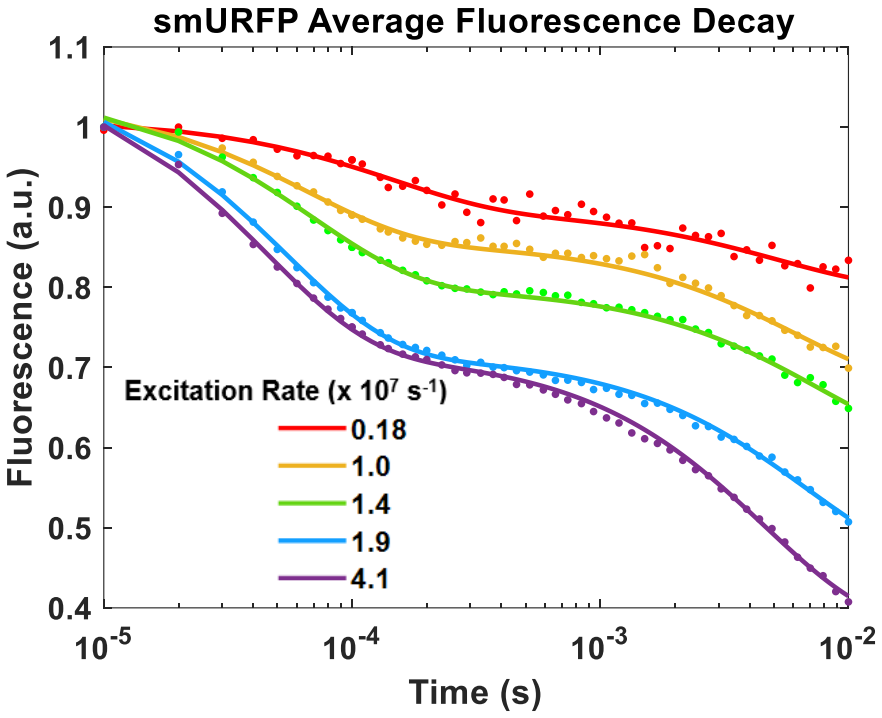

Figure 4.3 Two-exponential fit to the first 10 ms of the smURFP fluorescence decays. Excitation rates range from 1.8 x 10^6 s^{-1} to 4.1 x 10^7 s^{-1}. The fit is performed for the first 10 ms to illustrate the extraction of the microsecond-scale time constant.

The data in Figure 4.3 shows an intial, fast decay on the order of tens of microseconds. To extract fit constants on the millisecond-scale decays, fits were constructed from the steady-state plateau onwards. This was done using the same cut-

off times described when fitting the microsecond timescale component, fitting from 10 ms onward for the lowest excitation rate, 0.7 ms onward for the 1.0 x 10^7 s^{-1} excitation rate, and 0.3 ms onward for the three highest excitation rates. There is a clear trend with excitation rate, with faster fluorescence decays for both the fast and the slower components as excitation rate increases. The three-exponential fit equation that describes results on this timescale is given in Equation 4.1.

$$F = a \cdot e^{-k_1 \cdot t} + b \cdot e^{-k_2 \cdot t} + c \cdot e^{-k_3 \cdot t} + d$$

Equation 4.1 Equation for smURFP fluorescence decay. k_1, k_2, and k_3 are the rate constants extracted from the fits, with $k_1 > k_2 > k_3$. a, b, and c are the fractions of each exponential decay component.

The time constants determined from the smURFP exponential fits are listed in Table 4.1. The fastest time constant (t_1) is hypothesized to be related to dark state photophysics while the slower time constants (t_2 and t_3) are thought to be associated with irreversible photobleaching. This assignment is made based on comparison of these time constants to values reported from comparing multiple studies on FPs discussed in Chapter 1. [58,65,74,80]

Excitation Rate (s^{-1})	t_1 (μs)	t_2 (ms)	t_3 (s)
1.8×10^6	128	390	5.0
1.0×10^7	70	36	0.89
1.4×10^7	72	30	0.74
1.9×10^7	55	15	0.32
4.1×10^7	43	8.1	0.20

Table 4.1 Time constants obtained from fitting smURFP continuous illumination data. The time constants are obtained by taking the reciprocal of each rate constant. t_1, t_2, and t_3 are the time constants extracted from the smURFP exponential fits, in order of increasing time.

4.3 miRFP670 Continuous Illumination Study

miRFP670 was selected for study because it has the highest cellular brightness of any biliverdin-based fluorescent protein. miRFP670 is a useful far-red fluorescent protein to study because it was evolved from bacteriophytochromes and is part of a family of far-red fluorescent proteins that has been extensively studied.[41-46,118,119] The miRFP670 continuous illumination study followed the same procedure used for the smURFP experiments. Data was collected at a sampling rate of 100 kHz for 90 seconds with the 637 nm laser set to maximum power. The beam was attenuated with a half waveplate and polarizer to obtain a range of excitation rates. Figure 4.4 is a plot of the miRFP670 data. The data shows a trend of faster fluorescence decay rates as excitation rate increases. Unlike the data for smURFP, the miRFP670 data does not appear to show any fast, microsecond scale decays. The fastest decay is on the order of milliseconds.

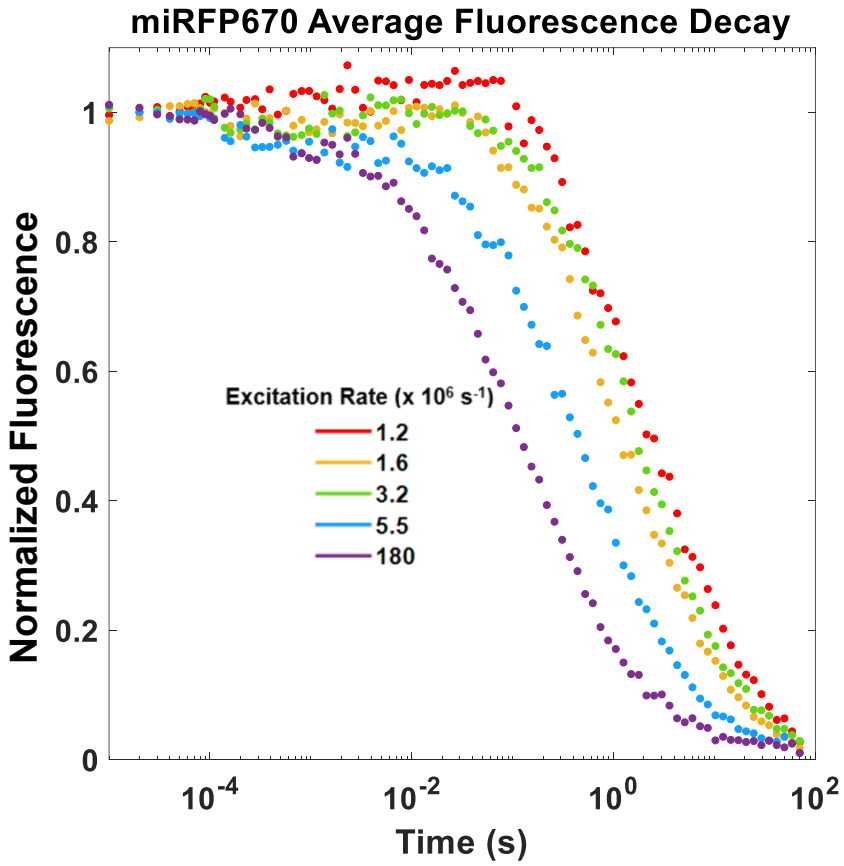

Figure 4.4. miRFP670 experimental data. Experiments are at excitation rates ranging from 1.2 x 10^6 s^{-1} to 1.8 x 10^7 s^{-1}. The data shown here is a normalized, baseline-corrected average at each set of experimental conditions, with the data set selected with the procedure described in Chapter 3. These experiments were performed for multiple purifications of miRFP670.

Initial fits of the fluorescence decay from two-exponential fit up to a four-exponential fit are given in Figure 4.5. As with fits for smURFP, adding additional terms to the exponential fit increases the quality of the fit, with the four-exponential fit most closely following the data, as assessed through examination of residuals and confidence intervals. To determine which fit best describes the data, a careful look was taken at the rate constants extracted from each fit. The four-exponential fit has multiple fit components with amplitudes that are much smaller than 1% of the decay, and while a trend of increasing photobleaching with irradiance is expected, the fit parameters do not show the

trend. While the three-exponential fit follows the data most closely, the third time-constant is much slower than the expected timescales of the processes being investigated, making this fit an unreliable descriptor of the data.

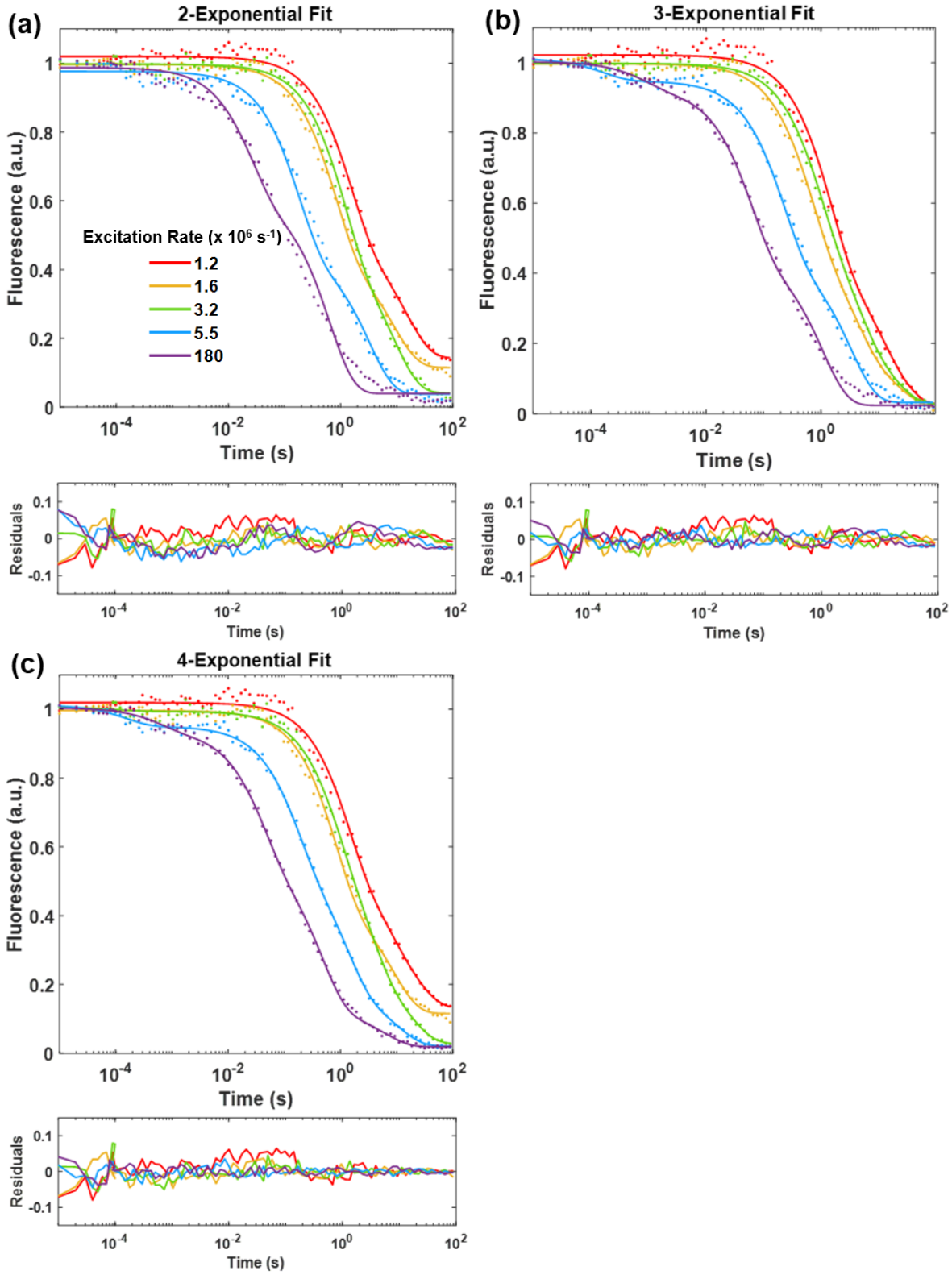

Figure 4.5 miRFP670 fits. (a-c) Two-, Three-, and Four-exponential fits of miRFP670 fluorescence data with residuals. Experiments are at excitation rates ranging from 1.2 x 10^6 s^{-1} to 1.8 x 10^7 s^{-1}.

Based on the considerations outlined above, the two-exponential fit is the best to describe the data, and outputs reasonable fit constants. Just as was done for smURFP, to ensure a more accurate fit of the millisecond decay components, the data was fit with a two-exponential fit from the steady-state plateau onward. This period was chosen to include the portion of the decay responsible for decay on a millisecond timescale. This corresponds to fitting from 10 ms onward for the 1.2 x 10^6 s^{-1} to 5.5 x 10^6 s^{-1} excitation rates, and 1 ms onward for the 1.8 x 10^7 s^{-1} excitation rate. A fit from 10 ms onward is shown at all excitation rates is shown in Figure 4.6 to illustrate this technique.

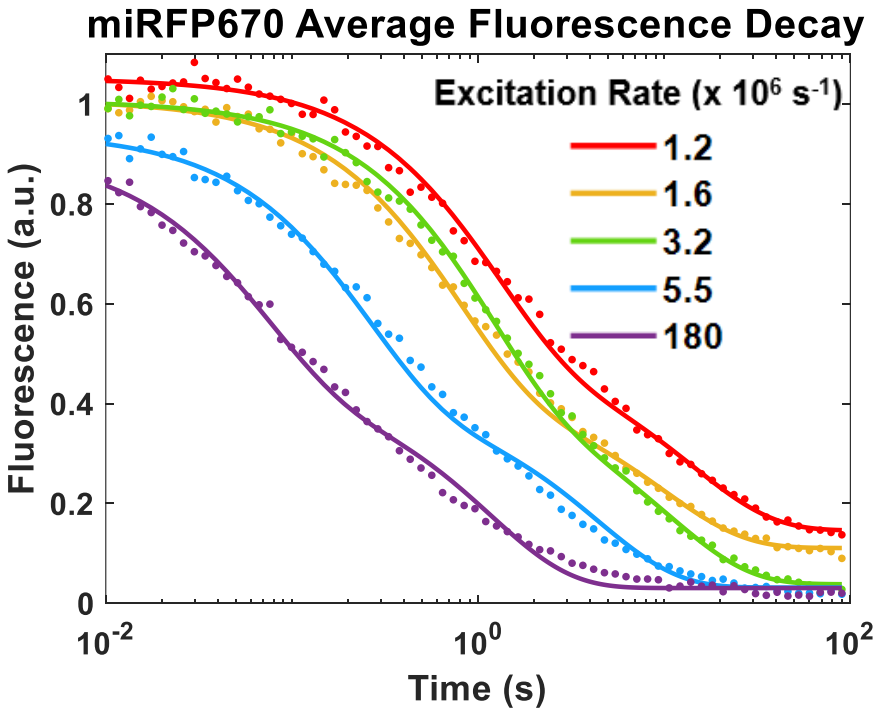

Figure 4.6 Two-exponential fit to miRFP670 fluorescence decays. Excitation rates ranging from 1.2 x 10^6 s^{-1} to 1.8 x 10^7 s^{-1}. The fit is from 10 ms onward to characterize the millisecond-scale fluorescence decays.

From the results shown in Figure 4.6 it appears that miRFP670 lacks the fast decay component that is attributed to dark state conversion in smURFP. Instead, the fastest decay component observed in the data for miRFP670 is on the timescale of ms. Based

on previous studies of dark state conversion and photobleaching in fluorescent proteins, at these irradiances fluorescence decay on this timescale can be assigned to photobleaching and not dark state conversion.[58,65,74,80] The two-exponential equation that describes the results on this timescale is given in Equation 4.2.

$$F = a \cdot e^{-k_1 \cdot t} + b \cdot e^{-k_2 \cdot t} + c$$

Equation 4.2 Two-exponential fit equation for miRFP670 fluorescence. k_1 and k_2 are the rate constants extracted from the fits, with $k_1 > k_2$. a and b are the fractions of each exponential decay component.

The time constants obtained from this fit are listed in Table 4.2. Both fluorescence decay timeconstants are conjectured to be associated with irreversible photobleaching. This assignment is made based on comparison to time constants reported in previous studies on various FPs. [58,65,74,80]

Excitation Rate (s^{-1})	t_1 (ms)	t_2 (s)
1.19 x 10^6	1020	14
1.61 x 10^6	640	9.2
3.16 x 10^6	1020	11.4
5.51 x 10^6	190	3.0
1.80 x 10^7	37	0.89

Table 4.2 Time constants obtained from fitting miRFP670 continuous illumination data. Time constants are obtained by taking the reciprocal of each rate constant. t_1 and t_2 are the time constants extracted from the smURFP exponential fits, in order of increasing time.

The reliability of both the model and parameters of the fit constants were assessed by comparing the data to mathematical modeling in Section 4.5. The mathematical modeling in that section relies on the rate constants extracted from the fit to generate simulated results.

4.4 mCherry Continuous Illumination Study

Continuous illumination experiments using mCherry were performed as a comparison to the experiments performed on smURFP and miRFP670. The experimental setup to investigate dark state photophysics in mCherry involves a 561nm CW laser source modulated externally by an Acuosto-Optical Modulator (AOM). The details of this experimental setup have been described in Chapter 3. Experimental data for mCherry is shown in Figure 4.7.

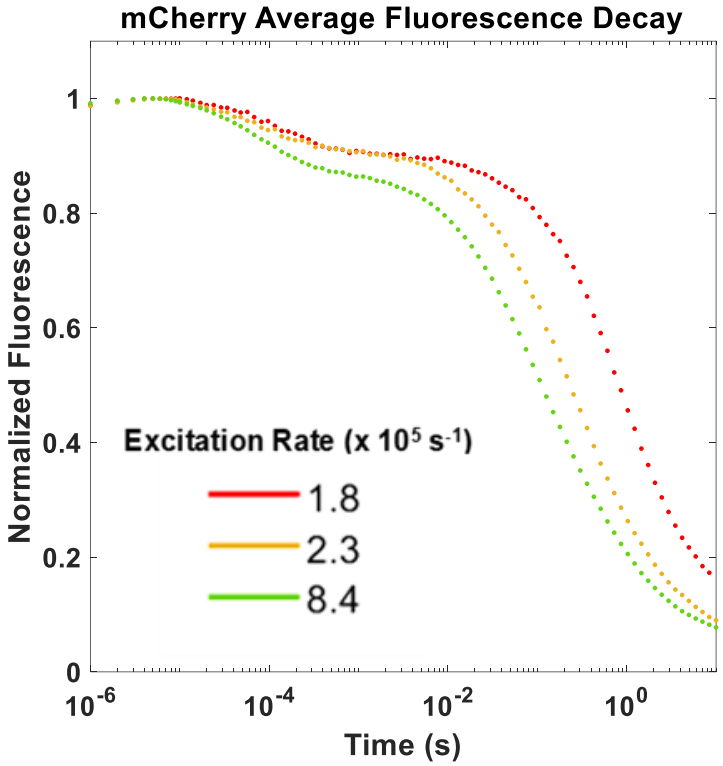

Figure 4.7. mCherry experimental data. Experiments are at excitation rates ranging from 1.8 x 10^5 s^{-1} to 8.4 x 10^5 s^{-1}. The data shown here is a normalized, baseline-corrected average at each set of experimental conditions, with the data set selected with the procedure described in Chapter 3.

Just as was done for smURFP and miRFP670, the mCherry data was fit with several sum of exponential functions and residuals and confidence intervals were used to assess fit quality. Two-, three-, and four-exponential fits are shown for mCherry in Figure 4.8 below.

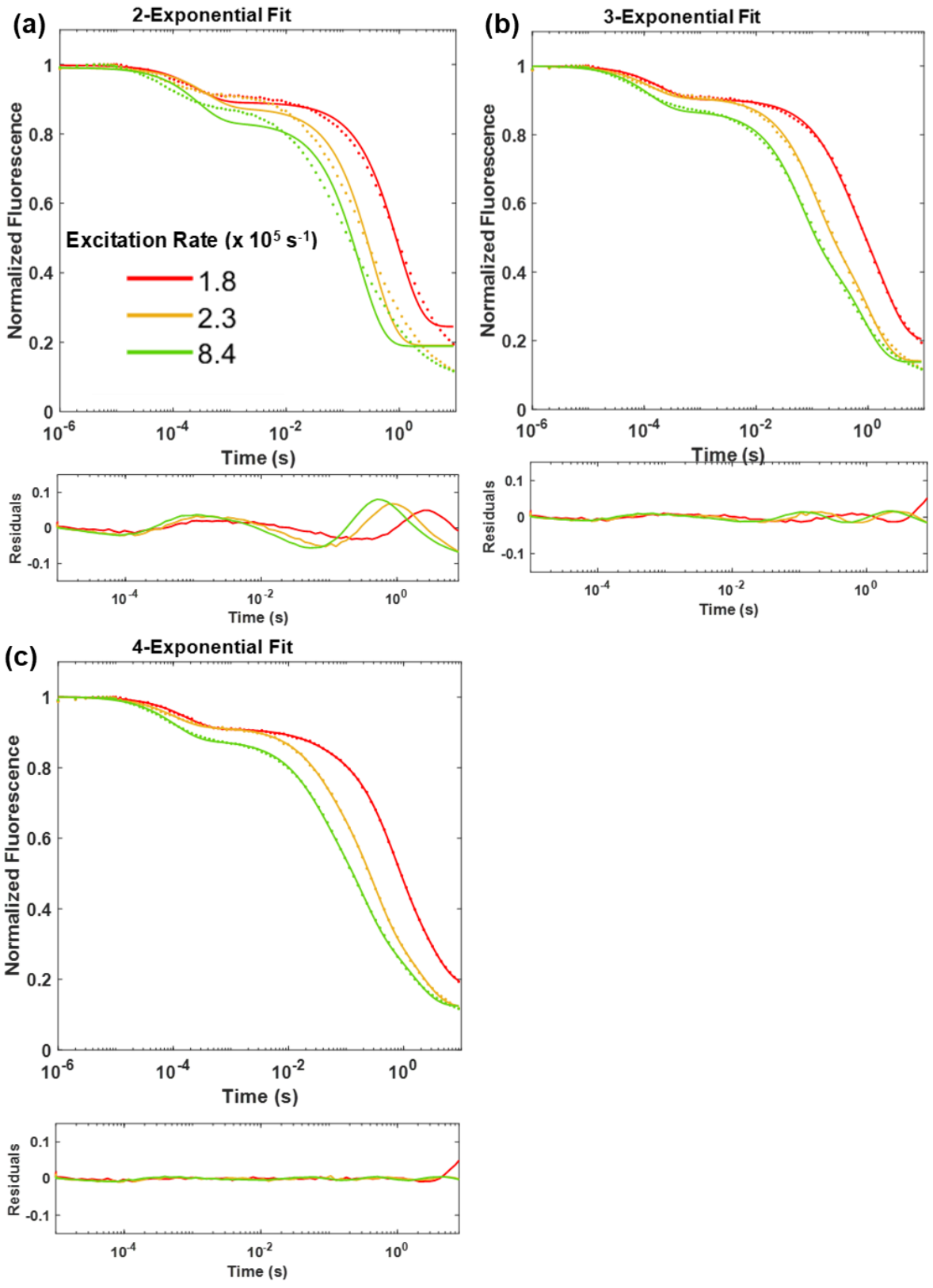

Figure 4.8. mCherry fits. (a-c) Two-, Three-, and Four-Exponential fits of mCherry fluorescence data with residuals. Experiments are at excitation rates ranging from 1.8 x 10^5 s^{-1} to 8.4 x 10^5 s^{-1}.

As before, the four-exponential fit decribes the data well, as determined by confidence intervals and residuals, but is more than is necessary to fit the data. The extracted bleaching rate constants for the two-exponential plot are in agreement with published mCherry data at higher irradiances.[65] Similar to the method used for smURFP, a two-exponential fit up to the steady-state plateau at 1 ms was selected to fit the dark state part of the curve (microsecond timescale), and a separate fit was done from 1 ms onward to fit the bleaching part of the curve (millisecond timescale). Figure 4.9 shows a two exponential fit up to 10 ms to illustrate.

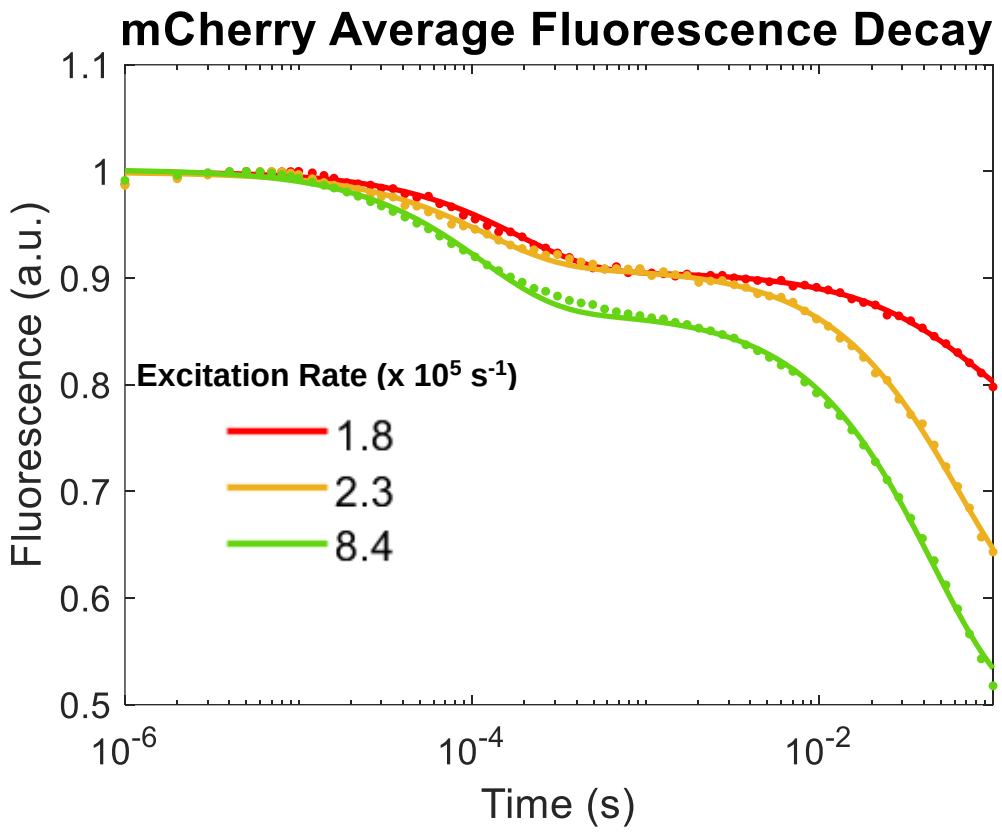

Figure 4.9 Two-exponential fit of mCherry fluorescence decays. Fit over first 0.1 s of the decay. Excitation rates ranging from $1.8 \times 10^5\ s^{-1}$ to $8.4 \times 10^5\ s^{-1}$

The initial, fast fluorescence decay in Figure 4.9 is on the order of hundreds of microseconds, while the second decay component is on the order of hundreds of milliseconds. Based on these timescales, although the fit was two-exponential like miRFP670, the fastest component is a result of the ground state recovery, while the slower component is attributed to photobleaching.[58,65] The fit equation describing this behavior is given in Equation 4.3.

$$F = a \cdot e^{-k_1 \cdot t} + b \cdot e^{-k_2 \cdot t} + c$$

Equation 4.3 Two-exponential fit equation for mCherry fluorescence. k_1 and k_2 are the rate constants extracted from the fits, with $k_1 > k_2$. a and b are the fractions of each exponential decay component.

The time constants obtained from this fit are listed in Table 4.3

Excitation Rate (s^{-1})	t_1 (µs)	t_2 (ms)
1.8 x 10^5	140	360
2.3 x 10^5	76	130
8.4 x 10^5	78	70

Table 4.3 Time constants obtained from fitting mCherry continuous illumination data. Time constants are obtained by taking the reciprocal of each rate constant. t_1 and t_2 are the time constants extracted from the smURFP exponential fits, in order of increasing time.

Comparing these measurements to a higher irradiance study on mCherry in our lab, the microsecond time constant from these measurements is over eight-fold faster compared to the previously determined ground state recovery time constant. In this study, the rate of dark state conversion in mCherry was found to be 2-fold faster at an excitation

rate of 2.4 x 10^6 s^{-1}, compared to our lower excitation rate of 8.4 x 10^5 s^{-1}.[58] The differences could be attributed to the differences in collection methods, with the previous study using frequency domain measurements to determine the rate of dark state conversion, while the ground state recovery rate constants were determined using pulsed excitation. This discrepancy indicates that a straightforward exponential alone cannot fully extract the rate constants from time domain data.

4.5 Comparison of smURFP and miRFP670 to RFPs

Rate constants determined from fits to smURFP, miRFP670, and mCherry data are compared in Figure 4.10 below. This figure illustrates that the fast, microsecond scale decay component (k_1) for smURFP is slower than dark state conversion for TagRFP-T and mCherry, while faster than ground state recovery for TagRFP-T and mCherry. This supports the hypothesis that the microsecond-scale component for smURFP is attributed to dark state photophysics. Comparing the k_2 and k_3 rate constants for smURFP to the reported bleaching rate constants for mCherry and TagRFP-T shows that the millisecond decays are on the same timescale as bleaching for these RFPs. This finding supports the hypothesis that the two millisecond decay components are due to photobleaching effects. Both rate constants for miRFP670 data (k_1 and k_2) are on slower timescales compared to the bleaching of mCherry and TagRFP-T.[58] This supports the hypothesis that both decay components for the miRFP670 decays are attributed to irreversible photobleaching.

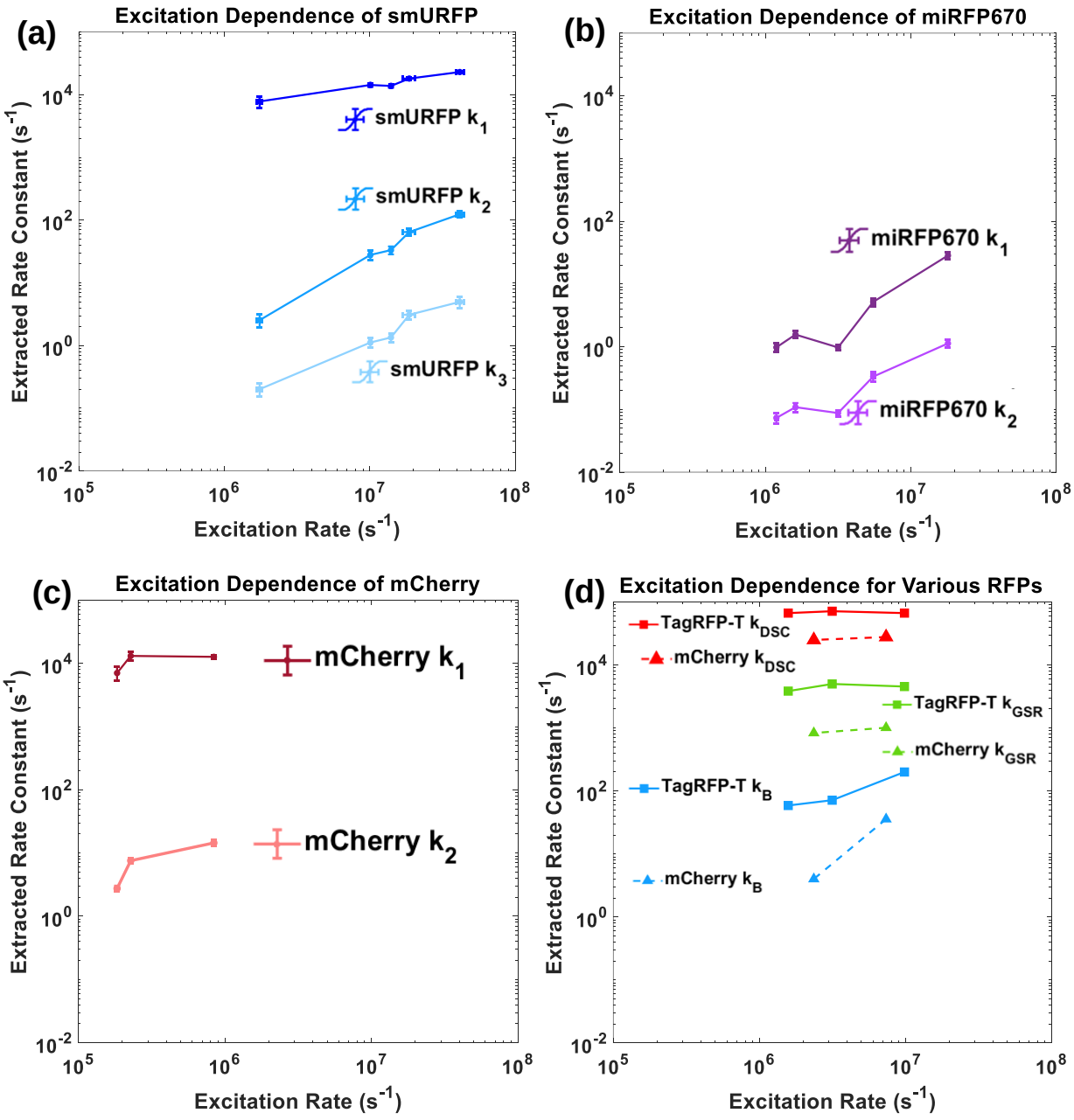

Figure 4.10 Comparison of rate constants (a) smURFP and (b) miRFP670, and (c) mCherry. Determined from exponential fits to experimental data. (d) Rate constants for dark state conversion (k_{DSC}), ground state recovery (k_{GSR}), and bleaching (k_B) for TagRFP-T and mCherry using reported values from Ref. 65.

4.6 Kinetic Modeling of Continuous Illumination Results

The exponential fits alone were not sufficient to interpret the fluorescence data. Kinetic modeling was needed to assess the assignment of rate constants to irreversible photobleaching or dark state photophysics. After generating the initial fits for smURFP, miRFP670, and mCherry described in sections 4.2-4.5, the extracted rate constants were used to simulate results by generating a numerical solution to the differential equations describing the system. The simplest model was chosen as a starting point and the simulated data was compared to the experimental data to assess whether that model accurately described the data. The simplest model that can be used is a two-level system with no dark state. The model is described by the two level energy diagram in Figure 4.11.

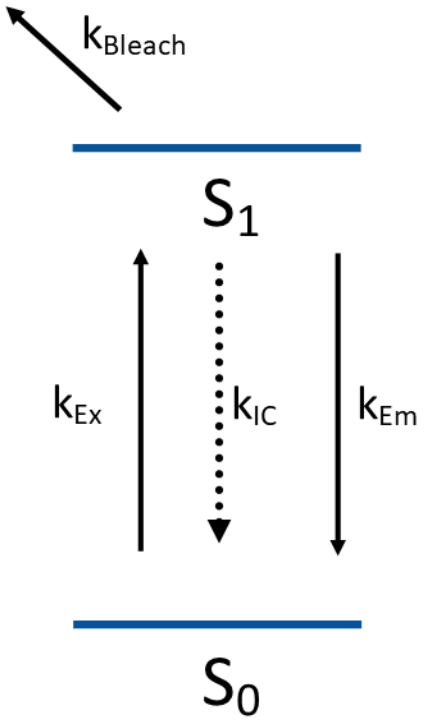

$$\frac{d[S_0]}{dt} = -k_{Ex}[S_0] + (k_{Em} + k_{IC})[S_1]$$

$$\frac{d[S_1]}{dt} = k_{Ex}[S_0] - (k_{Em} + k_{IC} + k_B)[S_1]$$

Figure 4.11. Two-level model diagram and equations. Two-level energy diagram (left) and rate equations (rightdefining kinetics of the states. S_0 is the ground state, S_1 is the excited state, k_{Ex}, k_{Em}, k_{IC}, and k_B are the excitation, emission, internal conversion, and photobleaching rate constants, respectively.

The numerical solution to the system of differential equations described in Figure 4.10 is obtained by using the differential equation solver “odeint” in Python with the initial normalized population of the ground state set to 1 and the initial population of the excited state set to 0. Values of k_{IC} and k_{Em} are set based on measured lifetimes and reported quantum yields for the fluorescent proteins. k_{Ex} is set based on the experimental conditions and k_B is the largest millisecond scale decay extracted from the exponential fits. Since the experimental results discussed here report on the ground state of the fluorescent protein, the resulting numerical solution for the S_0 state is plotted with respect to time and are compared to the fluorescence data generated experimentally. The simulated results for the S_0 state for miRFP670 are compared to the experimental results in Figure 4.12.

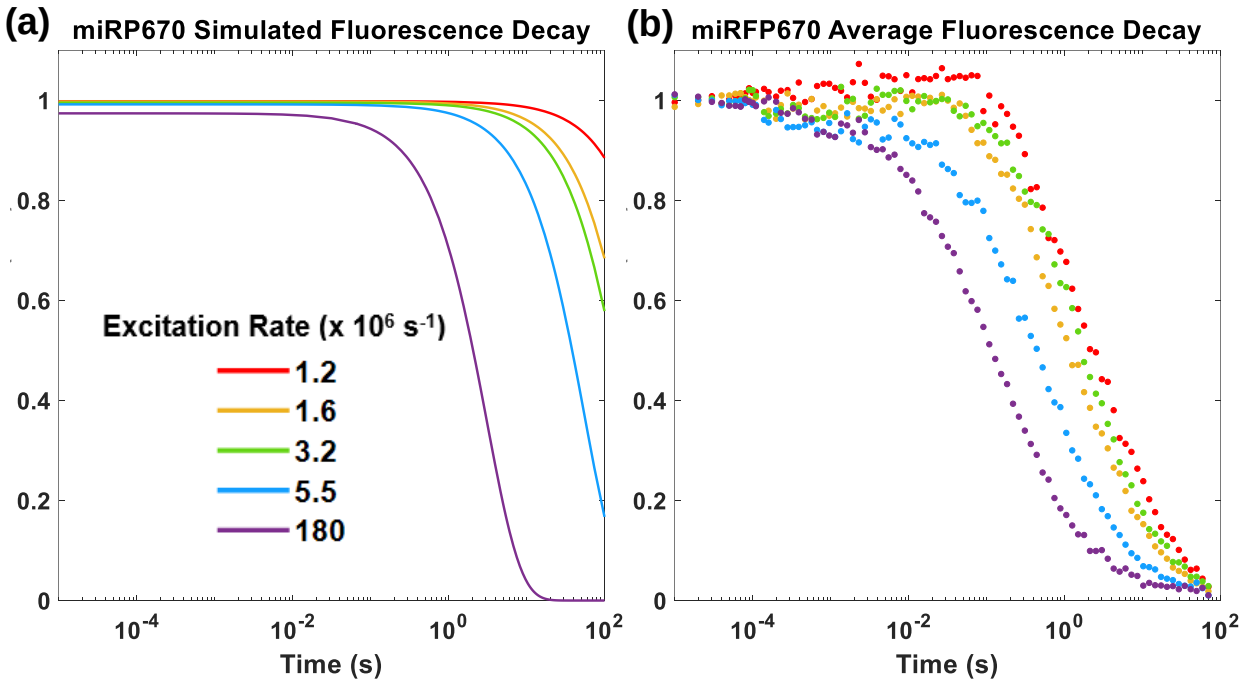

Figure 4.12. Comparison of miRFP670 two-level model to experimental results. (a) $S_0(t)$ simulated data for miRFP670 fluorescence decay based on two level model. (b) miRFP670 experimental data. k_{IC} was set 6.3 x 10^8 s^{-1} and k_{Em} was set to 9 x 10^7 s^{-1}. k_{Ex} values of 1.2 x 10^6 s^{-1}, 1.6 x 10^6 s^{-1}, 3.2 x 10^6 s^{-1}, 5.5 x 10^6 s^{-1}, and 1.8 x 10^7 s^{-1} were used with k_B values of 0.68, 1.6, 1.2, 52, and 778 s^{-1}, respectively.

Comparing the simulation to the experimental data the miRFP670 data seems to be well described by the two-level system and supports the hypothesis that miRFP670 does not exhibit dark state conversion. The simulated data shows slower overall decay, but qualitatively follows a similar shape to experimental data. This indicates that while the two-level model can be used to describe the miRFP670 data, more information about the system is needed to adjust the simulation parameters to more accurately describe the data. Since two bleaching rate constants were determined from the miRFP670 data, a second mechanism for bleaching should be incorporated into the model. One way to incorporate this feature would be to treat this as a three-state model in which photobleaching occurs from a dark state. While miRFP670 decays were slower than the timescales observed for fluorescent protein blinking in other studies, a fast conversion to the dark state with a high rate of bleaching would not be detected with these experimental conditions. This possibility is discussed below when assessing the smURFP simulated data. Additionally, while the fits for miRFP670 were restricted to 10 ms onward, a slight decay on the microsecond timescale can be observed for the data collected with a 1.8 x 10^7 s^{-1}, suggesting excitation-dependent miRFP670 dark state photophysics. Comparison to experiments done with other FPs support the possibility of an excitation-dependent dark state.[67]

After assessing the ability to describe miRFP670 data with a two-level model, the two-level model shown in Figure 4.11 was used to simulate smURFP data, using the excitation rates from experiments and the faster millisecond scale decay as the bleaching term, k_B. Data produced from the two-level model is compared to smURFP experimental data in Figure 4.13.

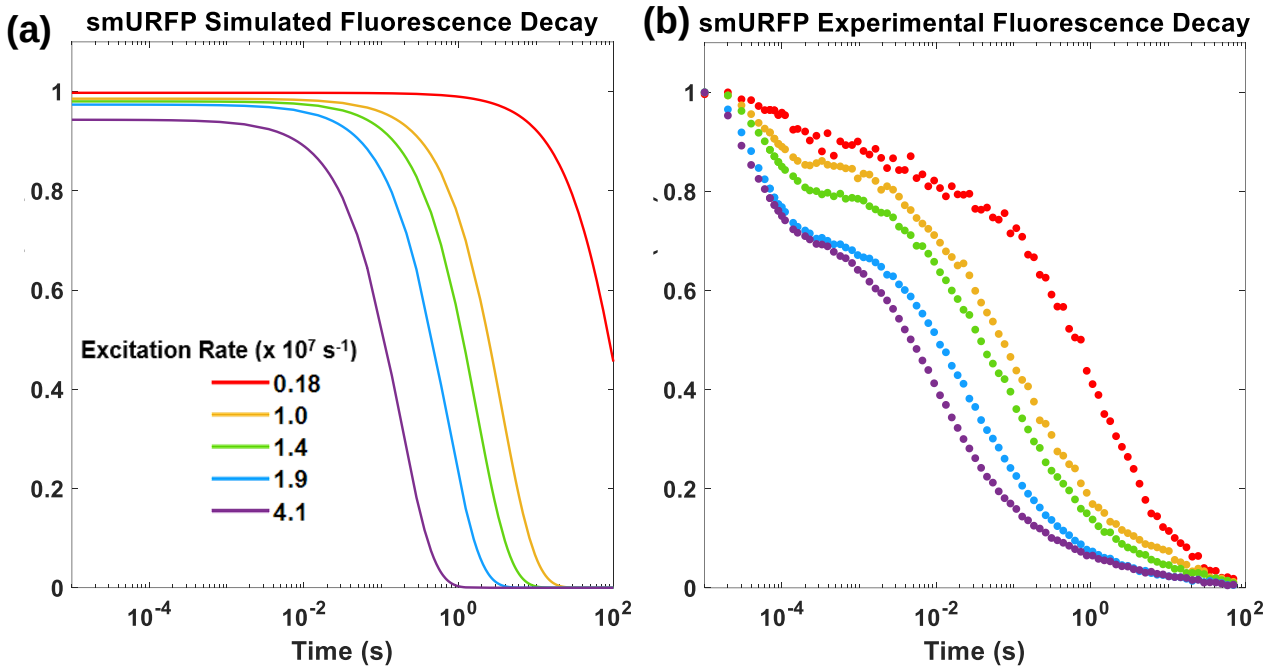

Figure 4.13 Comparison of two-level simulation to smURFP experimental data. (a) $S_0(t)$ simulated data for smURFP fluorescence decay. (b) smURFP experimental data. To simulate this data, k_{IC} was set 6 x 10^8 s^{-1} and k_{Em} was set 1 x 10^8 s^{-1}. k_{Ex} values of 1.8 x 10^6 s^{-1}, 1.0 x 10^7 s^{-1}, 1.4 x 10^7 s^{-1}, 1.9 x 10^7 s^{-1}, and 4.1 x 10^7 s^{-1} were used with k_B values of 3.0, 19, 30, 56, and 102 s^{-1}, respectively.

Comparing the curves generated in Figure 4.13, the fluorescence decay of smURFP is not accurately described by a two-level system and the dark state is needed to fully describe the fluorescence decay. The simulated two-level data lacks the microsecond scale decay observed in the smURFP experimental data. For this reason, a three-level diagram was applied next to incorporate the dark state into the simulation. The differential equations and the three-level energy diagram used to simulate the data are given in Figure 4.14. For simplicity, all irreversible photobleaching was assumed to occur from the dark state in this model.

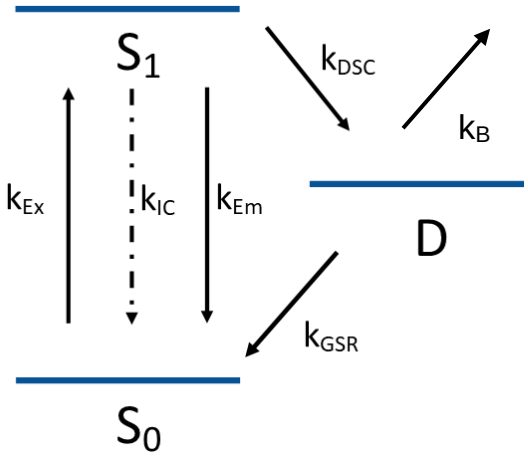

$$\frac{d[S_0]}{dt} = -k_{Ex}[S_0] + (k_{Em} + k_{IC})[S_1] + k_{GSR}[D]$$

$$\frac{d[S_1]}{dt} = k_{Ex}[S_0] - (k_{Em} + k_{IC} + k_{DSC})[S_1]$$

$$\frac{d[D]}{dt} = k_{DSC}[S_1] - (k_{GSR} + k_B)[D]$$

Figure 4.14 Three-level model diagram and equations. Three-level energy diagram (left) and differential equations (right) defining the kinetics of the states. S_0 is the ground state, S_1 is the excited state, and D is the dark state. k_{Ex}, k_{Em}, k_{IC}, and k_B are the excitation, emission, internal conversion, and bleaching rate constants, respectively. k_{DSC} and k_{GSR} are the rate constants for dark state conversion and ground state recovery, respectively.

As before, the numerical solution to the system of differential equations described in Figure 4.14 is obtained by using “odeint” in Python. The initial population of the normalized ground state is set to 1 and the initial populations of the excited and dark states are set to 0. Values of k_{IC}, k_{Em}, k_{ex}, and k_B are set the same as used for the two-level model. The value of k_{DSC} is unknown and was estimated 7 x 10^4 s^{-1} based on the assumption that k_{DSC} occurs faster than k_{GSR} as observed in dark state studies conducted on RFPs.[65,68] The value of k_{GSR} is set to the microsecond scale rate constant extracted from the fits. The resulting numerical solution for the S_0 state is then plotted and compared to the fluorescence data generated experimentally. The simulated results for the three-level model are compared to the smURFP experimental data in Figure 4.15.

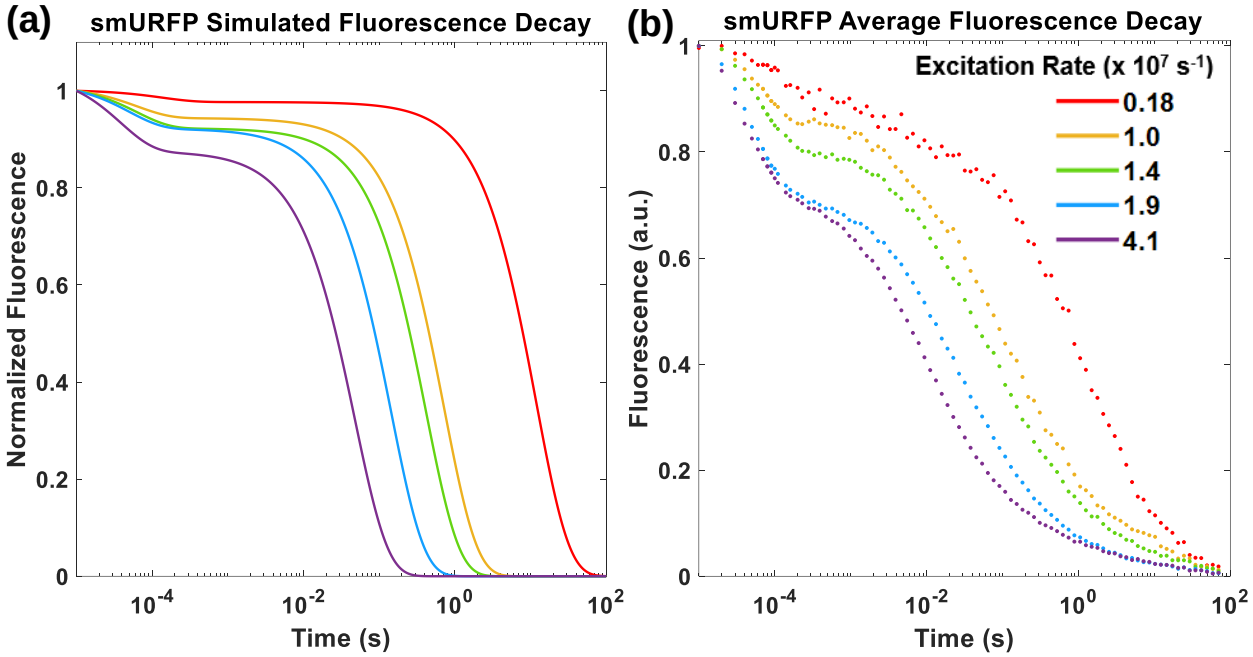

Figure 4.15. Comparison of smURFP simulated results using a three-level model (a) Simulated data for smURFP fluorescence decay based on three-level model. (b) smURFP experimental data. To simulate this data, k_{IC} was set 6 x 10^8 s^{-1}, k_{Em} was set to 1 x 10^8 s^{-1}, and k_{DSC} was set to 7 x 10^4 s^{-1}. k_{Ex} values of 1.8 x 10^6 s^{-1}, 1.0 x 10^7 s^{-1}, 1.4 x 10^7 s^{-1}, 1.9 x 10^7 s^{-1}, and 4.1 x 10^7 s^{-1} were used with k_B values of 3.0, 19, 30, 56, and 102 s^{-1} and k_{GSR} values of 2.3 x 10^3 s^{-1}, 1.17 x 10^4 s^{-1}, 1.2 x 10^4 s^{-1}, 1.6 x 10^4 s^{-1}, and 1.77 x 10^4 s^{-1}, respectively.

Both simulated and experimental data show a fast, microsecond decay and slower, millisecond decay. The microsecond decay component observed in the simulation is slower compared to the experiment, while the simulated decay component on the millisecond scale are faster compared with experiments. Qualitative comparison of the simulated data to the experimental data indicates that the three-level model generally describes the data, but deeper examination of the parameters is needed to understand the divergence between simulation and experiment.

As mentioned above the dark state conversion rate constant used in simulations was an estimate chosen based on comparison to studies on dark state photophysics observed in RFPs.[65] The estimate was selected based on the assumption that ground state recovery is the rate-limiting process, as observed for other FPs.[68] To interrogate this

assumption, the dark state conversion rate constant was varied while all other rate constants remained unchanged. The simulated data resulting from dark state conversion much slower than ground state recovery ($k_{DSC} << k_{GSR}$), about the same magnitude as ground state recovery ($k_{DSC} \sim k_{GSR}$), and much faster than ground state recovery ($k_{DSC} >> k_{GSR}$) is shown in Figure 4.16.

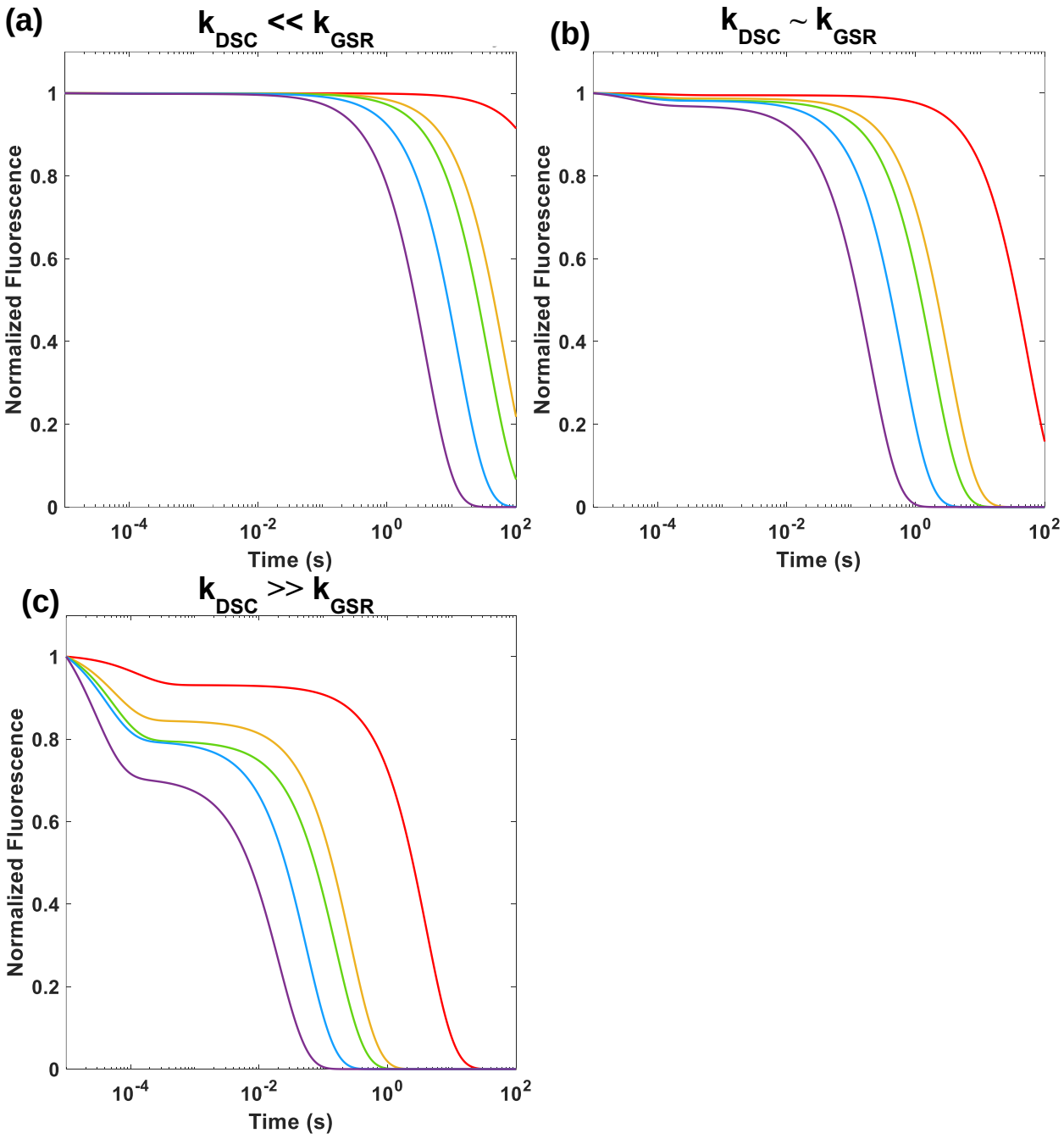

Figure 4.16. Effect of k_{DSC} on simulated data. Parameters: k_{IC} = 6 x 10^8 s^{-1}, k_{Em} = 1 x 10^8 s^{-1}. k_{Ex} values of 1.8 x 10^6 s^{-1}, 1.0 x 10^7, 1.4 x 10^7, 1.9 x 10^7, and 4.1 x 10^7 s^{-1} were used with k_B values of 3.0, 19, 30, 56, and 102 s^{-1}. k_{GSR} values were 2.3 x 10^3, 1.17 x 10^4, 1.2 x 10^4, 1.6 x 10^4, and 1.77 x 10^4, respectively. (a) k_{DSC} = 7.2 x 10^2 s^{-1}, an order of magnitude slower than the slowest k_{GSR} value. (b) k_{DSC} = 1.5 x 10^4 s^{-1}, the median value for k_{GSR}. (c) k_{DSC} = 2.2 x 10^5 s^{-1}, an order of magnitude faster than the fastest k_{GSR} value.

The results of the simulations in Figure 4.16 support the assumption that dark state conversion occurs much faster than ground state recovery. If dark state conversion is slower, as in Figure 4.16 (a), no microsecond scale decay component is observable because there is not accumulation of dark state population. If dark state conversion is on the same order of magnitude as ground state recovery, as in Figure 4.16 (b), a slight microsecond decay component can be observed, but it is so slight that it may be lost in the experimental noise if the dark state conversion of a protein with these properties were measured. This small microsecond decay component can be attributed to a small accumulation of population in the dark state. The last scenario, where dark state conversion is faster than ground state recovery (Figure 4.16 (c)), most closely resembles smURFP experimental data, showing a sharp microsecond decay component, suggesting higher accumulation of population in the dark state. Careful comparison of experimental and simulated data narrowed the range of values for dark state conversion to between 7.4×10^4 and $2.2 \times 10^5\ s^{-1}$.

Although the simulations in Figure 4.16 were based on smURFP experimental rate constants, they can also inform interpretation of the miRFP670 data. The scenarios observed in Figure 4.16 (a) and (b) could describe miRFP670, in which the dark state conversion effects could be classified as either not observed as in (a) or very slight as in (b). While miRFP670 data was described by a two-level system, dark state photophysics could describe the slight microsecond decay observed for the $1.8 \times 10^7\ s^{-1}$ excited state and the multiple timescales for photobleaching.

Following assessment of the dark state conversion parameter, the three-level model was adjusted by adding a second photobleaching decay term. The 3-level diagram

and kinetic equations describing this adjustment are shown in Figure 4.17. According to this model, bleaching from the dark state (k_B) is greater than bleaching from the excited state (k_{B2}). Addition of photobleaching from the excited state had a negligible effect on the simulated data and resulting simulations were indistinguishable from the previous model.

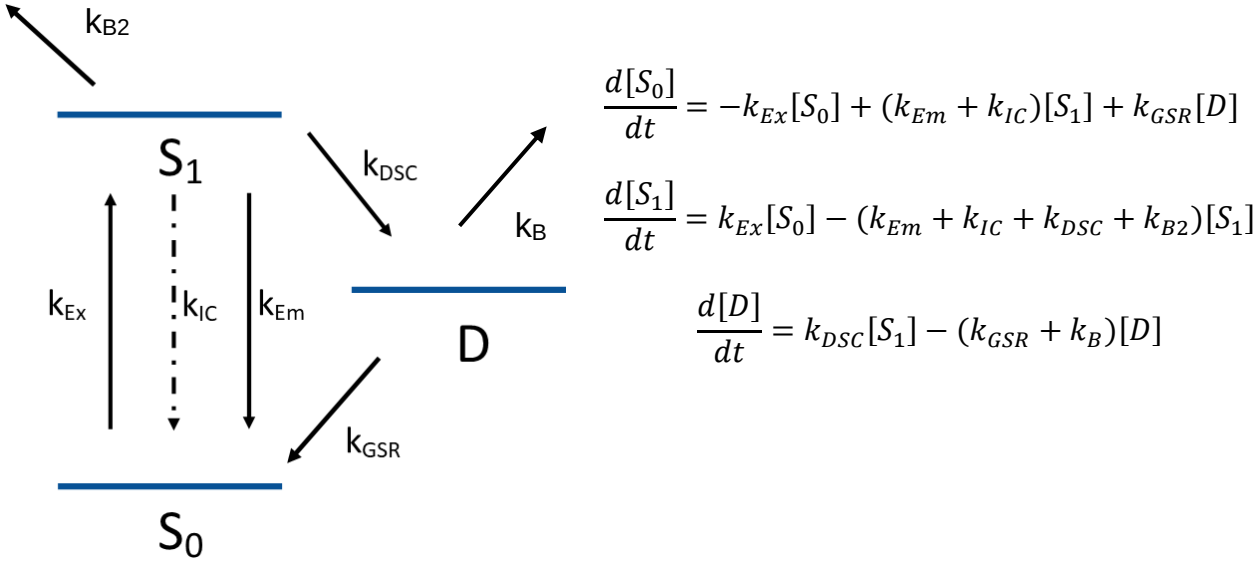

Figure 4.17 Three-level model with excited-state bleaching. Three-level energy diagram (left) and differential equations (right) defining the kinetics of the states. S_0 is the ground state, S_1 is the excited state, and D is the dark state. k_{Ex}, k_{Em}, k_{IC}, k_B, and k_{B2} are the excitation, emission, internal conversion, dark state bleaching, and excited state bleaching rate constants, respectively. k_{DSC} and k_{GSR} are the rate constants for dark state conversion and ground state recovery, respectively.

The effect of irreversible photobleaching on the relative rate of the millisecond fluorescence decay was further investigated by switching the bleaching values so that the larger bleaching rate constant was assigned to the excited state. The effects of this switch are shown in Figure 4.18. This plot shows that when the larger bleaching component is assigned to the dark state rather than the excited state, there is a shorter dwell time in steady state, and faster overall fluorescence decay. This supports the initial assignment

of the faster millisecond bleaching rate constant as associated with irreversible photobleaching from the dark state.

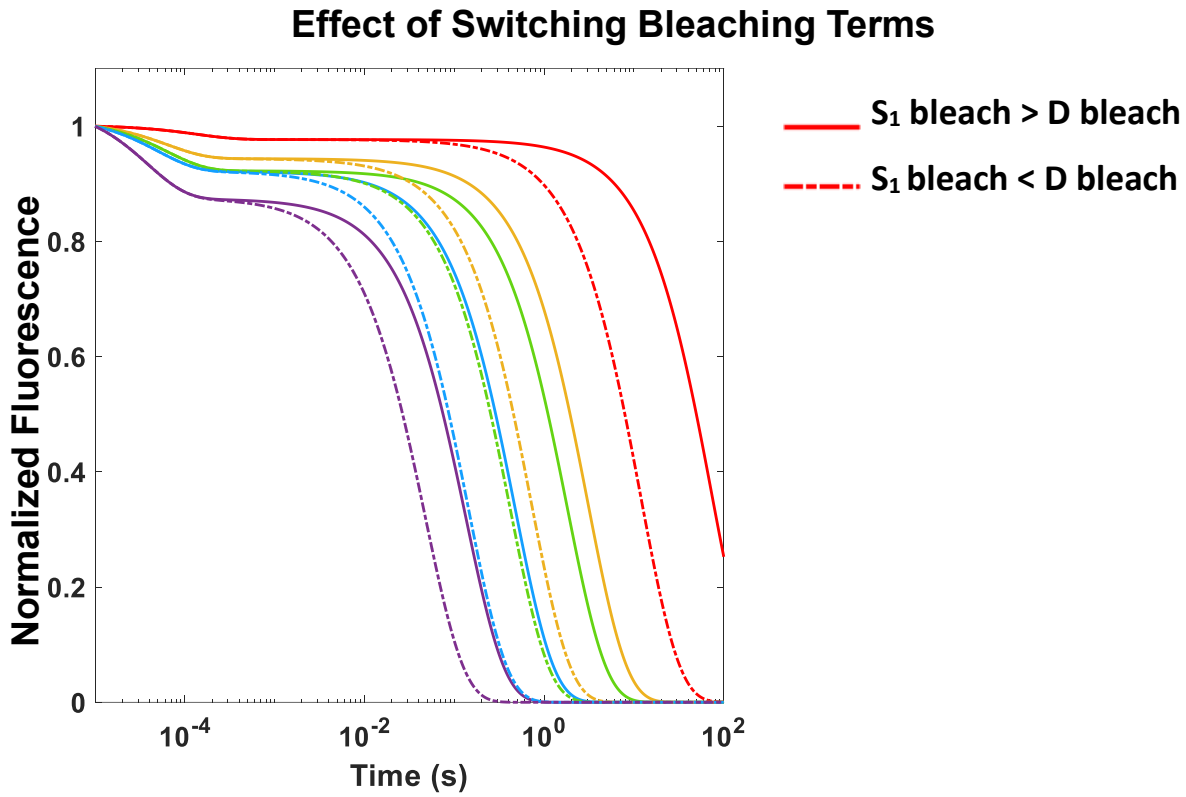

Figure 4.18 Effect of switching bleaching terms on simulated data. The k_B and k_{B2} terms determined experimentally are switched within the model to predict source of bleaching. k_{IC} was set 6 x 10^8 s^{-1}, k_{Em} was set to 1 x 10^8 s^{-1}, and k_{DSC} was set to 7 x 10^4 s^{-1}. k_{Ex} values of 1.8 x 10^6 s^{-1}, 1.0 x 10^7 s^{-1}, 1.4 x 10^7 s^{-1}, 1.9 x 10^7 s^{-1}, and 4.1 x 10^7 s^{-1} were used with k_B values of 3.0, 19, 30, 56, and 102 s^{-1}, k_{B2} values of 0.20, 0.55, 0.69, 3.4, and 6.0 s^{-1}, and k_{GSR} values of 2.3 x 10^3 s^{-1}, 1.17 x 10^4 s^{-1}, 1.2 x 10^4 s^{-1}, 1.6 x 10^4 s^{-1}, and 1.77 x 10^4 s^{-1}, respectively.

Comparison of the models developed to experimental data revealed that in the case of miRFP670, the two-level model qualitatively represents the experimental results, but the fluorescence decay in the simulation is too slow compared to the experiment. A careful look at the investigation into the effects of adjustments to the dark state conversion rate constant (k_{DSC}) on the simulated results revealed that miRFP670 could also be described by a three-level model in the scenario where $k_{DSC} \leq k_{GSR}$.

In the case of smURFP, the three-level model best represented the experimental results, and the simulation of this model allowed the k_{DSC} parameter to be estimated. The value of k_{DSC} over the irradiance range studied was found to be between 7.4 x 10^4 and 2.2 x 10^5 s^{-1}. This estimate allowed the single molecule fluorescence blinking times to be predicted, using Equations 4.4 and 4.5 below. Calculated τ_{on} values were between 60 µs and 5 ms and τ_{off} values between 40 and 130 µs for the excitation rates ranging from 1.8 x 10^6 s^{-1} to 4.2 x 10^7 s^{-1}. Based on these values, smURFP is expected to blink twice as fast as mCherry, and TagRFP-T blinks 1.2-fold faster than smURFP.[65] While brighter fluorescent proteins are ideal for super-resolution experiments, this fast blinking predicted for smURFP indicates that further development of smURFP could be advantageous for super-resolution imaging.

$$\tau_{on} = \frac{1}{k_{ex} * k_{DSC} * \tau_{em}}$$

Equations 4.4 Expression to calculate the on time (τ_{on}) for a fluorescence trajectory. k_{ex} is the excitation rate constant, k_{DSC} is the dark sate conversion rate constant, and τ_{em} is the fluorescence lifetime.

$$\tau_{off} = \frac{1}{k_{GSR}}$$

Equations 4.5. Expression to calculate the off time (τ_{off}) for a fluorescence trajectory. k_{GSR} is the ground state recovery rate constant.

4.7 Discussion

Insight into these dark state conversion results requires looking closely at previous studies on BV-binding fluorescent protein and their origins. miRFP670 was developed from bacteriophytochromes, which are composed of the PHY, PAS, and GAF domains, with the GAF domain being the site of most chromophore protein contacts.[117,120-122] Biliverdin binding occurs via a cysteine to the vinyl side chain of the BV A-ring.[121-122] The biliverdin chromophore sits within its binding pocket, with steric interactions and hydrogen bonding interactions holding it in place. Light activation of the phytochromes involves isomerization about the C15=C16 double bond in biliverdin, resulting in a flip of the D-ring.[117,120] In solution, the preferred conformation of biliverdin is mostly helical with extended forms present in smaller proportion, but is extended when bound to protein.[18,40]

Brighter, blue-shifted mutants of a bacteriophytochrome were generated by incorporating cysteine residues for BV binding in the GAF and the PAS domain rather than the PAS domain alone. This group of blue-shifted mutants includes iRFP670, and the study found that the blue-shift is attributed to the sp^3 hybridization of the biliverdin carbon that binds the cysteine residue instead of forming a double bond, reducing the extent of π-electron conjugation to exclude the BV A-ring.[118] The same blue shift is also observed in miRFP670. The increase in fluorescence lifetime for these blue-shifted mutants is linked to the increase in steric constraints about the BV A-ring, reducing A-ring motion, and the reduction of π-conjugation so that it does not extend to the A-ring, affecting the rate of decay from the excited state.[118] The miRFP670 biliverdin-binding pocket is shown in Figure 4.19

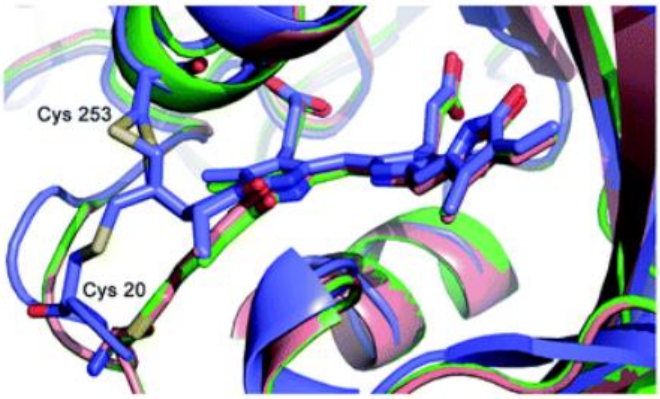

Figure 4.19. Protein environment around chromophore for miRFP proteins. From crystal structure. Shows environment around miRFP670 (blue), miRFP703 (green), and miRFP709 (red). Image from Ref. 81.

In the development of near infrared fluorscent proteins (NIR FPs), the PHY domain was truncated and mutations of key residues in the GAF domain blocked photoconversion.[34,41,42] A femtoseond transient absorption spectroscopy experiment on iRFP670, a miRFP670 precursor, confirmed that there was no significant formation of ground-state photoproducts associated with photoconversion.[118,119] A resonance Raman study on iRFP reveals the protein has fewer hydrogen bonding interactions with ring D and fewer water molecules around ring D compared to the phytochrome from which it is evolved.[123] The flexibility of the chromophore is reduced, especially around ring A and D and there is an overall reduction in conformational heterogeneity compared to wild-type proteins. The T258F mutation may have strengthened hydrophobc interactions with ring D, packing the chromophore more tightly.[123]

Time-resolved fluorescence studies in H_2O and D_2O found significant kinetic isotope effects in fluorescence lifetimes for red-shifted and blue-shifted mutants. Kinetic isotope effects of ~1.8 for all lifetimes above 0.8 ns were reported.[118,119] This result is consistent with spectroscopic studies of other iRFPs and with wild-type BphPs that had similar kinetic isotope effects, indicating that the excited-state proton transfer (ESPT)

model of proton transferred from the pyrrole to the protein backbone observed in these proteins is also a potential pathway for non-radiative decay in iRFP670.[124-126]

An ultrafast spectrscopic study comparing behaviors of two wild-type bacteriophytochromes investigated the kinetic isotope effect in these proteins. The study found that the rate-limiting process for excited-state deactivation was a proton transfer reaction. Replacing amino acid residues attributed to hydrogen bonding decreased the rate of excited state decay while increasing the rate of isomerization product formation. From these results, the breaking of hydrogen bonds surrounding the chromophore was determined to be rate-limiting for isomerization about the C15=C16 double bond, and these hydrogen bonds must be disrupted to form photoproducts in the wild-type bacteriophytochromes.[124] Additionally, the biliverdin pyrrole ring deprotonation competes with isomerization about the C15=C16 as a deactivation pathway.[124-125,127] The process of excited-state proton transfer is shown in Figure 4.20. QM/MM computations on a wild-type bacteriophytochrome reproduce absorption and emission energies[57] and qualitatively support isomerization around the biliverdin D-ring as a possible pathway of excited-state nonradiative decay in phytochromes.[128]

The studies discussed here inform the interpretation of the dark state conversion results for the smURFP and miRFP670. miRFP670 can be more directly compared to the studies on bacteriophytochromes discussed here since it was evolved from the blue-shifted variants in which motion of the A-ring and D-ring has been constricted,[46] whereas smURFP is based on directed evolution of allophycocyanin (APC) to generate a biliverdin-binding variant. Since only the Y56A mutant of smURFP has been crystallized, interpretation of its results and comparison to miRFP670 results requires consideration

of the photophysics of biliverdin to infer the protein environment surrounding the chromophore.

Although the two near-infrared fluorescent proteins studied here both use biliverdin as a chromophore they exhibited vastly different behavior. While smURFP exhibited fast dark state conversion, no dark state conversion was measured for miRFP670 at the irradiances studied. The additional exponential terms required to fit smURFP compared to miRFP670 likely stems from structural heterogeneity of the smURFP molecule, including the tendency to dimerize and ability to bind 1 or 2 BV molecules.[37] One possible interpretation of the smURFP results is a distinct isomerization rate observed for each conformation. Based on the mutations and structural studies done on precursors to miRFP670, dark state conversion may be inhibited by the reduced mobility of the BV A-ring and the BV D-ring. No such structural studies were done on smURFP, but studies discuss above on biliverdin alone and bound to protein indicate that isomerization about the C15=C16 bond may be a deactivation pathway for smURFP.[124-125,127] Figure 4.20 (a) shows the protein environment around biliverdin based on a homology model and Figure 4.20 (b) shows the biliverdin binding pocket of a low quantum yield mutant, smURFP Y56R.[37,129] Additional study on NIR FPs that lack the A-ring and D-ring stabilization would grant further insights into the mechanisms behind DSC in biliverdin-based fluorescent proteins, in addition to deuterium exchange experiments to assess the role of proton transfer in dark state conversion for these proteins.

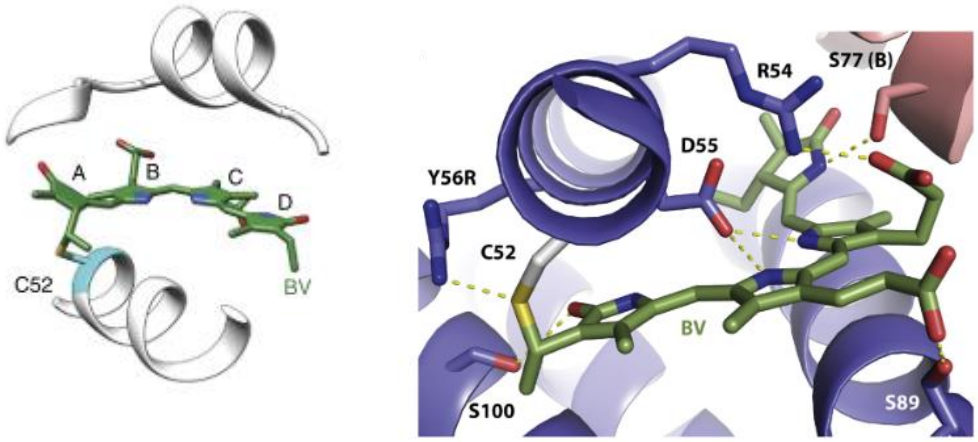

Figure 4.20. Protein environment of smURFP chromophore. (a) smURFP homology model. Picture from Ref. 37. (b) Crystal structure of smURFP Y56R. Picture from Ref. 129.

The fluorescence decay component for with the smURFP dark state was found to vary from 46-140 µs across the excitation rates measured (1.8×10^6 to 4.1×10^7 s^{-1}). Based on the above analysis, this decay component is most comparable to the ground state recovery rate constant, indicating smURFP blinking is 2-fold faster than mCherry and slower than TagRFP-T blinking.[65] The fastest decay component for miRFP670 varied from 25-670 ms, likely associated with bleaching since it occurred much more slowly than blinking timescales observed for other fluorescent proteins.[58,65,74,80] These results indicate that smURFP is potentially useful for imaging techniques that require a molecule that shows fast blinking behavior, such as super-resolution techniques. The apparent absence of dark state conversion in miRFP670 and higher photostability compared to smURFP, mCherry, and TagRFP-T[65] indicate that this is a useful protein to use for deep-tissue experiments.

4.8 Conclusion

In this chapter I reported the results from measurements of the dark state photophysics of two near-infrared fluorescent proteins that had not previously been chracterized. I found that miRFP670 exhibited no dark state conversion over the irradiance range measured, and smURFP exhibited dark state photoswitching on timescales ranging from tens to hundreds of microseconds. This timescale is consistent with other fluorescent proteins for which the dark-state photophysics has been characterized, and is the first time dark state conversion rates have been measured in near-infrared fluorescent proteins. While the exponential fits shown here can be used to extract rate constants for ground-state recovery, at the excitation rate used the dark state conversion rate constants cannot be determined and could only be estimated from simulated data. These measurements can be used to illuminate the photophysical properties of the near-infrared fluorescent proteins, but complementary measurements such as single-molecule measurements are needed to fully characterize the dark-state dynamics of smURFP.

4.9 Future Directions

Further experiments should look at lower irradiances (100 W/cm^2 and below) to give better predictions of blinking behavior under conditions more relevant to wide-field imaging. Expanding the range of irradiances used would give more insight into for which imaging experiments these proteins are best applied. Single-molecule measurements of

smURFP should also be done to compare the predicted on- and off- times to the ensemble studies described here.

Other experiments needed are dark state measurements on miRFP670 mutants with mutations designed disrupt the hydrogen bonding interactions around both ring A and ring D. This would help determine whether motions of the biliverdin A- or D-ring are responsible for the dark state conversion observed in smURFP. Dark state photophysical measurements on such proteins would yield insight into the mechanism behind dark state conversion in smURFP and possibly hindering it in miRFP670.

Bibliography

1. Shimomura, O., Johnson, F. H. & Saiga, Y. Extraction, Purification and Properties of Aequorin, a Bioluminescent Protein from the Luminous Hydromedusan, Aequorea. *J. Cell. Comp. Physiol.* **59**, 223–239 (1962).

2. Shimomura, O. Structure of the chromophore of Aequorea green fluorescent protein. *FEBS Lett.* **104**, 220–222 (1979).

3. Prasher, D. C., Eckenrode, V. K., Ward, W. W., Prendergast, F. G. & Cormier, M. J. Primary structure of the Aequorea victoria green-fluorescent protein. *Gene* **111**, 229–233 (1992).

4. Cody, C. W., Prasher, D. C., Westler, W. M., Prendergast, F. G. & Ward, W. W. Chemical structure of the hexapeptide chromophore of the Aequorea green-fluorescent protein. *Biochemistry* **32**, 1212–1218 (1993).

5. Reid, B. G. & Flynn, G. C. *Chromophore Formation in Green Fluorescent Protein*. *Biochemistry* **111**, (1992).
6. Chalfie, M., Tu, Y., Euskirchen, G., Ward, W. W. & Prasher, D. C. Green fluorescent protein as a marker for gene expression. *Science* **263**, 802–5 (1994).

7. Heim, R., Prasher, D. C. & Tsien, R. Y. Wavelength mutations and posttranslational autoxidation of green fluorescent protein. *Proc. Natl. Acad. Sci. U. S. A.* **91**, 12501–4 (1994).

8. Heim, R., Cubitt, A. B. & Tsien, R. Y. Improved green fluorescence. *Nature* **373,** 663–664 (1995).

9. Heim, R. & Tsien, R. Y. Engineering green fluorescent protein for improved brightness, longer wavelengths and fluorescence resonance energy transfer. *Curr. Biol.* **6**, 178–182 (1996).

10. Gross, L. A., Baird, G. S., Hoffman, R. C., Baldridge, K. K. & Tsien, R. Y. The structure of the chromophore within DsRed, a red fluorescent protein from coral. *Proc. Natl. Acad. Sci. U. S. A.* **97**, 11990–11995 (2000).

11. Matz, M. V. *et al.* Fluorescent proteins from nonbioluminescent Anthozoa species. *Nat. Biotechnol.* **17**, 969–973 (1999).

12. Henderson, J. N. & Remington, S. J. Crystal structures and mutational analysis of amFP486, a cyan flourescent protein from Anemonia majano. *Proc. Natl. Acad. Sci. U. S. A.* **102**, 12712–12717 (2005).
13. Remington, S. J. et al. zFP538, a yellow-fluorescent protein from Zoanthus, contains a novel three-ring chromophore. *Biochemistry* **44**, 202–212 (2005).

14. Wachter, R. M., Elsliger, M. A., Kallio, K., Hanson, G. T. & Remington, S. J. Structural basis of spectral shifts in the yellow-emission variants of green fluorescent protein. *Structure* **6**, 1267–1277 (1998).

15. Ormö, M. *et al.* Crystal structure of the Aequorea victoria green fluorescent protein. *Science* **273**, 1392–5 (1996).

16. Petersen, J. et al. The 2.0-Å Crystal Structure of eqFP611, a Far Red Fluorescent Protein from the Sea Anemone Entacmaea quadricolor. *J. Biol. Chem.* **278**, 44626–44631 (2003).

17. Campbell, R. E. *et al.* A monomeric red fluorescent protein. *Proc. Natl. Acad. Sci.* **99**, 7877–7882 (2002).

18. Shaner, N. C. et al. Improved monomeric red, orange and yellow fluorescent proteins derived from Discosoma sp. red fluorescent protein. *Nat. Biotechnol.* **22**, 1567–1572 (2004).

19. Shu, X., Shaner, N. C., Yarbrough, C. A., Tsien, R. Y. & Remington, S. J. Novel chromophores and buried charges control color in mFruits. *Biochemistry* **45**, 9639–9647 (2006).

20. Siegel, A. P., Baird, M. A., Davidson, M. W. & Day, R. N. Strengths and weaknesses of recently engineered red fluorescent proteins evaluated in live cells using fluorescence correlation spectroscopy. *Int. J. Mol. Sci.* **14,** 20340–58 (2013).

21. Strack, R. L. et al. A rapidly maturing far-red derivative of DsRed-Express2 for whole-cell labeling. *Biochemistry* **48**, 8279–8281 (2009).

22. Zaccolo, M. *et al.* A genetically encoded, fluorescent indicator for cyclic AMP in living cells. *Nat. Cell Biol.* **2**, 25–29 (2000).

23. Wang, A., Feng, J., Li, Y. & Zou, P. Beyond Fluorescent Proteins: Hybrid and Bioluminescent Indicators for Imaging Neural Activities. ACS Chem. Neurosci. 9, 639–650 (2018).

24. Shcherbo, D. et al. Near-infrared fluorescent proteins. *Nat. Methods* **7**, 827–829 (2010).

25. Moron, V., Marazzi, M. & Wanko, M. Far Red Fluorescent Proteins: Where Is the Limit of the Acylimine Chromophore? *J. Chem. Theory Comput.* **15**, 4228–4240 (2019).

26. Miyawaki, A., Griesbeck, O., Heim, R. & Tsien, R. Y. Dynamic and quantitative Ca2+ measurements using improved cameleons. *Proc. Natl. Acad. Sci. U. S. A.* **96**, 2135–40 (1999).

27. Walia, A., Waadt, R. & Jones, A. M. Genetically Encoded Biosensors in Plants: Pathways to Discovery. *Annu. Rev. Plant Biol.* **69**, 497–524 (2018).

28. Wang, A., Feng, J., Li, Y. & Zou, P. Beyond Fluorescent Proteins: Hybrid and Bioluminescent Indicators for Imaging Neural Activities. ACS Chem. Neurosci. 9, 639–650 (2018).

29. Miyawaki, A. et al. Fluorescent indicators for Ca2+based on green fluorescent proteins and calmodulin. *Nature* **388,** 882–887 (1997).

30. Zaccolo, M. *et al.* A genetically encoded, fluorescent indicator for cyclic AMP in living cells. *Nat. Cell Biol.* **2**, 25–29 (2000).

31. Weissleder, R. & Ntziachristos, V. Shedding light onto live molecular targets. *Nat. Med.* **9**, 123–128 (2003).

32. Richards-Kortum, R. & Sevick-Muraca, E. Quantitative Optical Spectroscopy for Tissue Diagnosis. *Annu. Rev. Phys. Chem.* **47**, 555–606 (1996).

33. Auldridge, M. E. & Forest, K. T. Bacterial phytochromes: More than meets the light. *Crit. Rev. Biochem. Mol. Biol.* **46**, 67–88 (2011).

34. Shcherbakova, D. M. & Verkhusha, V. V. Near-infrared fluorescent proteins for multicolor in vivo imaging. *Nat. Methods* **10**, 751–754 (2013).

35. Giraud, E. & Verméglio, A. Bacteriophytochromes in anoxygenic photosynthetic bacteria. *Photosynthesis Research* **97**, 141–153 (2008).

36. Wagner, J. R., Brunzelle, J. S., Forest, K. T. & Vierstra, R. D. A light-sensing knot revealed by the structure of the chromophore-binding domain of phytochrome. *Nature* **438**, 325–331 (2005).

37. Rodriguez, E. A. *et al.* A far-red fluorescent protein evolved from a cyanobacterial phycobiliprotein. *Nat. Methods* **13**, 763–769 (2016).

38. Bhattacharya, S., Auldridge, M. E., Lehtivuori, H., Ihalainen, J. A. & Forest, K. T. Origins of fluorescence in evolved bacteriophytochromes. *J. Biol. Chem.* **289**, 32144–52 (2014).

39. Bhattacharya, S., Auldridge, M. E., Lehtivuori, H., Ihalainen, J. A. & Forest, K. T. Origins of fluorescence in evolved bacteriophytochromes. *J. Biol. Chem.* **289**, 32144–52 (2014).

40. Braslavsky, S. E., Holzwarth, A. R. & Schaffner, K. Solution Conformations, Photophysics, and Photochemistry of Bile Pigments; Bilirubin and Biliverdin, Dimethyl Esters and Related Linear Tetrapyrroles. *Angew. Chemie Int. Ed. English* **22**, 656–674 (1983).

41. Shu, X. *et al.* Mammalian Expression of Infrared Fluorescent Proteins Engineered from a Bacterial Phytochrome. *Science* **324**, 804–807 (2009).

42. Yu, D. *et al.* An improved monomeric infrared fluorescent protein for neuronal and tumour brain imaging. *Nat. Commun.* **5**, 3626 (2014).

43. Yu, D. *et al.* A naturally monomeric infrared fluorescent protein for protein labeling in vivo. *Nat. Methods* **12**, 763–765 (2015).

44. Filonov, G. S. et al. Bright and stable near-infrared fluorescent protein for in vivo imaging. *Nat. Biotechnol.* **29**, 757–761 (2011).

45. Piatkevich, K. D. et al. Near-Infrared Fluorescent Proteins Engineered from Bacterial Phytochromes in Neuroimaging. *Biophys. J.* **113**, 2299–2309 (2017).

46. Shcherbakova, D. M. *et al.* Bright monomeric near-infrared fluorescent proteins as tags and biosensors for multiscale imaging. *Nat. Commun.* **7**, 12405 (2016)

47. Rodriguez, E. A. *et al.* A far-red fluorescent protein evolved from a cyanobacterial phycobiliprotein. *Nat. Methods* **13**, 763–769 (2016).

48. Yeh, S. W., Ong, L. J., Glazer, A. N. & Clark, J. H. Fluorescence properties of allophycocyanin and a crosslinked allophycocyanin trimer. *Cytometry* **8**, 91–95 (1987).

49. Berns, D. S. & MacColl, R. Phycocyanin in Physical–Chemical Studies. *Chem. Rev.* **89**, 807–825 (1989).

50. Li, X. D. *et al.* Design of small monomeric and highly bright near-infrared fluorescent proteins. *Biochim. Biophys. Acta - Mol. Cell Res.* **1866**, 1608–1617 (2019).

51. Lakowicz, J. R. *Principles of fluorescence spectroscopy*. (Springer, 2006). doi:10.1007/978-0-387-46312-4

52. Chudakov, D. M., Matz, M. V., Lukyanov, S. & Lukyanov, K. A. Fluorescent proteins and their applications in imaging living cells and tissues. *Physiological Reviews* **90**, 1103–1163 (2010).

53. Rodriguez, E. A. *et al.* The Growing and Glowing Toolbox of Fluorescent and Photoactive Proteins. *Trends in Biochemical Sciences* **42**, 111–129 (2017).

54. Shcherbakova, D. M., Baloban, M. & Verkhusha, V. V. Near-infrared fluorescent proteins engineered from bacterial phytochromes. *Current Opinion in Chemical Biology* **27**, 52–63 (2015).

55. Shcherbakova, D. M., Shemetov, A. A., Kaberniuk, A. A. & Verkhusha, V. V. Natural Photoreceptors as a Source of Fluorescent Proteins, Biosensors, and Optogenetic Tools. *Annu. Rev. Biochem.* **84**, 519–550 (2015).

56. Lehtivuori, H. *et al.* Fluorescence properties of the chromophore-binding domain of bacteriophytochrome from Deinococcus radiodurans. *J. Phys. Chem. B* **117**, 11049–11057 (2013).

57. Wagner, J. R. *et al.* Mutational analysis of Deinococcus radiodurans bacteriophytochrome reveals key amino acids necessary for the photochromicity and proton exchange cycle of phytochromes. *J. Biol. Chem.* **283**, 12212–12226 (2008).

58. Dean, K. M. et al. Analysis of red-fluorescent proteins provides insight into dark-state conversion and photodegradation. *Biophys. J.* **101**, 961–969 (2011).

59. Soper, S. A., Nutter, H. L., Keller, R. A., Davis, L. M. & Shera, E. B. The Photophysical Constants of Several Fluorescent Dyes Pertaining to Ultrasensitive Fluorescence Spectroscopy. *Photochem. Photobiol.* **57**, 972–977 (1993).

60. Eggeling, C., Widengren, J., Rigler, R. & Seidel, C. A. M. Photobleaching of Fluorescent Dyes under Conditions Used for Single-Molecule Detection: Evidence of Two-Step Photolysis. *Anal. Chem.* **70**, 2651–2659 (1998).

61. Eggeling, C., Volkmer, A. & Seidel, C. A. M. Molecular Photobleaching Kinetics of Rhodamine 6G by One- and Two-Photon Induced Confocal Fluorescence Microscopy. *ChemPhysChem* **6**, 791–804 (2005).

62. Harms, G. S., Cognet, L., Lommerse, P. H. M., Blab, G. A. & Schmidt, T. Autofluorescent proteins in single-molecule research: Applications to live cell imaging microscopy. *Biophys. J.* **80**, 2396–2408 (2001).

63. Veettil, S., Budisa, N. & Jung, G. Photostability of green and yellow fluorescent proteins with fluorinated chromophores, investigated by fluorescence correlation spectroscopy. *Biophys. Chem.* **136**, 38–43 (2008).

64. Hinkeldey, B., Schmitt, A. & Jung, G. Comparative Photostability Studies of BODIPY and Fluorescein Dyes by Using Fluorescence Correlation Spectroscopy. *ChemPhysChem* **9**, 2019–2027 (2008).

65. Manna, P. & Jimenez, R. Time and Frequency-Domain Measurement of Ground-State Recovery Times in Red Fluorescent Proteins. *J. Phys. Chem. B* **119**, 4944–4954 (2015).

66. Schenk, A., Ivanchenko, S., Röcker, C., Wiedenmann, J. & Nienhaus, G. U. Photodynamics of Red Fluorescent Proteins Studied by Fluorescence Correlation Spectroscopy. *Biophys. J.* **86,** 384–394 (2004).

67. Mo, G. C. H. et al. Genetically encoded biosensors for visualizing live-cell biochemical activity at super-resolution. Nat. Methods 14, 427–434 (2017).

68. Dickson, R. M., Cubitt, A. B., Tsien, R. Y. & Moerner, W. E. On/off blinking and switching behaviour of single molecules of green fluorescent protein. *Nature* **388**, 355–358 (1997).

69. Sinnecker, D., Voigt, P., Hellwig, N. & Schaefer, M. Reversible photobleaching of enhanced green fluorescent proteins. *Biochemistry* **44**, 7085–7097 (2005).

70. Prangsma, J. C. *et al.* Quantitative Determination of Dark Chromophore Population Explains the Apparent Low Quantum Yield of Red Fluorescent Proteins. *J. Phys. Chem. B* (2020). doi:10.1021/acs.jpcb.9b10396

71. Adam, V. *et al.* Structural basis of X-ray-induced transient photobleaching in a photoactivatable green fluorescent protein. *J. Am. Chem. Soc.* **131**, 18063–18065 (2009).

72. Roy, A., Field, M. J., Adam, V. & Bourgeois, D. The nature of transient dark states in a photoactivatable fluorescent protein. *J. Am. Chem. Soc.* **133**, 18586–18589 (2011).

73. Berardozzi, R., Adam, V., Martins, A. & Bourgeois, D. Arginine 66 Controls Dark-State Formation in Green-to-Red Photoconvertible Fluorescent Proteins. *J. Am. Chem. Soc.* **138,** 558–565 (2016).

74. Heikal, A. A., Hess, S. T., Baird, G. S., Tsien, R. Y. & Webb, W. W. Molecular spectroscopy and dynamics of intrinsically fluorescent proteins: coral red (dsRed) and yellow (Citrine). *Proc. Natl. Acad. Sci. U. S. A.* **97**, 11996–2001 (2000).

75. Schwille, P., Kummer, S., Heikal, A. A., Moerner, W. E. & Webb, W. W. Fluorescence correlation spectroscopy reveals fast optical excitation-driven intramolecular dynamics of yellow fluorescent proteins. *Proc. Natl. Acad. Sci. U. S. A.* **97,** 151–6 (2000).

76. Haupts, U., Maiti, S., Schwille, P. & Webb, W. W. Dynamics of fluorescence fluctuations in green fluorescent protein observed by fluorescence correlation spectroscopy. *Proc. Natl. Acad. Sci. U. S. A.* **95,** 13573–8 (1998).

77. Vegh, R. B. et al. Chromophore photoreduction in red fluorescent proteins is responsible for bleaching and phototoxicity. *J. Phys. Chem. B* **118**, 4527–4534 (2014).

78. Annibale, P., Scarselli, M., Kodiyan, A. & Radenovic, A. Photoactivatable Fluorescent Protein mEos2 Displays Repeated Photoactivation after a Long-Lived Dark State in the Red Photoconverted Form. *J. Phys. Chem. Lett.* **1**, 1506–1510 (2010).

79. David, C. C. et al. Spectroscopic characterization of Venus at the single molecule level. *Photochem. Photobiol. Sci.* **11**, 358–363 (2012).

80. Malvezzi-Campeggi, F., Jahnz, M., Heinze, K. G., Dittrich, P. & Schwille, P. Light-induced flickering of DsRed provides evidence for distinct and interconvertible fluorescent states. *Biophys. J.* **81**, 1776–1785 (2001).

81. Baloban, M. *et al.* Designing brighter near-infrared fluorescent proteins: insights from structural and biochemical studies. *Chem. Sci.* **8**, 4546–4557 (2017).

82. Zhou, X. X. & Lin, M. Z. Photoswitchable fluorescent proteins: Ten years of colorful chemistry and exciting applications. *Current Opinion in Chemical Biology* **17**, 682–690 (2013).

83. Chen, Y.-C. & Dickson, R. M. Improved Fluorescent Protein Contrast and Discrimination by Optically Controlling Dark State Lifetimes. *J. Phys. Chem. Lett.* **8**, 733–736 (2017).

84. Mahoney, D. P. *et al.* Tailoring Cyanine Dark States for Improved Optically Modulated Fluorescence Recovery. *J. Phys. Chem. B* (2015). doi:10.1021/acs.jpcb.5b00777

85. Donnert, G., Eggeling, C. & Hell, S. W. Major signal increase in fluorescence microscopy through dark-state relaxation. *Nat. Methods* **4**, 81–86 (2007).

86. Jablonski, A. E. et al. Signal discrimination between fluorescent proteins in live cells by long-wavelength optical modulation. *J. Phys. Chem. Lett.* **3**, 3585–3591 (2012).

87. Abbe, E. Beiträge zur Theorie des Mikroskops und der mikroskopischen Wahrnehmung. *Arch. für Mikroskopische Anat.* **9**, 413–418 (1873).

88. Moerner, W. E. & Kador, L. Optical detection and spectroscopy of single molecules in a solid. *Phys. Rev. Lett.* **62**, 2535–2538 (1989).

89. Moerner, W. E. & Orrit, M. Illuminating single molecules in condensed matter. *Science* **283**, 1670–6 (1999).

90. Hell, S. W. & Wichmann, J. Breaking the diffraction resolution limit by stimulated emission: stimulated-emission-depletion fluorescence microscopy. *Opt. Lett.* **19**, 780 (1994).

91. Klar, T. A., Jakobs, S., Dyba, M., Egner, A. & Hell, S. W. Fluorescence microscopy with diffraction resolution barrier broken by stimulated emission. *Proc. Natl. Acad. Sci. U. S. A.* **97**, 8206–10 (2000).

92. Hell, S. W. & Kroug, M. Ground-state-depletion fluorescence microscopy: A concept for breaking the diffraction resolution limit. *Appl. Phys. B Lasers Opt*. **60**, 495–497 (1995).

93. Hofmann, M., Eggeling, C., Jakobs, S. & Hell, S. W. Breaking the diffraction barrier in fluorescence microscopy at low light intensities by using reversibly photoswitchable proteins. *Proc. Natl. Acad. Sci.* **102**, 17565–17569 (2005).

94. Betzig, E. *et al.* Imaging intracellular fluorescent proteins at nanometer resolution. *Science* **313**, 1642–5 (2006).

95. Rust, M. J., Bates, M. & Zhuang, X. Sub-diffraction-limit imaging by stochastic optical reconstruction microscopy (STORM). *Nat. Methods* **3**, 793–796 (2006).

96. Dertinger, T., Colyer, R., Iyer, G., Weiss, S. & Enderlein, J. Fast, background-free, 3D super-resolution optical fluctuation imaging (SOFI). *Proc. Natl. Acad. Sci. U. S. A.* **106**, 22287–92 (2009).

97. Potma, E. O. *et al.* Reduced protein diffusion rate by cytoskeleton in vegetative and polarized Dictyostelium cells. *Biophys. J.* **81**, 2010–2019 (2001).

98. Patterson, G. H., Knobel, S. M., Sharif, W. D., Kain, S. R. & Piston, D. W. Use of the green fluorescent protein and its mutants in quantitative fluorescence microscopy. *Biophys. J.* **73**, 2782–90 (1997).

99. Rizzo, M. A., Springer, G. H., Granada, B. & Piston, D. W. An improved cyan fluorescent protein variant useful for FRET. *Nat. Biotechnol.* **22**, 445–449 (2004).

100. Kremers, G.-J., Goedhart, J., Van Munster, E. B. & Gadella, T. W. J. Cyan and Yellow Super Fluorescent Proteins with Improved Brightness, Protein Folding, and FRET Förster Radius †, ‡. (2006). doi:10.1021/bi0516273

101. Kremers, G. J. & Piston, D. Photoconversion of purified fluorescent proteins and dual-probe optical highlighting in live cells. *J. Vis. Exp.* 1995 (2010). doi:10.3791/1995

102. Cranfill, P. J. *et al.* Quantitative assessment of fluorescent proteins. *Nat. Methods* **13**, 557–562 (2016).

103. Rondelez, Y. *et al.* Microfabricated arrays of femtoliter chambers allow single molecule enzymology. *Nat. Biotechnol.* **23**, 361–365 (2005).

104. Murphy, T. W., Zhang, Q., Naler, L. B., Ma, S. & Lu, C. Recent advances in the use of microfluidic technologies for single cell analysis. *Analyst* **143**, 60–80 (2018).

105. Henley, W. H., Dennis, P. J. & Ramsey, J. M. Fabrication of Microfluidic Devices Containing Patterned Microwell Arrays. *Anal. Chem.* **84**, 1776–1780 (2012).

106. Qin, Y. *et al.* Direct Comparison of a Genetically Encoded Sensor and Small Molecule Indicator: Implications for Quantification of Cytosolic Zn^{2+}. *ACS Chem. Biol.* **8**, 2366–2371 (2013).

107. Processing Guidelines for SU-8 2025-2075 (2019). Available at: https://kayakuam.com/wp-content/uploads/2019/09/SU-82000DataSheet2025thru2075Ver4.pdf.

108. Processing Guidelines for SU-8 3000 (2019). Available at: https://kayakuam.com/wp-content/uploads/2019/09/SU-8-3000-Data-Sheet.pdf

109. Ling, Z. G., Lian, K. & Jian, L. Improved patterning quality of SU-8 microstructures by optimizing the exposure parameters. in *Advances in Resist Technology and Processing XVII* (ed. Houlihan, F. M.) **3999**, 1019 (2000).

110. Liu, J., Zhu, J., Ding, G., Zhao, X. & Cai, B. Orthogonal method for processing of SU-8 resist in UV-LIGA. in *Micromachining and Microfabrication Process Technology VII* (eds. Karam, J. M. & Yasaitis, J. A.) **4557**, 462–466 (2001).

111. Wouters, K. & Puers, R. Accurate measurement of the steady-state swelling behavior of SU-8 negative photo resist. in *Procedia Chemistry* **1**, 60–63 (2009).

112. Grubbs, F. E. Procedures for Detecting Outlying Observations in Samples. Technometrics 11, 1–21 (1969).

113. Ferguson, T. S. Rules for Rejection of Outliers. *Rev. l'Institut Int. Stat. / Rev. Int. Stat. Inst.* **29**, 29-43 (1961).

114. Aggarwal, C. C. Outlier Analysis. (Springer International Publishing, 2017). doi:10.1007/978-3-319-47578-3

115. Barnett, V. & Lewis, T. *Outliers in statistical data*. (Wiley, 1994).

116. Anscombe, F. J. & Glynn, W. J. Distribution of the Kurtosis Statistic b_2 for Normal Samples. *Biometrika* **70**, 227-234 (1983).

117. Yang, X., Kuk, J. & Moffat, K. Crystal structure of Pseudomonas aeruginosa bacteriophytochrome: Photoconversion and signal transduction. *Proc. Natl. Acad. Sci. U. S. A.* **105**, 14715–14720 (2008).

118. Hontani, Y. et al. Bright blue-shifted fluorescent proteins with Cys in the GAF domain engineered from bacterial phytochromes: fluorescence mechanisms and excited-state dynamics. Sci. Rep. 6, 37362 (2016).

119. Zhu, J., Shcherbakova, D. M., Hontani, Y., Verkhusha, V. V. & Kennis, J. T. M. Ultrafast excited-state dynamics and fluorescence deactivation of near-infrared fluorescent proteins engineered from bacteriophytochromes. *Sci. Rep.* **5**, 12840 (2015).

120. Yang, X., Stojković, E. A., Kuk, J. & Moffat, K. Crystal structure of the chromophore binding domain of an unusual bacteriophytochrome, RpBphP3, reveals residues that modulate photoconversion. *Proc. Natl. Acad. Sci. U. S. A.* **104**, 12571–12576 (2007).

121. Lamparter, T. *et al.* Biliverdin Binds Covalently to Agrobacterium Phytochrome Agp1 via Its Ring A Vinyl Side Chain. *J. Biol. Chem.* **278**, 33786–33792 (2003).

122. Wagner, J. R., Zhang, J., Brunzelle, J. S., Vierstra, R. D. & Forest, K. T. High resolution structure of Deinococcus bacteriophytochrome yields new insights into phytochrome architecture and evolution. *J. Biol. Chem.* **282**, 12298–12309 (2007).

123. Velazquez Escobar, F. *et al.* Structural parameters controlling the fluorescence properties of phytochromes. *Biochemistry* **53**, 20–29 (2014).

124. Toh, K. C., Stojkovic, E. A., van Stokkum, I. H. M., Moffat, K. & Kennis, J. T. M. Proton-transfer and hydrogen-bond interactions determine fluorescence quantum yield and photochemical efficiency of bacteriophytochrome. *Proc. Natl. Acad. Sci. U. S. A.* **107**, 9170–5 (2010).

125. Toh, K. C., Stojković, E. A., Van Stokkum, I. H. M., Moffat, K. & Kennis, J. T. M. Fluorescence quantum yield and photochemistry of bacteriophytochrome constructs. *Phys. Chem. Chem. Phys.* **13**, 11985–11997 (2011).

126. Nieder, J. B. *et al.* Pigment-protein interactions in phytochromes probed by fluorescence line narrowing spectroscopy. *J. Phys. Chem. B* **117**, 14940–14950 (2013).

127. Toh, K. C. *et al.* Primary Reactions of Bacteriophytochrome Observed with Ultrafast Mid-Infrared Spectroscopy. *J. Phys. Chem. A* **115**, 3778–3786 (2011).

128. Altoé, P. et al. Deciphering intrinsic deactivation/isomerization routes in a phytochrome chromophore model. J. Phys. Chem. B 113, 15067–15073 (2009).

129. Fuenzalida-Werner, J. P. *et al.* Crystal structure of a biliverdin-bound phycobiliprotein: Interdependence of oligomerization and chromophorylation. *J. Struct. Biol.* **204**, 519–522 (2018).

Appendix A: Steady State Fluorescence Measurements

A.1 Publication Status

This section discusses the work done in preparing Figure S6 for the following publication:

Konold, P. E., Yoon, E., Lee, J., Allen, S. L., Chapagain, P. P., Gerstman, B. S., Regmi, C. K., Piatkevich, K. D., Verkhusha, V. V., Joo, T., Jimenez, R. Fluorescence from Multiple Chromophore Hydrogen-Bonding States in the Far-Red Protein TagRFP675. *J. Phys. Chem. Lett.* **7**, 3046–3051 (2016).

A.2 Introduction

This work was done as part of an investigation into TagRFP675 hydrogen-bonding between the *N*-acylimine carbonyl and the Q41 side chain. While other studies have associated the large Stokes shift observed in TagRFP675 with this and other hydrogen bonds, the mechanism required further investigation. This investigation used spectrally resolved transient grating (SRTG) and femtosecond time-resolved fluorescence spectra (TRFS) measurements in addition to MD simulations to characterize the excited-state dynamics of TagRFP675.

The Q41 interaction was investigated in part by generating mKate/M41Q and TagRFP675/Q41M, to add glutamine, which has a polar side chain, into mKate and remove it from TagRFP675 by replacing it with methionine, an amino acid with a hydrophobic side chain. SRTG measurements on TagRFP675 and mKate/M41 showed that peak-shifts in the stimulated emission spectral response suggested the presence of multiple spectral forms. Time-resolved area-normalized spectra (TRANES) generated from TRFS measurements supported the existence of multiple discrete emitting states.[106] In this section I discuss steady-state fluorescence measurements on TagRFP675 and mKate/M41Q that were done to provide additional information on the existence of multiple ground states.

A.3 Methods

The fluorescent proteins TagRFP675 and mKate/M41Q were prepared in 15 mM Tris, 100 mM KCl, pH 8.0 buffer. The fluorescence spectra were collected using a QM-6 steady-state spectrofluorimeter from Photon Technology International (PTI). The excitation and emission slits were opened to 0.5 mm for a 2 nm bandwidth, and the PMT voltage was set to 1000. The step size was set to 0.25 nm.

A.4 Results

The results of the steady-state fluorescence measurements on TagRFP675 and mKate/M41Q are shown in Figure A.1 below.

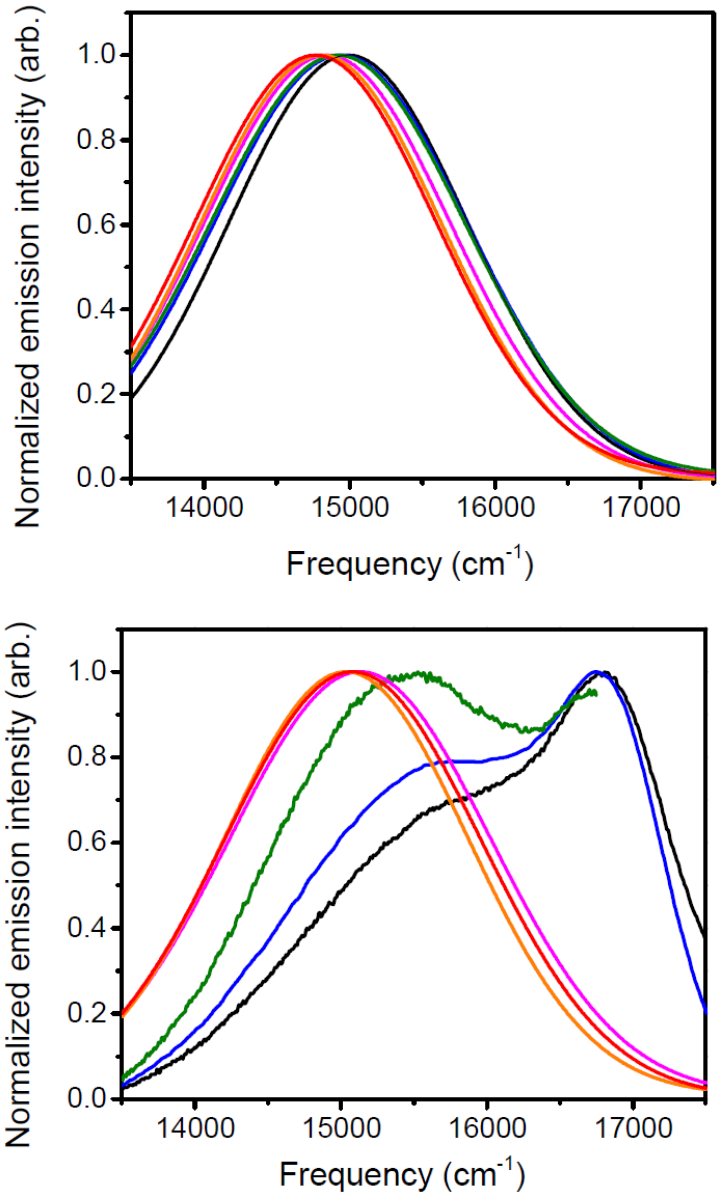

Figure A.1 Excitation-dependent emission spectra. (top) TagRFP675 (bottom) mKate/M41Q. For both plots, the colors correspond to excitation at red-15310 cm-1, orange-15850 cm-1, magenta-16420 cm-1, green- 17040 cm-1, blue- 18050 cm-1, and black- 19190 cm-1.

Figure A.1 shows variation in emission peak wavelength as excitation wavelength is altered. These results support the claim that there are multiple ground states for these two proteins. From these results in combination with other

measurements, the hydrogen-bonding interactions with the Q41 position in TagRFP675 and mKate/M41Q leads to a heterogenous system with multiple emitting forms.

Appendix B: Detailed Protocols

B.1 Microfluidic Master Fabrication

Microwell masters are the molds that are used to produce PDMS microwell deices. Master fabrication takes two days and once generated the masters can be used many times to generate microwell devices.

B.1. 1 Selecting materials and Design

Master templates are designed using computer-aided design (CAD) software such as AutoCAD. The photolithography mask with the design is printed with the specification that the emulsion side is down. It is a good idea to order a few variations on the same design to troubleshoot. Silicon wafers with 76.2 mm diameter are used as a substrate to deposit photoresist. The SU-8 photoresist is selected based on desired photoresist thickness, and the 3000 series is recommended for its improved adhesion properties. Datasheets are available on the Microchem website for guidance (http://microchem.com/Prod-SU8_KMPR.htm). Initial trials for microwells were done using SU-8 2025 for 25 µm

photoresist thickness. Later fabrications used SU-3025 for the same thickness due to the improved adhesion properties of the SU-8 3000 series.

B.1.2 Wafer Cleaning

If a used wafer has a layer of cross-linked SU-8 it should be submerged in piranha solution for at least 30 minutes between 90-100 °C to remove the photoresist. Piranha should never be left unattended while heating. After, rinse with isopropanol and dry with N_2. All used wafers should be ashed in the reactive ion etcher (RIE) prior to use. This will remove a few microns from the surface. The RIE setting for this step is pure O_2 with 30 sccm and 300 W for 5 minutes. The RIE can be purged before use by running the program once with nothing in the chamber.

The next cleaning step is optional but recommended for new wafers. The wafer is rinsed with acetone and then submerged in a dish containing acetone and swished for 5 minutes. The wafer is then rinsed with methanol and then submerged in a dish containing methanol and swished for 2 minutes. It is then rinsed for ~10 seconds with isopropanol and thoroughly dried with pressurized N_2 and placed on a hot plate at 70 °C for 10 minutes to evaporate any remaining solvent.

B.1.3 Spin-Coating the Wafer

The wafers are next spin-coated with SU-8, a negative epoxy type photoresist. The clean wafer is centered on the spin coater and the vacuum is

engaged. Failing to center the wafer may lead to an uneven spin coat. A few milliliters of photoresist is carefully poured on the wafer. Adding too much will lead to beading on the edge of the wafer. A 2-step spin coat process is used, with an initial 500 rpm/s step followed by a higher speed step determined from desired photoresist thickness. Data for spin speeds for specific photoresists and resulting thickness is given on the datasheets found on the Microchem website (http://microchem.com/Prod-SU8_KMPR.htm).

Procedure 7 in the Keck Lab spin-coater protocol list corresponds to a 2-step process that can be slightly modified based on the desired spin settings. The procedure used for microwell masters with SU-8 3025 and 25 µm photoresist thickness is first a 500 rpm step for 10 seconds with 100 rpm/s acceleration followed by 3000 rpm for 30 seconds with 300 rpm/s acceleration.

Thickness of the spin coat can be adjusted by altering the viscosity of the photoresist during the spin coat by heating the photoresist or the wafer immediately before spin-coating. Centrifuging photoresist prior to pouring it can reduce the number of air bubbles compared to resist straight from the bottle. If many wafers are being spin-coated at once, the spin coat chamber should be cleaned after a few wafers have been spin-coated. Otherwise built up photoresist from previous spins may drip onto the wafer.

B.1.4 Soft bake

After spin-coating, the wafer is soft baked on a hot plate to evaporate solvent. To improve adhesion of the microwell masters, a slow ramp was done for every heating step. The hot plate was set to increase the temperature at a rate of 5 °C/min. The wafers are placed on a hot plate at room temperature (~20 °C) and raised to 95 °C. The amount of time to soft bake is determined by the Microchem datasheet based on specific SU-8 type used and photoresist thickness. Once the hot plate reaches 85 °C the timer is started. After the time is up, the hot plate is ramped down and the wafer is removed from heat once it has cooled to 65°C. For the 25 µm thick features with SU-8 3025 a 15 minute soft bake was done. For improved adhesion, the ramp speed can be lowered further to 1-3 °C/min.

B.1.5 UV Exposure

UV exposure is used to generate the acid catalyst that promotes the cross-linking reaction. To do this the photolithography mask is placed on the spin-coated wafer with the emulsion side down. The emulsion side will have acetate bubbles when viewed under a microscope and this orientation results in an image that is readable on the master (all letters, numbers correctly displayed). Arrange mask to avoid any bubbles or particles on the resist surface. The wafer is then placed on the UV mask aligner stage so that it fills the glass area. Both levers to the left of the machine should be pushed all the way away from the user. The stage should be raised by turning the stage knob counterclockwise until one of the levers

moves backward and the separation button lights up. At this point, the lever is pushed back and the contact button will light up. This ensures the wafer is in contact with the photolithography mask for uniform exposure. For small features in the center of the wafer deselect soft contact and use hard contact instead so that a burst of N_2 will push the chuck up for better contact. A single drop of glycerol can be placed between the wafer and the mask to improve contact. The wafer is now ready for UV exposure using the Karl Suss MJB3/MJB4.

The UV exposure settings are determined based on the mask aligner power measurement and the Microchem datasheet for the SU-8 photoresist selected and feature thickness. The SU-8 3025 is i-line sensitive and recommends 150-250 mJ/cm^2 exposure for 25 µm feature thickness. The i-line power of the UV contact aligner is 9.5 mW/cm^2 based on the most recent power measurement. Based on this information, a range of 16 s-26 seconds is recommended for exposure times. If a wafer is under-exposed, this will appear as cracks on the inside of the area exposed by the photolithography mask as not enough exposure energy was used to crosslink the entire exposure area. If a wafer is over-exposed, it will appear as reacted photoresist outside the area exposed by the photolithography mask, leading to cracks on the outside of the design. If good contact is not achieved between the photolithography mask and the spin-coated wafer, this will appear as exposure in the area outside of the area exposed by the photolithography mask. Adding a few drops of glycerol to the soft baked photoresist before adding the photolithography mask will improve the contact.

With 16 seconds of UV exposure, the design was slightly underexposed but over half of the microwells stuck to the substrate and were not washed away. With 18 seconds of UV exposure, all of the microwells appear to have stuck and all other features are formed, with a few cracks indicating slight underexposure. These cracks will likely be smoothed out during the hard bake step. A later repeat of the procedure found that 20-22 s of exposure produced even better results with no apparent under or overexposure.

B.1.6 Post-Exposure Bake

The post-exposure bake step will initiate the cross-linking reaction in the presence of the acid catalyst. Following UV exposure, the wafer is placed on a hot plate at room temperature. The heat is slowly ramped up to 95 °C at a rate of 5 °C/min. Once the temperature reaches 85 °C, the timer is started, similar to the soft bake step. The amount of time the device spends on the hot plate is determined from the Microchem datasheet for the selected SU-8 and for the photoresist thickness. For SU-8 3025 and 25 µm feature thickness, the post-exposure bake time is 5 minutes. After the time is up, the hot plate is slowly ramped down and the wafer is removed from the hot plate once it has cooled to 65 °C.

The latent image should begin to appear after a few minutes of heating. If it appears more quickly, the photoresist has likely been overexposed Exposure levels can be assessed during the post-exposure bake step. If the design takes longer to appear, this is a sign of under-exposure. Typically, the design will appear

after a few minutes of heating above 50 °C. Paying attention to this step when developing a protocol for a new design can save time on future steps by assessing whether the procedure worked as intended or not before continuing. After this step the cross-linked photoresist should be observed under a microscope to assess whether it has been underexposed or overexposed. This assessment may not be possible later if the design washes away in the development step.

B.1.7 Development

Once the wafer is at room temperature, it is submerged in fresh SU-8 developer Propylene glycol methyl ether acetate or PGMEA) to rinse any unreacted photoresist. The development time is found on the Microchem data sheet for the SU-8 type selected and feature thickness. For SU-8 3025 and 25 µm feature thickness, the development time selected was 8 minutes. For the first 3 minutes, the wafer is submerged with no agitation. For the final 5 minutes, the wafer is very gently swished in the developer. After this period the wafer is rinsed with fresh SU-8 developer for ~10 seconds (~10 mL developer). The wafer is then rinsed for ~ 10 seconds with isopropanol. The wafer is then carefully dried with N_2.

If a white residue appears on the wafer following development, this means that some unreacted photoresist remains on the wafer. In this case, the wafer should be submerged in the developer and swished for an additional 30-60 s to remove the remaining photoresist. If the design is washed away at this step, that

indicates either underexposure, too short of a post-exposure bake, or that the swishing during development was too vigorous. The key to this step is rinsing vigorously enough to remove all unreacted photoresist, but gently enough that the crosslinked photoresist remains. After this stage the designs should be checked under a microscope to assess whether the process was successful. Slight cracks in the photoresist will be filled during the hard bake step.

B.1.8 Hard Bake

The hard bake step will smooth out cracks in the photoresist and improve adhesion between the wafer and the photoresist. The wafer is is heated overnight (>6 hrs) on a hot plate set between 150 °C – 200 °C. A slow ramp at a rate of 3 °C/min is done to reach this temperature and ensure the integrity of the design during heating. This step will reflow cross-linked SU-8 to smooth out minor cracks in the photoresist. The next day the temperature is ramped down to room temperature.

B.1.9 Silanization

The silanization step is necessary to passivate the surface of the wafer, improving hydrophilicity to improve the process of pulling PDMS off of the wafer. If this step is skipped the PDMS may be bonded to the wafer and impossible to

remove. Silanization is done in a vacuum chamber reserved for chlorosilane use. A few drops of (tridecafluoro-1,1,2,2,-tetrahydrooctyl)-1-trichlorosilane are placed on a low fiber paper towel and placed with the wafers under vacuum overnight (>6 hours). The vacuum is arranged so that the wafers are between the silanes and the vacuum source. If possible, a wafer that is not in use is placed in front to ensure the wafers are not directly exposed to silane solution and the wafers are faced away from the vacuum flow. This is the final step in master fabrication. Following this step the master is taped into a Petri dish and used as a mold for PDMS devices. The master can be reused several times to produce several rounds of device fabrication.

B.2 Preparation, Cleaning, and Storage of Microwell Devices

Microwell devices are prepared by pouring PDMS into a pre-made microwell master mold, cutting the devices out of PDMS, and cleaning the devices which are then stored in a low dust environment prior to use. Polydimethylsiloxane (PDMS) is prepared by mixing the pre-polymer and curing agent in a 10:1 ratio. After thoroughly mixing, several gas bubbles will appear. The mixture is degassed under vacuum for 30 minutes to remove the majority of the bubbles. The mixture is then poured over the microwell master in a Petri dish and again degassed under vacuum for an additional 30 minutes. The dish is then placed in an over pre-heated to 70 °C and left to cure overnight (>6 hrs). The oven is turned off and vented to cool before removing the dish from the oven. This

step is necessary to prevent the plastic Petri dish from deforming due to the rapid temperature change.

The devices are cut out of the PDMS in a cleanroom to prevent dust from blocking the small features. Tape is pressed against the devices on each side and quickly removed. This removes small pieces of PDMS generated from cutting out the devices. Any remaining debris is blown from the microwell master template and the device using N_2 air. The devices are rinsed with isopropanol for ~10 s. The devices are blown dry with N_2 air and placed on a hot plate set to 70 °C for 10 minutes to evaporate any remaining solvents. Devices can additionally be plasma cleaned, but care must be taken to not let the top of the device touch anything (even another clean device) after this step as it may become permanently bonded.

For device storage, a clean, sterile Petri dish is blown with N_2 air to remove any dust and devices are placed in one layer across the bottom, with microwells facing up. The Petri dish is taped closed and wrapped in aluminum foil. These precautions are taken to prevent dust from entering the container and blocking microwells during storage. The container is stored in a clean hood and is only opened in a clean environment. After a microwell is removed for use, the dish is immediately re-sealed. Microwell devices are not exposed to ambient air once they have been cut out. Containers holding them are only opened in the cleanroom or in a clean hood. Exposure to particles in the air increases the odds that some of the wells will be clogged.

B.3 Bacterial Transformation

Bacterial transformation is the process of introducing plasmid DNA into bacterial cells for the purposes of growing cells expressing fluorescent protein. This protein can be used for optical measurements, or used to start liquid culture for protein purification or DNA extraction. 50 µL of *E. coli* competent cells (Top10) are removed from the Ultralow freezer and thawed on ice. Competent cells have had membranes made porous to prepare for transformation. Plasmid DNA encoding the fluorescent protein of interest is also thawed over ice. The plasmid should be His-tagged and have the pBAD expression system under the araBAD promoter to be used according to the fluorescent protein expression protocol listed in section B.4. 1 µL of plasmid DNA is added to the *E. coli* cells. The tube is mixed by gently tapping and is left on ice for 20 minutes. This allows the DNA to settle onto the cell walls. A water bath is heated to 42 °C and an incubator is set to 37 °C for later steps.

After sitting on ice for 20 minutes the cells are heat shocked by placing them in the 42 °C water bath for 35 s. The cells are then returned to the ice bath for 2 minutes and lysogeny broth (LB) media is preheated in the water bath. 400 µL of preheated LB media is added to the cells and the sample is incubated at 37 °C, 225 rpm for one hour. During this time an LB agar plate with ampicillin and arabinose is preheated at 37 °C. Once the samples are done incubating, 30-100 µL of the transformation sample is added to the agar plate and spread until the solution is completely absorbed using a sterile loop. The plate is placed in an incubator at 37 °C overnight (~12 hours). After the plate is grown up with many colonies, it can be placed in the fridge at 4 °C to stop growth. Plates are discarded after a week.

B.4 Fluorescent Protein Expression, Purification, and Storage

To generate protein solution for fluorescence measurements, cells containing the protein must be grown, the protein must be produced by the cells (expression), and the protein must be extracted from the cells (purification). This section details the protocol to produce fluorescent protein using *E. coli* cells.

B.4.1 Expression

A plasmid encoding the fluorescent protein was transformed into *E. coli* (Top10) competent cells via the procedure described in section B.3. After the *E. coli* have been transformed with the plasmid and grown on a plate overnight, a single colony is selected with an inoculum loop. Colonies are only used from plates that are less than three days old. The colony is added to a 50 mL conical tube with 12 mL of lysogeny broth (LB) media containing ampicillin to generate a starter culture. This culture is incubated at 37 °C, 225 rpm overnight (12-14 hours).

While the culture grows overnight, 2XTY media is prepared and autoclaved. 2XTY is prepared by adding 3.1 g 2XTY to 100 mL nanopure water. The cap is loosened and the solution is autoclaved using the liquid program settings. Once the solution is cooled to 55 °C or lower, 100 µL ampicillin is added for an ampicillin concentration of 0.1 mg/mL. Overnight culture is diluted in 2XTY at a 1:100 dilution. If larger volumes of expression culture are needed the recipe can be scaled up.

1 mL of the overnight culture is added to 100 mL of the 2XTY solution in a 250 mL sterile Erlenmeyer flask and incubated for 2 hours at 37 °C, 225 rpm.

Expression is then started by adding 1 mL of arabinose stock solution (20% w/v) for an arabinose concentration of 0.2 %. The expression culture is incubated overnight (6-8 hours) at 37 °C, 225 rpm. The incubator heat is turned to 28 °C, with the incubator shaker still set to 225 rpm. After 24 hours at 28 °C, the culture is removed from the incubator. The culture is centrifuged for 20 minutes at 6000 rpm with a centrifuge pre-chilled to 4 °C. The supernatant is poured off and disposed of and the protein pellet is stored in the -30 °C freezer for later purification unless the culture will be used immediately.

B.4.2 Purification and Concentration

The first step of protein purification is cell lysis. The centrifuge is chilled to 4 °C while the lysis is prepared. The pellets are weighed, and the weight of an empty centrifuge tube is subtracted. 3 mL of bPER II (Bacterial Protein Extraction Reagent) is added per 1 g of pellet is measured and combined with 10 µL of EDTA-free protease inhibitor per mL of resuspended pellet. The protease inhibitor is necessary to prevent degradation of extracted proteins. The volume of resuspended pellet can be calculated from volume of bPER (mL) added to pellet weight (g). The mixture is added to the cell pellet and mixed to resuspend. The resuspended cell mixture is added to a 50 mL conical tube and stirred for 30-45 minutes. A small aliquot (~300 mL) can be centrifuged to test whether lysis is complete. The pellet should be pale or white indicating the fluorescent protein has

been released from the cells. The lysis can be left overnight in the 4 °C fridge to remove protein trapped in inclusion bodies.

Once lysis is complete, TNS buffer (50 mM Tris-HCl, 0.1 mM EDTA, 50 mM NaCl, pH 8.0) is added at an equal volume of the cell mixture. The cold TNS aids in the precipitation of the lysate. The lysis mixture is chilled in ice water for 10 minutes and then is spun down in the centrifuge at 11,000 rpm for 15 minutes. The supernatant is carefully decanted into a clean conical tube and is re-spun for 11,000 rpm for 20 minutes. The supernatant is filter using a syringe with a 0.45 µm polyethersulfone membrane filter, being careful not to expel the filter.

After the supernatant is filtered, it is added to a column of Ni-NTA resin that has been pre-calibrated in TNS buffer, with 3-4 mL of resin used per protein pellet. The resin binds to His-tagged proteins which can then be eluted with a high concentration of Imidazole. The column is stirred or rocked over ice or in the 4 °C fridge for 20 minutes or until a spun down aliquot shows little to no color in the supernatant. To test if more resin is needed, it can be added to a small sample and tested to see if more color is removed from the supernatant. The column is placed vertically over a conical vial to gravity pack the column. The column is rinsed with approximately 10 column volumes of TNS buffer, followed by 10 column volumes of TNS + 10mM imidazole, followed by 10 column volumes of TNS + 20 mM imidazole. After these rinses the protein is eluted from the column with TNS + 250 mM Imidazole into a clean tube. Collection stops once the color has moved off the resin.

The protein is concentrated with an Amicon Ultra-4 Centrifugal Devices following the datasheet for these devices. The protein is concentrated in one of these Amicon spin columns for 30 kDa proteins for 15 minutes at 7500 rpm. The process can be repeated until the desired concentration is reached. Buffer exchange is done using a PD-10 column (GE Healthcare, 10 mL). The manufacturer instructions are used for gravity buffer exchange with dialysis buffer (150 µM NaCl, 0.05 M Tris, pH 7.4 buffer) as the exchange buffer. The protein is re-concentrated if needed and the concentration of the protein is measured using the Nanodrop instrument and is frozen rapidly using liquid Nitrogen to avoid denaturation. Protein is frozen in small aliquots to avoid repetitive freezing and thawing that may affect biological activity or damage the protein structure. Proteins are stored for at most one week at 4 °C before being discarded and efforts are made to not use sample past 24 hours after thawing.